NPS 68-89-007

# NAVAL POSTGRADUATE SCHOOL
## Monterey, California

# THESIS

A NUMERICAL STUDY OF WIND FORCING IN
THE EASTERN
BOUNDARY CURRENT SYSTEM OFF PORTUGAL

by

Carlos N. Lopes da Costa

September 1989

Thesis Advisor                                         M. L. Batteen

Approved for public release; distribution is unlimited.

Prepared for:
Office of Naval Research
800 N. Quincy Street
Arlington, VA    22217-5000
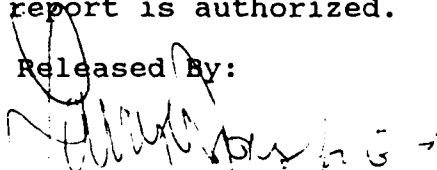
NAVAL POSTGRADUATE SCHOOL
Monterey, CA.   93943

Rear Admiral Ralph W. West, Jr.                    Harrison Shull
Superintendent                                     Provost


This report was prepared in conjunction with research conducted for Chief of Naval Research and Funded by the Naval Postgraduate School.

Reproduction of this report is authorized.

Released By:

GORDON E. SCHACHER
Dean of Science and Engineering

Unclassified

security classification of this page

## REPORT DOCUMENTATION PAGE

| 1a Report Security Classification Unclassified | 1b Restrictive Markings |
|---|---|

| 2a Security Classification Authority | 3 Distribution Availability of Report |
|---|---|
| 2b Declassification Downgrading Schedule | Approved for public release; distribution is unlimited. |

| 4 Performing Organization Report Number(s) NPS-68-89-007 | 5 Monitoring Organization Report Number(s) |
|---|---|

| 6a Name of Performing Organization Naval Postgraduate School | 6b Office Symbol (if applicable) 68 | 7a Name of Monitoring Organization Office of Naval Research |
|---|---|---|

| 6c Address (city, state, and ZIP code) Monterey, CA 93943-5000 | 7b Address (city, state, and ZIP code) 800 N. Quincy St., Arlington, VA 22217-5000 |
|---|---|

| 8a Name of Funding Sponsoring Organization | 8b Office Symbol (if applicable) | 9 Procurement Instrument Identification Number O&MN, Direct Funding |
|---|---|---|

| 8c Address (city, state, and ZIP code) | 10 Source of Funding Numbers | | | |
|---|---|---|---|---|
| | Program Element No | Project No | Task No | Work Unit Accession No |
| | | | | |

11 Title (Include security classification) A NUMERICAL STUDY OF WIND FORCING IN THE EASTERN BOUNDARY CURRENT SYSTEM OFF PORTUGAL

12 Personal Author(s) Carlos N. Lopes da Costa in conjunction with M.L. Batteen and C.S. Nelson

| 13a Type of Report Master's Thesis | 13b Time Covered From To | 14 Date of Report (year, month, day) September 1989 | 15 Page Count 127 |
|---|---|---|---|

16 Supplementary Notation The views expressed in this thesis are those of the author and do not reflect the official policy or position of the Department of Defense or the U.S. Government.

| 17 Cosati Codes | | | 18 Subject Terms (continue on reverse if necessary and identify by block number) |
|---|---|---|---|
| Field | Group | Subgroup | Coastal Oceanography, upwelling, fronts, jets and eddies. |
| | | | |
| | | | |

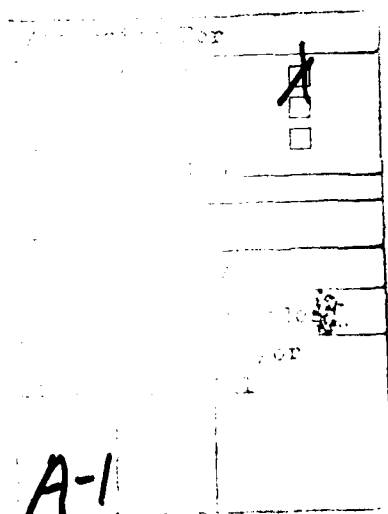19 Abstract (continue on reverse if necessary and identify by block number)

A high resolution, multi-level, primitive equation ocean model is used to examine the response to wind forcing of an idealized, flat-bottomed oceanic regime on a $\beta$-plane, along the eastern ocean boundary off the west coast of the Iberian Peninsula. Three experiments are conducted to investigate the role of different types of prescribed wind forcing. In experiment 1, a band of equatorward winds which are uniform alongshore but contain zonal variability (i.e., large negative wind stress curl near the coast), results in an equatorward coastal surface current nearshore and a poleward surface current offshore. With time, the currents become unstable and anticyclonic warm core eddies develop in the region of negative wind stress curl. In experiment 2, the model is forced with poleward wind stress for 20 days followed by a sudden change to equatorward wind stress. A 1-2 day transition from downwelling and a poleward surface current near the coast to upwelling and an equatorward surface jet occurs. With time the upwelled isotherms are displaced offshore, the equatorward surface jet widens and gets shallower nearshore, and the poleward undercurrent moves closer to the surface (depth $\sim$ 120 m at the coast). For experiment 3, a time series of 6-hourly values of the north south component of the wind, computed from Fleet Numerical Oceanography Center synoptic surface pressure analyses are used to investigate the response of the coastal current system to time dependent wind forcing. Equatorward wind events increase the vertical extent and cross-section of the surface equatorward jet and reduce the poleward undercurrent. Relaxations reduce the vertical extent of the equatorward surface coastal current, increase the cross-sectional area of the poleward undercurrent, and the undercurrent tends to shoal nearshore. Poleward winds displace the equatorward current offshore and create a poleward surface current nearshore. By the middle of the upwelling season, eddies are generated. By the end of the upwelling season (with the seasonal reversal to poleward winds), the eddies and equatorward surface current weaken or disappear and a poleward surface current develops nearshore. The results from the experiments support the hypothesis that wind forcing, and particularly time dependent winds, can be a significant generation mechanism for eddies, jets, fronts and upwelling filaments off the west coast of the Iberian Peninsula.

| 20 Distribution Availability of Abstract ☒ unclassified unlimited ☐ same as report ☐ DTIC users | 21 Abstract Security Classification Unclassified |
|---|---|

| 22a Name of Responsible Individual M. L. Batteen | 22b Telephone (include Area code) (408) 646-2768 | 22c Office Symbol 54Ss |
|---|---|---|

DD FORM 1473,84 MAR   83 APR edition may be used until exhausted   security classification of this page
All other editions are obsolete

Unclassified

i

A Numerical Study of Wind Forcing in the Eastern
Boundary Current System off Portugal

by

Carlos N. Lopes da Costa
Lieutenant Commander, Portuguese Navy
B.S., Portuguese Naval Academy, 1977

Submitted in partial fulfillment of the
requirements for the degree of

MASTER OF SCIENCE IN PHYSICAL OCEANOGRAPHY

from the

NAVAL POSTGRADUATE SCHOOL
September 1989

Author: _____

Carlos N. Lopes da Costa

Approved by: _____

M. L. Batteen, Thesis Advisor

_____

C. S. Nelson, Second Reader

_____

Curtis A. Collins, Chairman,
Department of Oceanography

ii

# ABSTRACT

A high resolution, multi-level, primitive equation ocean model is used to examine the response to wind forcing of an idealized, flat-bottomed oceanic regime on a $\beta$-plane, along the eastern ocean boundary off the west coast of the Iberian Peninsula. Three experiments are conducted to investigate the role of different types of prescribed wind forcing. In experiment 1, a band of equatorward winds which are uniform alongshore but contain zonal variability (i.e., large negative wind stress curl near the coast), results in an equatorward coastal surface current nearshore and a poleward surface current offshore. With time, the currents become unstable and anticyclonic warm core eddies develop in the region of negative wind stress curl. In experiment 2, the model is forced with poleward wind stress for 20 days followed by a sudden change to equatorward wind stress. A 1-2 day transition from downwelling and a poleward surface current near the coast to upwelling and an equatorward surface jet occurs. With time the upwelled isotherms are displaced offshore, the equatorward surface jet widens and gets shallower nearshore, and the poleward undercurrent moves closer to the surface (depth $\sim$ 120 m at the coast). For experiment 3, a time series of 6-hourly values of the north/south component of the wind, computed from Fleet Numerical Oceanography Center synoptic surface pressure analyses are used to investigate the response of the coastal current system to time dependent wind forcing. Equatorward wind events increase the vertical extent and cross-section of the surface equatorward jet and reduce the poleward undercurrent. Relaxations reduce the vertical extent of the equatorward surface coastal current, increase the cross-sectional area of the poleward undercurrent, and the undercurrent tends to shoal nearshore. Poleward winds displace the equatorward current offshore and create a poleward surface current nearshore. By the middle of the upwelling season, eddies are generated. By the end of the upwelling season (with the seasonal reversal to poleward winds), the eddies and equatorward surface current weaken or disappear and a poleward surface current develops nearshore. The results from the experiments support the hypothesis that wind forcing, and particularly time dependent winds, can be a significant generation mechanism for eddies, jets, fronts and upwelling filaments off the west coast of the Iberian Peninsula.

# TABLE OF CONTENTS

A-1

## LIST OF TABLES

# LIST OF FIGURES

## ACKNOWLEDGMENTS

# I. INTRODUCTION

## A. OBJECTIVES

Satellite images of the sea surface temperature distribution off Portugal and north-west Spain, taken during conditions favorable for upwelling, show several plumes/filaments extending offshore near 43° N, 41° 40′ N, 40° 20′ N, 38° 40′ N, and off southwest Portugal (Fiúza and Sousa, 1989). Ongoing studies, based on multi-year sequences of satellite imagery, indicate that such filaments tend to show up near the same places, mainly between the submarine canyons which indent the continental margin (Fiúza and Sousa, 1989). Observations have also shown that pairs of anticyclonic and cyclonic mesoscale eddies, with horizontal dimensions of order 100 km (Fiúza, 1984) can also exist off the west coast of Portugal and Spain. In other eastern boundary current regions of subtropical gyres, particularly in the California Current System, eddies have been shown to be generated by baroclinic instability (Emery and Mysak, 1980; Thomson, 1984; Ikeda and Emery, 1984; Batteen *et al.*, 1989), barotropic instability (Wright, 1980), or mixed barotropic/baroclinic instability (Thomson, 1984; Wright, 1980) of the large scale flow.

The primary objective of this thesis is to investigate the role(s) of climatological and time dependent wind forcing as possible generation mechanism(s) for the coastal jets, undercurrents, fronts, and eddies in the eastern boundary current region off the west coast of the Iberian Peninsula (IP). Experiments, designed to reproduce some of the possible important and/or unique features of the study area, will be systematically run using a multi-level, eddy-resolving primitive equation (PE) ocean model developed by Haney (1985) and modified by Batteen *et al.* (1989). The water temperature field will be initialized in all experiments based on climatological data for the area. Different wind forcing will be used to study some of the important processes due to wind driven circulation for the area. The role of wind forcing in the generation of mesoscale features in the current system off the IP has not been systematically investigated and may be the most important mechanism. Satellite infrared imagery has shown evidence of cold water filaments, jets, and eddies during periods of winds favorable for upwelling. These observations provide evidence for wind forcing as a possible important mechanism for the formation of the mesoscale features. Eddies and jets could respond to the seasonal mean wind or to wind fluctuations with time scales of a few days during the upwelling season.

The organization of the thesis is as follows. In Chapter I, the wind fields, hydrology, and circulation that are thought to be important or unique features for the study area are described. The PE ocean model and the experimental conditions used in the study are then presented (Chapter II). Chapter III describes the basis and procedures used to apply spectral analysis for the evaluation of wave lengths and kinetic energy of eddy fields that result from the simulations. In Chapter IV the results of the model simulations along with an analysis of the results are presented. A comparison of model results with available observations is also made. Conclusions and recommendations for future work are presented in Chapter V.

## B. BACKGROUND

In the following section, general descriptions of the wind fields, water masses, and circulation for the study region are presented. An introduction to the wind forcing used in some of the experiments is also given.

### 1. The Wind Fields

The seasonal regime of the Azores high pressure system and the meridional migration of the subtropical front, which separates the mid-latitude from the tropical air masses, regulates the mean wind conditions off the IP west coast (Fiúza, 1982). The center of the Azores high migrates along 38° W, from 27° to 33° N between March and August. The mean east-west pressure contrast between the coast of Portugal and the high center is higher in summer (8 mb) than in winter (1 mb), resulting in weak mean westerly winds in winter, and considerably stronger northerly and northwesterly mean winds in summer (Fiúza, 1982). The northern limit of southward upwelling favorable winds shifts from about 27° N, near the Canary islands, in January to about 43° N, over the northern limit of the Portuguese west coast, in July (Wooster et al., 1976). Based on one-degree latitude/longitude climatological summaries of wind stress estimates from ship reports near the coast of the IP, Bakun (1987) concluded that the mean wind stress curl distribution is weak and irregular during fall and early winter, but strongly cyclonic during the spring and summer, when the spatially separated wind stress curl maximum appears adjacent to the northwestern coast of the Iberian Peninsula and off southern Portugal (Figure 1). The region of cyclonic wind stress curl extends from the coast up to about 200 km offshore; farther offshore there is anticyclonic wind stress curl (Bakun, 1987).

Local wind patterns near the coast, associated with orographic features such as capes and. or rias (fjord type of estuary along the northwest coast of Spain). may signif-

2
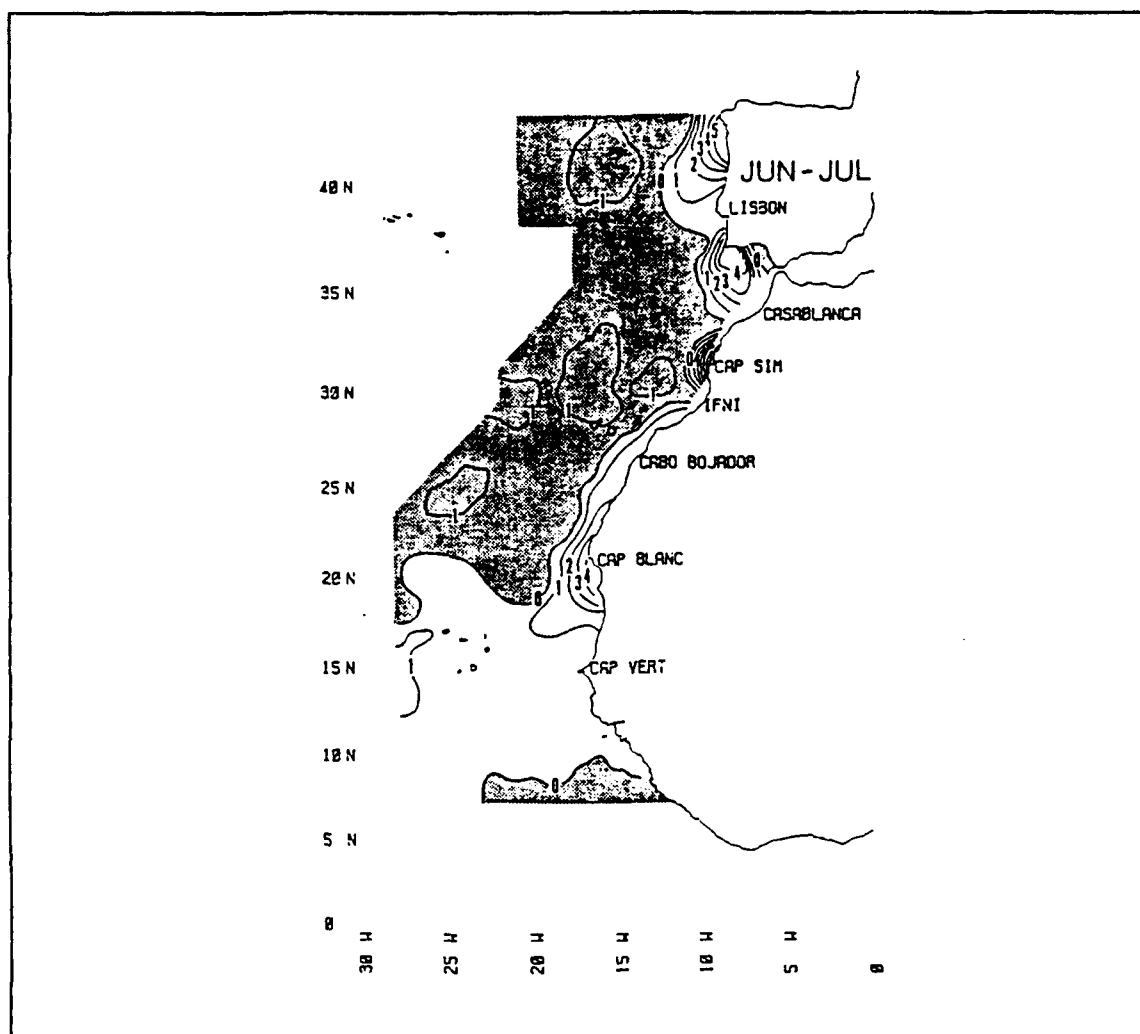
**Figure 1.** Wind stress curl distribution for June-July in the area off the west coast of the IP and NW Africa: Units are dynes/cm² per 1000 km. Regions of anticyclonic wind stress curl are shaded and regions of cyclonic wind stress curl are unshaded (from Bakun, 1987).

icantly influence the flow near the coast. For instance, McClain *et al.* (1986) combined information on the wind stress derived from surface pressure charts and ship observations for the period from 18 to 22 April 1982 and found consistently strong winds with a heading to the southwest at the mouth of Ria de Arosa, parallel to the axis of the ria, and generally weaker winds a small distance offshore (about 20 km). The existence of the resulting large negative wind stress curl, possibly orographically induced, has been

3

concluded by McClain *et al.* (1986) to be the primary driving mechanism for the current shear associated with an observed southward coastal jet adjacent to a northward off-shore current near the shelf break. These wind and current features will be explored in experiment 1.

A time series of monthly values (over a 32-year period, 1948-1979) of the wind stress in four, five-degree latitude/longitude quadrangles off the IP was analyzed by Bakun (1987). The quadrangles used in the analysis are shown in Figure 2. The area covered by these data overlays the numerical model domain used in the present study (see Chapter II). Based on his analysis of climatological and time-dependent winds, the following features of the wind field were noted by Bakun (1987):

- The seasonal cycle (long term mean monthly values) of the alongshore wind stress in the near-coastal areas, shows strongest equatorward values during the upwelling season, roughly from April through September.

- There is a general trend towards increased values of the alongshore (southward) wind stress (averaging values for April through September of each year) from the beginning of the time series (1948) to the end (1979).

- The long term mean monthly values of alongshore wind stress are stronger in the southern areas compared to the northern areas. This feature is apparent if every month is included in the averaging process, and particularly so, if the upwelling season alone is considered.

A time series of 6-hourly values of the north/south component of the wind velocity computed from Fleet Numerical Oceanography Center (FNOC) surface pressure analyses, for the period from 1 February to 31 December 1986, at 39°N, 10°W is shown in Figure 3. The wind velocity computation is based on a finite difference calculation of the geostrophic wind (from the analyzed surface pressure field interpolated onto a 3-degree latitude/longitude grid), with a subsequent multiplication by 0.7 and a rotation of 15° to the left to account for friction. These wind values may be seen as an approximation to the large spatial scale, time dependent winds in the IP. Fluctuations of the alongshore component of the wind stress with time scales of a few days (which may be associated with reversals of the coastal currents) can be seen. In addition, sequences of alternating upwelling favorable events (southward winds) and relaxations (northward winds) are common features of the time series. Spectral densities computed from this data series (Figure 4) show a considerable amount of variance in the event time scale (e.g., 4-20 days). The strong peak at the diurnal frequency is probably associated with differential day/night heating over land and over the ocean and corresponding changes
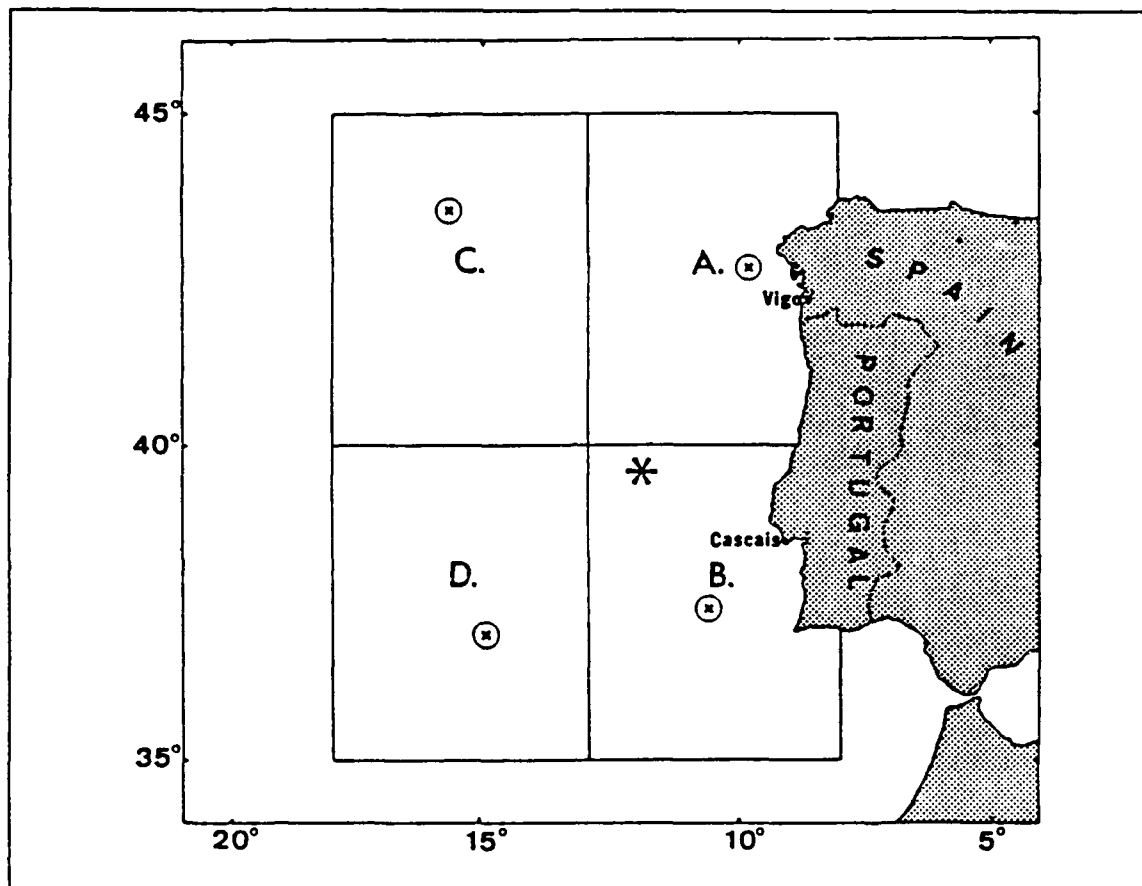
**Figure 2.** Locations of 5-degree latitude/longitude quadrangles off the west coast of the IP: (areas labeled 'A', 'B', 'C', and 'D') used to summarize maritime reports in monthly time series. The mean position of reports within each of these areas, over the period 1948 to 1979, is marked by the 'X' symbols surrounded by small circles. The mean latitude and longitude of the reports from all four areas together (i.e., from the entire 10-degree quadrangle) is marked by the large asterisk (from Bakun, 1987).

in the cross-shore pressure gradient. The response of currents to this time series will be explored in experiment 3 (see Chapter IV).

## 2. The Water Masses

Climatological temperature, salinity, and potential density data, from Levitus (1982), for 5-degree latitude/longitude quadrangles centered at 37.5° N, 12.5° W (southern area) and 42.5° N, 12.5° W (northern area) have been plotted (Figures 5, 6,
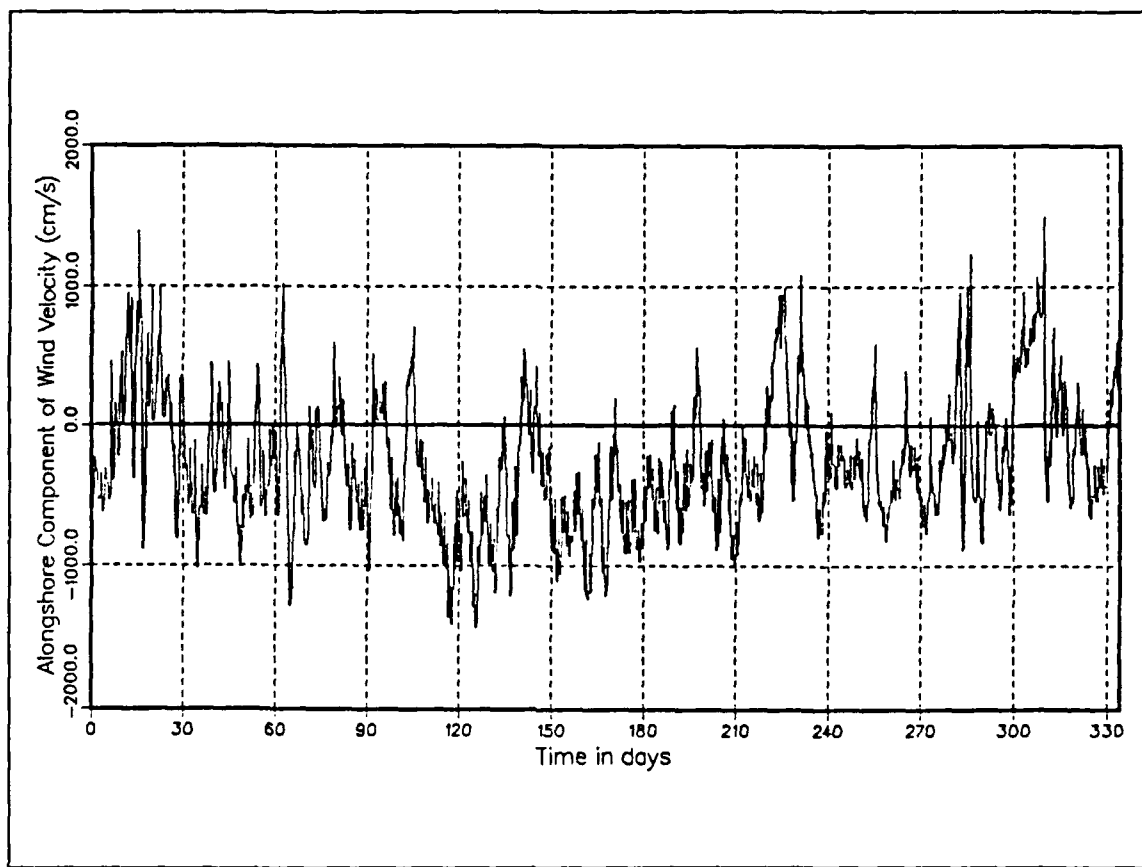
**Figure 3.** Time series of the six hourly values for the north/south component of the wind velocity (cm/s) from 1 February to 31 December 1986 at position 39°N, 10°W: Day zero is 1 February 1986.

and 7) and used to examine large scale features of the water properties in the study area. The upper water, from the surface down to about 125 m, includes the mixed layer and the seasonal thermocline (Figure 8). The layer between approximately 125 and 500 m, plotted in a temperature-salinity diagram (Figure 9), shows a linear relationship between temperature and salinity with a slope of about 6.9°C per part per thousand (ppt). This is North Atlantic Central Water (Sverdrup *et al.*, 1942). The intermediate depths, from about 500 m and 2000 m, roughly the depth of the 35.1 ppt isohaline, are strongly influenced by Mediterranean Water. The stronger influence of Mediterranean Water is located at 1000-1200 m and corresponds to a relative maximum of salinity (Figure 6), relatively high temperature (10.0-10.5°C, Figure 5), and potential density ($\sigma_\theta$) of about 1027.75 $kg/m^3$ (Figure 7), as seen from climatology. Ambar and Howe (1979), have

6
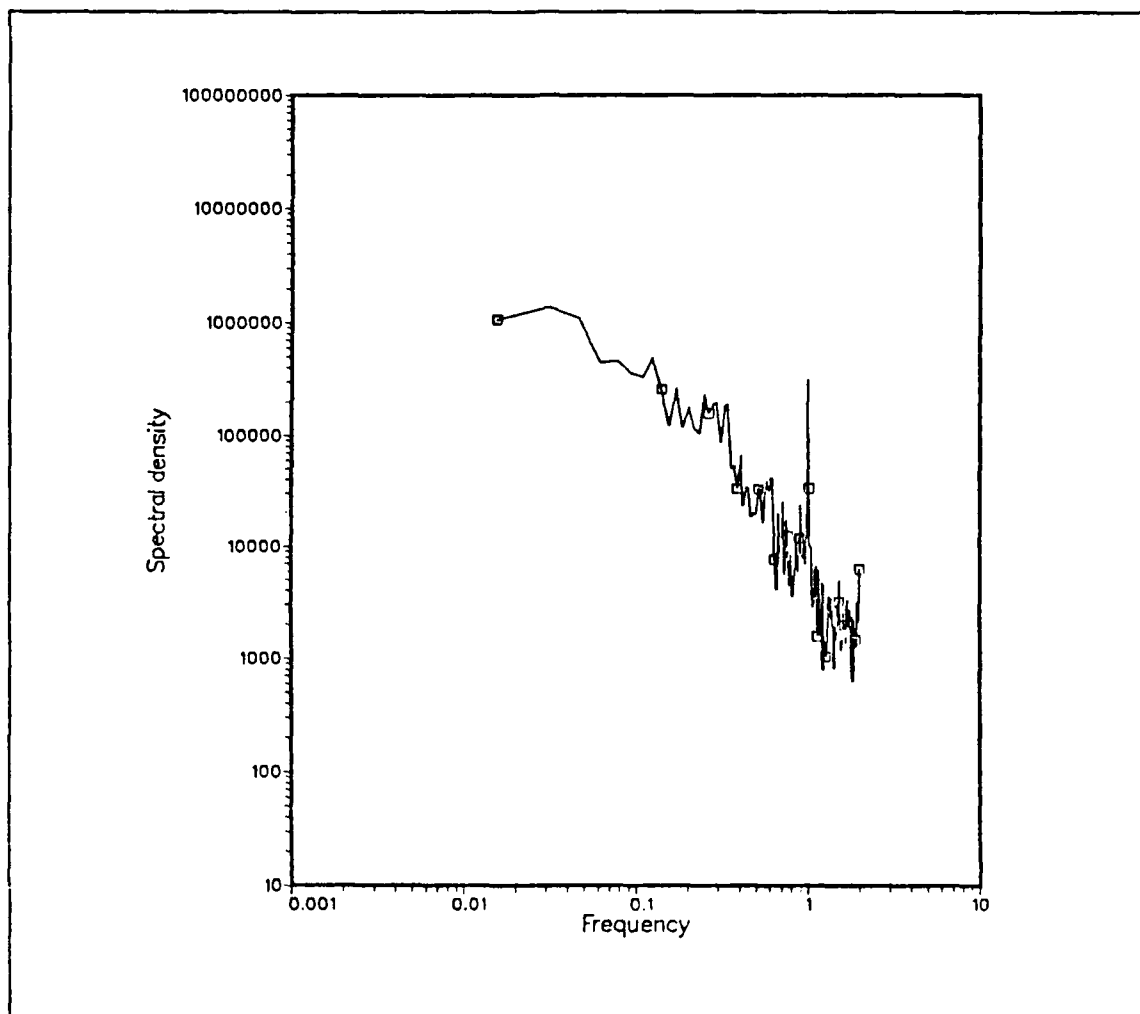
**Figure 4.** Spectral densities of the north/south component of the wind velocity at 39°N, 10°W from 1 February to 18 December 1986: Units are $cm^2 s^{-2} day$ for spectral density and $day^{-1}$ for frequency.

documented the separation of the Mediterranean outflow into two distinct cores, at about 7° W. Both cores flow westward at different depths, along the continental slope in the Gulf of Cadiz and turn northward around Cape São Vicente. At 38° N, off western Portugal, the upper core was observed with a relative temperature maximum of 12.67°C at 660 m, and the lower core, recognized by a salinity maximum, was located further to the west at depths nearer 1300 m (Ambar and Howe , 1979). A third shallower vein of Mediterranean Water (distinct from the two main cores) was traced from the vicinity of the Strait of Gibraltar northward to about 38° 30' N, off western Portugal,

7

and followed the upper continental slope off the IP (Ambar, 1983). Below the Mediterranean Water, from 2000 m downward, North Atlantic Deep Water of relatively low stratification is present (Figure 7). Bottom waters with a temperature of about 2.5°C and salinity of 34.9 ppt (Figures 5 and 6) are evolved forms of Antarctic Bottom Water (Tchernia, 1980).

Comparing the climatological vertical profiles of *in situ* temperature, salinity, and potential density for the northern and southern areas, the following large scale features may be noted :

- From the surface to about 2500 m, there is a substantial meridional gradient in the large scale temperature field (colder in the north, warmer in the south). From 2500 m downward nearly uniform water temperatures correspond to North Atlantic Deep Water and Bottom Water.

- In the upper 2500 m we note a substantial decrease of salinity from south to north, that is, a decrease of salinity with distance from the area of Mediterranean Water outflow (Figure 6). The meridional gradients of salinity and *in situ* temperature have the same vertical extent in the water column. Below 2500 m the salinity field looks uniform in the meridional sense.

- The potential density field shows, in the upper 600 m, increasing values of $\sigma_\theta$ from south to north, suggesting that the temperature effect overcomes the salinity effect. Bellow 600 m. one notes decreasing values of $\sigma_\theta$ from south to north, especially at the levels of Mediterranean influence (1000-2000 m), indicating that salinity has an important control on density at these levels (Figure 7).

### 3. The General Circulation

Wooster *et al.* (1976), based on an analysis of mean monthly ship drift data, concluded that near the eastern boundary off Portugal there is maximum equatorward surface flow during the upwelling season. A seasonal reversal to predominantly northward winds during winter is accompanied by poleward alongshore surface flow. Current meter observations near the continental slope in 2450 m of water, 100 km west of Cape São Vicente, indicate northward flow at levels between 234 and 2046 m (Meincke *et al.*, 1975). In winter the countercurrent may reach the surface, but in other seasons, the poleward flow can have the configuration of a northward undercurrent below the upper 100 to 200 m, where the wind driven Portugal current flows southward (Fiúza, 1982). Moored current meter observations in 1100 m of water at 37° 24' N, 9° 25'W indicate a mean flow of 0.1 m s towards the north over the period December 1982 to May 1983 at 750 m; the meridional (v) component decrease with depth to almost 0 at 200 m (Ambar, 1984; cited in Barton, 1989). Current meter data, in 1100 m of water, at 40° N, 9° 45'W. from July 1983 through January 1984, show a mean northward flow in excess of 0.3 m s between 200 and 750 m (Ambar, 1985; cited in Barton, 1989). The
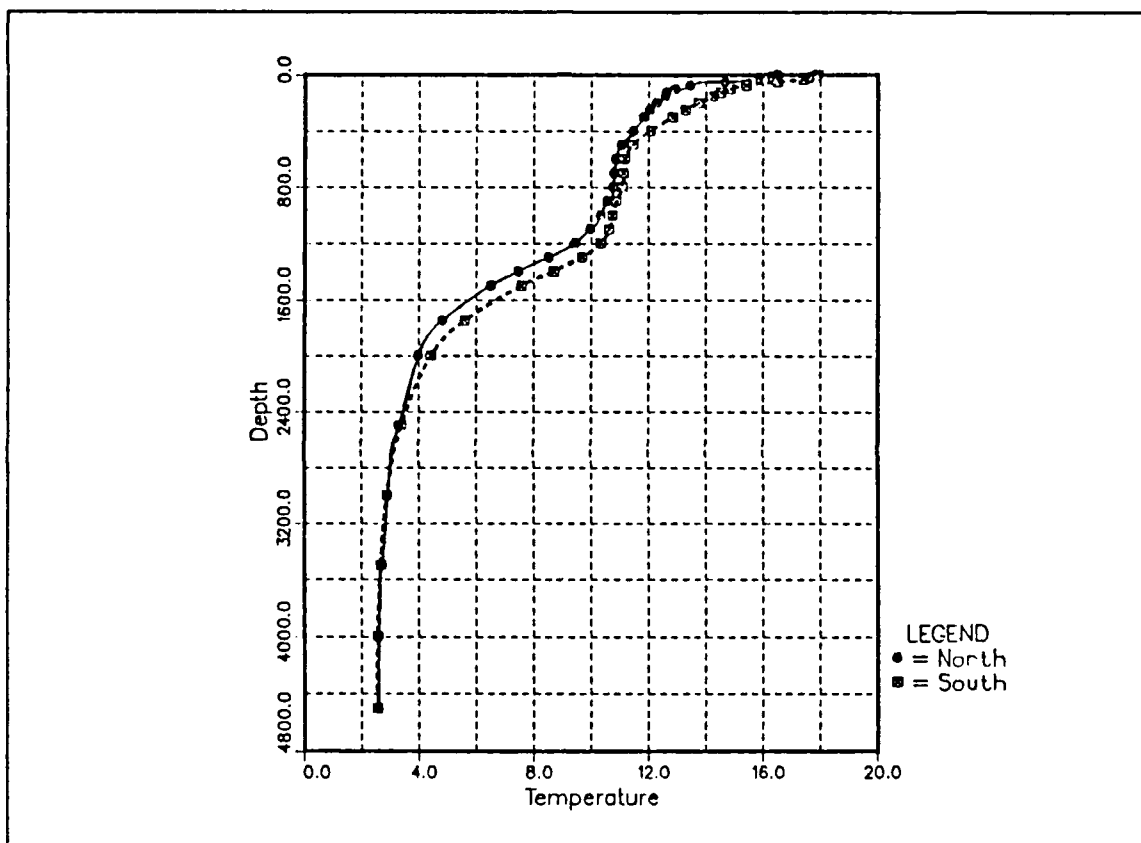
**Figure 5.** Climatological temperature profiles: for 5-degree latitude/longitude quadrangles centered at 42.5° N, 12.5° W and 37.5° N, 12.5° W. Temperature and depth have units of °C and meters, respectively. Data from Levitus (1982).

undercurrent off Portugal, deeper than 100-200 m, can flow northward and transport water from the Mediterranean between 500 and 1500 m depth, and water from a subtropical origin in the upper layers (Fiúza, 1982).

9
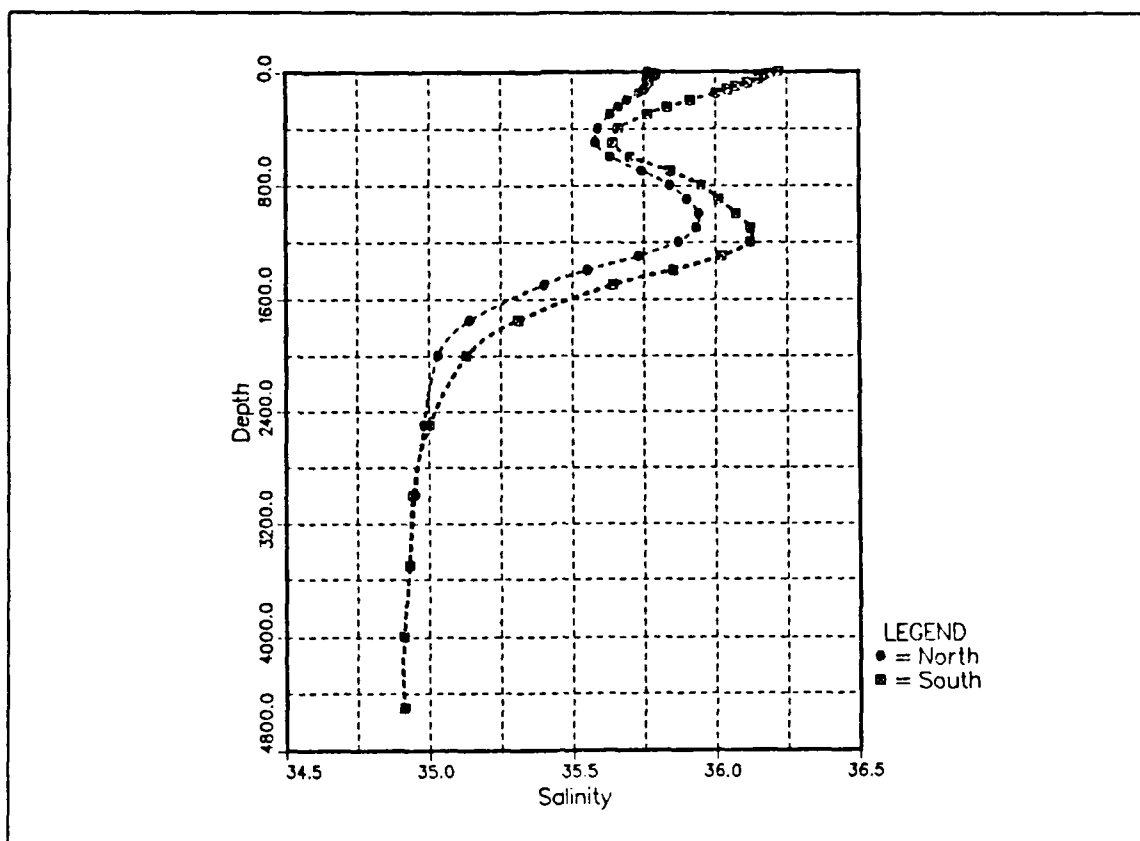
**Figure 6.** Climatological salinity profiles: for the 5-degree latitude longitude quadrangles centered at 42.5° N, 12.5° W and 37.5° N, 12.5° W. Salinity and depth have units of ppt and meters, respectively. Data from Levitus (1982).
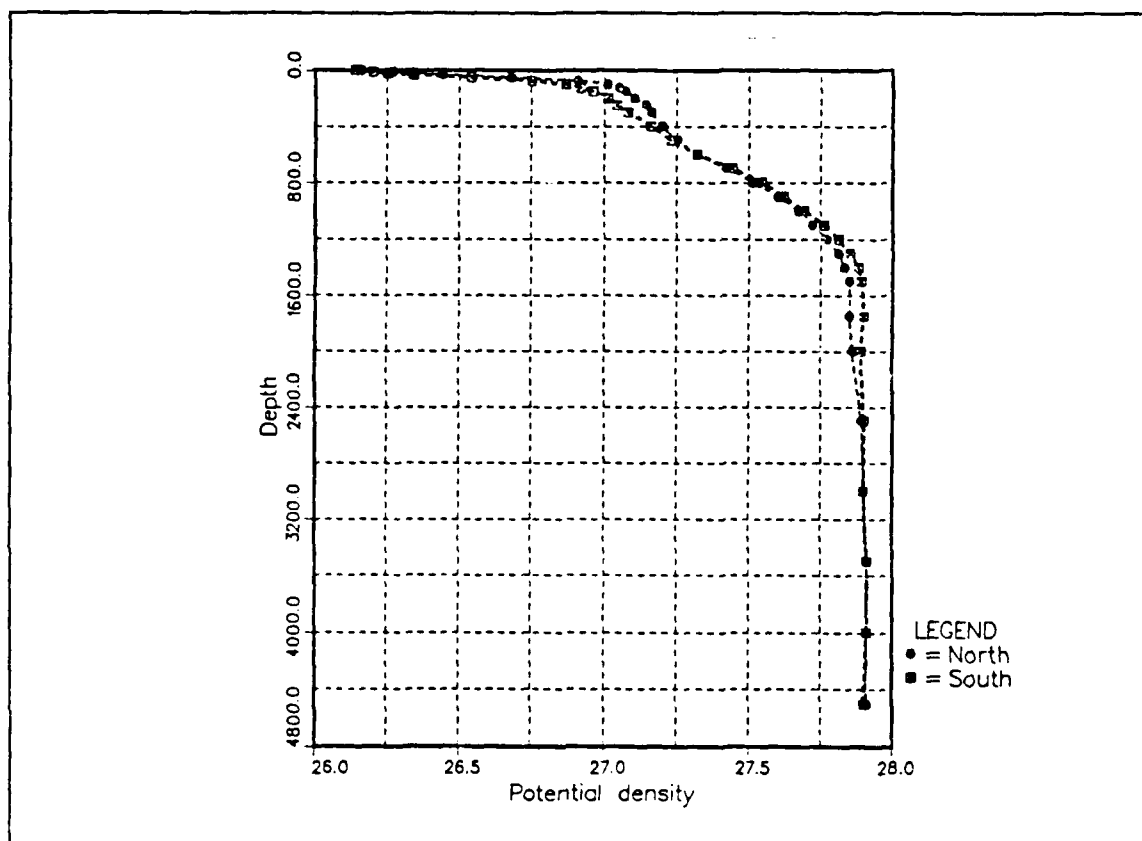
**Figure 7.** Climatological potential density profiles: for the 5-degree latitude longitude quadrangles centered at 42.5° N, 12.5° W and 37.5° N, 12.5° W. Potential density has units of $kg\ m^{-3}$ and values are subtracted from 1000; depth is in meters. Data from Levitus (1982).
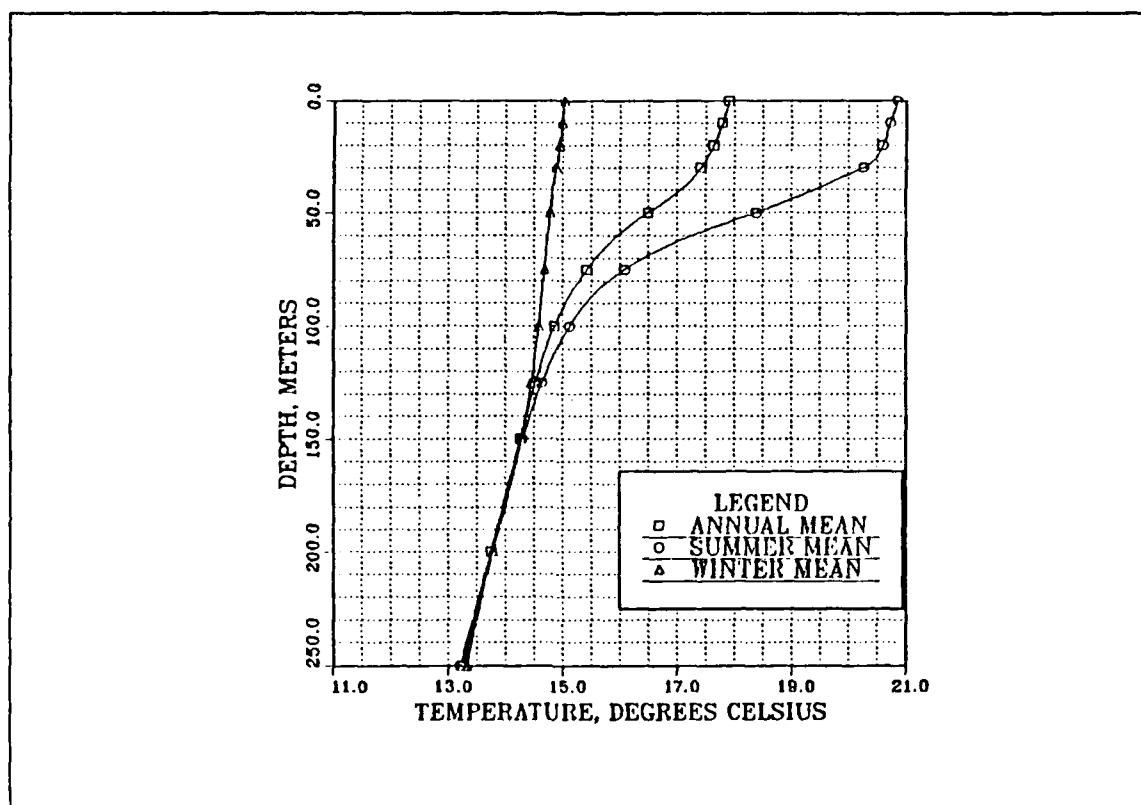
Figure 8.    Climatological summer, winter, and annual temperature (°C) profiles in the upper 250 m of the water column:    for the 5-degree latitude/ longitude quadrangle centered at 37.5° N, 12.5° W. Data from Levitus (1982).

12
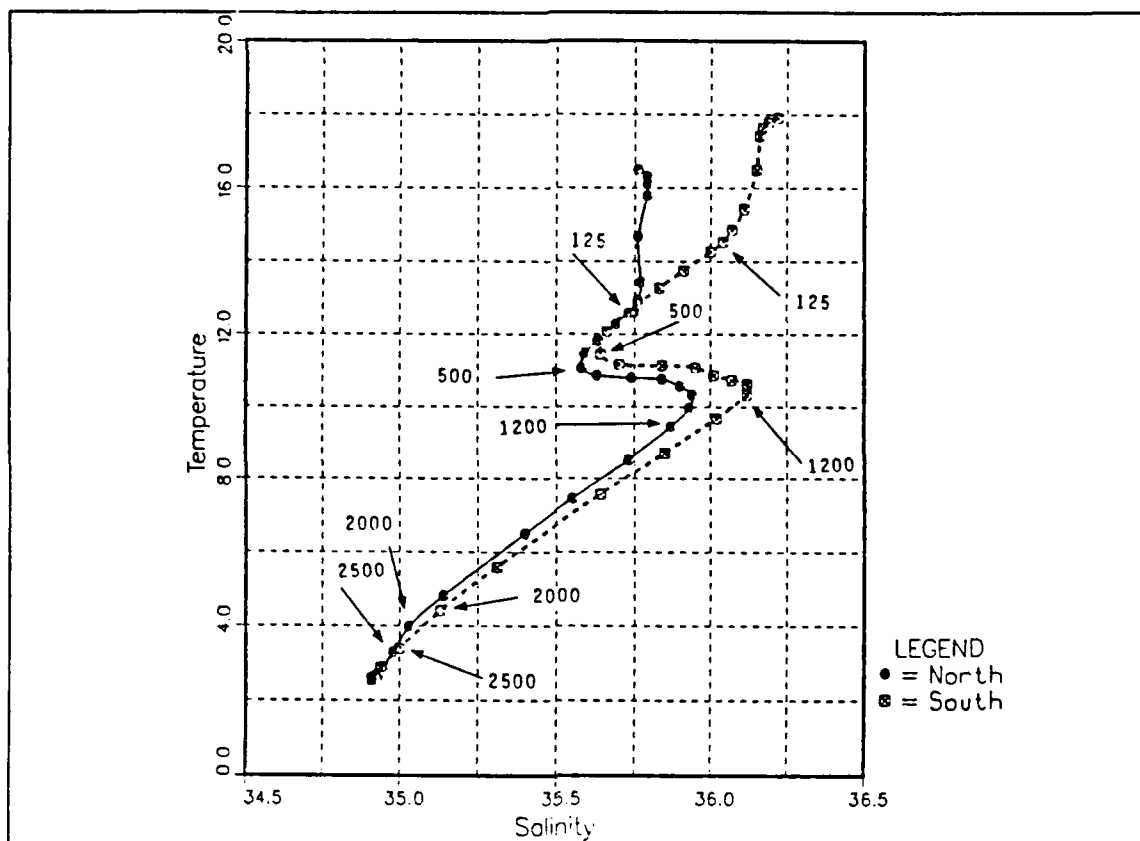
**Figure 9.** Climatological temperature-salinity diagrams: for the 5-degree latitude longitude quadrangles centered at 42.5° N, 12.5° W and 37.5° N, 12.5° W. Temperature and salinity have units of °C and ppt, respectively. Numbers associated with the arrows indicate depths in meters. Data from Levitus (1982).

# II. NUMERICAL MODEL

## A. MODEL DESCRIPTION

### 1. Model Equations

The numerical model used in the experiments was developed by Haney (1985), modified by Batteen et al. (1989), and is a multi-level, primitive equation (PE) model. The hydrostatic, rigid lid, $\beta$-plane, and Boussinesq approximations are used in the model. The governing equations are as follows :

$$\frac{du}{dt} = \frac{-1}{\rho_0} \frac{\partial p'}{\partial x} + fv - A_m \nabla^4 u + K_m \frac{\partial^2 u}{\partial z^2} + \delta_d(u) \qquad [1]$$

$$\frac{dv}{dt} = \frac{-1}{\rho_0} \frac{\partial p'}{\partial y} - fu - A_m \nabla^4 v + K_m \frac{\partial^2 v}{\partial z^2} + \delta_d(v) \qquad [2]$$

$$w = - \int_{-H}^{z} ( \frac{\partial u}{\partial x} + \frac{\partial v}{\partial y} ) d\varepsilon \qquad [3]$$

$$p' = \int_{z}^{0} \rho g d\varepsilon - \frac{1}{H} \int_{-H}^{0} ( \int_{z}^{0} \rho g d\varepsilon ) dz \qquad [4]$$

$$\rho = \rho_0 (1 - \alpha(T - T_0)) \qquad [5]$$

$$\frac{dT}{dt} = - A_H \nabla^4 T + K_H \frac{\partial^2 T}{\partial z^2} + Q_s + \delta_d(T) \quad . \qquad [6]$$

In the above equations, t is time and (x,y,z) is a right-handed cartesian coordinate system with x pointing toward shore, y alongshore, and z upward. The corresponding velocity components are (u,v,w), T is temperature, $\rho$ is density, and $p'$ is the departure of the pressure from the vertically averaged pressure. In equations (3) and (4), $\varepsilon$ is a dummy variable of integration. Equation (4) includes the assumption that the depth-averaged pressure is a constant (assumed zero); that is, the barotropic mode is ignored. Equation (5) assumes that density is a function of temperature only. This as-

14

sumption may not be appropriate for the study region, because salinity also affects density over a substantial vertical extent due to the influence of the Mediterranean outflow. The relatively important river runoff north of 41° N may also control the density near the coast. Future modeling studies of the region should incorporate salinity to assess its effect on the circulation off the IP. In (6), $Q_s = \frac{1}{\rho_0 C} \frac{\partial S}{\partial z}$ is the heating (a function of depth) due to solar radiation, where

$$S = S_0(R \, e^{z/z_1} + (1 - R) \, e^{z/z_2}) \quad . \qquad [7]$$

In formula (7), $S_0$ is the downward flux of solar radiation at the surface, $R = 0.62$ is the fraction of solar radiation absorbed in the upper few meters ($z_1 = 1.5$ m), and $(1 - R) = 0.38$ is the fraction that penetrates to somewhat deeper levels ($z_2 = 20$ m), as given by Paulson and Simpson (1977). The terms $\delta_d(u)$, $\delta_d(v)$ and $\delta_d(T)$ represent the vertical turbulent mixing of zonal and meridional momentum and heat, respectively, due to surface layer processes, by a dynamic adjustment mechanism. This adjustment maintains the dynamic stability in the water column, in the sense of lighter water overlaying denser water.

The boundary conditions at the top ($z = 0$) of the model ocean are :

$$K_m \frac{\partial u}{\partial z} = 0 \qquad [8]$$

$$K_m \frac{\partial v}{\partial z} = \frac{\tau}{\rho_0} \qquad [9]$$

$$K_H \frac{\partial T}{\partial z} = - Q_B \qquad [10]$$

$$w = 0 \quad . \qquad [11]$$

In (9), $\tau$ is the alongshore component of the surface wind stress. In (10), $Q_B$ is the net upward flux of long wave radiation, sensible, and latent heat across the sea surface.

The bottom ($z = -H$) boundary conditions are as follow :

$$K_m \frac{\partial u}{\partial z} = C_D(u^2 + v^2)^{1/2}(u \cos \gamma - v \sin \gamma) \qquad [12]$$

$$K_m \frac{\partial v}{\partial z} = C_D(u^2 + v^2)^{1/2}(v \cos \gamma + u \sin \gamma) \qquad [13]$$

15

$$K_H \frac{\partial T}{\partial z} = 0 \qquad\qquad [14]$$

$$w = 0 \quad . \qquad\qquad [15]$$

In the above equations, $C_D$ is a bottom drag coefficient and $\gamma = 10°$ is the geostrophic inflow angle (Weatherly, 1972). Table 1 provides other symbols in the model equations, as well as values of constants used throughout this study.

Table 1.  VALUES OF CONSTANTS USED IN THE MODEL

|  | Value | Name |
|---|---|---|
| $\Omega$ | $2\,\pi\ day^{-1}$ | earth rotation rate |
| C | $0.958\ cal\,gm^{-1}\,(°K)^{-1}$ | specific heat of sea water |
| $C_D$ | $1.3 \times 10^{-3}$ | drag coefficient |
| L | $595.\ cal\,gm^{-1}$ | latent heat of sea water |
| $T_0$ | $278.2°K$ | constant reference temperature |
| $\rho_a$ | $1.23 \times 10^{-3}\ gm\,cm^{-3}$ | density of air |
| $\rho_0$ | $1.0276\ gm\,cm^{-3}$ | density of sea water at $T_0$ |
| $\alpha$ | $2.01 \times 10^{-4}\ (°K)^{-1}$ | thermal expansion coefficient |
| K | 10 | number of levels in vertical |
| $\Delta X$ | $8. \times 10^5\ cm$ | zonal grid spacing |
| $\Delta Y$ | $1.6 \times 10^6\ cm$ | meridional grid spacing |
| D | $4.5 \times 10^5\ cm$ | total ocean depth |
| $\phi_0$ | $34.7°\ N$ | latitude of southern boundary |
| $\phi_m$ | $44.3°\ N$ | latitude of northern boundary |
| $\lambda_0$ | $9.0°\ W$ | longitude of eastern boundary |
| $\lambda_m$ | $15.0°\ W$ | longitude of western boundary |
| $\Delta t$ | $800.\ s$ | time step |
| f | $0.93 \times 10^{-4}s^{-1}$ | Coriolis parameter |
| g | $980.\ cm\,s^{-2}$ | acceleration of gravity |
| $A_M$ | $2. \times 10^{17}\ cm^4\,s^{-1}$ | biharmonic momentum diffusion coefficient |
| $A_H$ | $2. \times 10^{17}\ cm^4\,s^{-1}$ | biharmonic heat diffusion coefficient |
| $K_M$ | $0.5\ cm^2\,s^{-1}$ | vertical eddy viscosity |
| $K_H$ | $0.5\ cm^2\,s^{-1}$ | vertical eddy conductivity |

## 2. Model Domain and Resolution

The domain of the model is the rectangular region extending from approximately 9° to 15° W and from 34.7° to 44.3° N (Figure 10), covering an area of 6 degrees of longitude by 9.6 degrees of latitude. The region extends approximately 500 km offshore from the west coast of the IP, and it spans 1024 km in the alongshore direction, exceeding by about 1.3 degrees of latitude the northern limit of the coast (Cape Finisterre at 43° N), and by 2.3 degrees of latitude the southern limit (Cape São Vicente at 37° N). The horizontal grid spacing in the model is 8 km in the cross-shore direction and 16 km in the alongshore direction, which should allow realistic, spatial resolution of mesoscale features in the Portugal Current System, since these features are expected to have typical wave lengths on the order of 100 km. Although there are variations in the coastline and ocean bathymetry (e.g., Cape Roca, and a few submarine canyons), these variations are omitted in the model to focus on the role of wind forcing in the generation of eddies.

## 3. Finite Difference Scheme

In the horizontal, a space-staggered B-scheme (Arakawa and Lamb, 1977; Batteen and Han, 1981) is used. There are 10 layers in the vertical, separated by constant z-levels placed at depths of 13, 46, 98, 182, 316, 529, 870, 1416, 2283, and 3656 m.

## 4. Boundary Conditions

The eastern boundary, representing the west coast of the IP, is modeled as a straight, vertical wall. A no-slip condition on the tangential velocity is invoked at the coastline. The northern, southern, and western boundaries are open using a modified version of the radiation boundary condition of Camerlengo and O' Brien (1980).

The 1024 km alongshore extent of the modeled coastline is not realistic, since the distance between Cape São Vicente and Cape Finisterre is approximately 667 km. However, the choice of this meridional extent allows wind forcing only along the corresponding section of the real coast. That is, the model uses both northern and southern bands of no wind forcing which, according to McCreary *et al.* (1987) and Batteen *et al.* (1989), will avoid unrealistic results for wind forced cases. The use of a band of wind forcing in the interior of the domain although somewhat artificial, allows for the propagation of coastal Kelvin waves, which can establish the alongshore pressure gradient field, resulting in a surface-trapped coastal jet and an approximately realistic undercurrent (Batteen *et al.*, 1989).

17
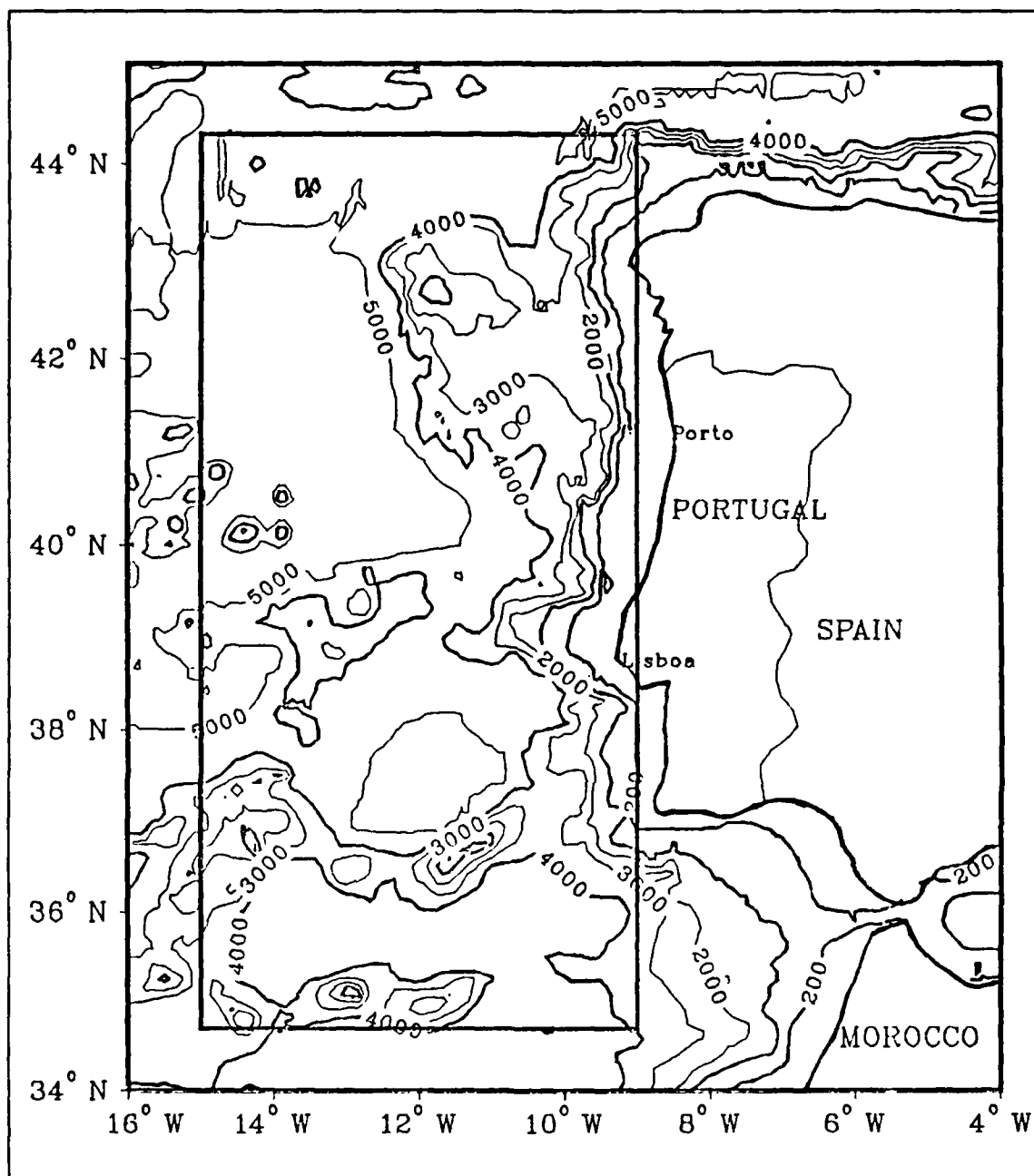
**Figure 10.  Model domain area and ocean bathymetry:  Depths in meters.**

## 5.  Heat and Momentum Diffusion

The model uses biharmonic lateral momentum and heat diffusion with the choice of coefficients listed in Table 1 .  The choice of biharmonic, rather than

Laplacian lateral diffusion, along with the appropriate coefficients, is justified since biharmonic diffusion is scale selective and acts predominantly on scales smaller than those of eddies (Holland, 1978), allowing mesoscale eddies to be generated via baroclinic and or barotropic instability processes (Holland and Batteen, 1986).

## B. INITIALIZATIONS AND SPECIFIC EXPERIMENTAL CONDITIONS

The model can either be spun up from rest by a surface wind stress or heat flux, or it can be initialized with a specified current field. In this study the model is spun up from rest by a prescribed surface wind stress.

### 1. The Initial Temperature Field

Based on the mean climatological temperature profile (Figure 5) for the 5° latitude/longitude square centered at 37.5° N, 12.5° W, a simple approximation was used to initialize the temperature field in the model. This approximation consists of using exponentials for the upper 500 m and the lower 3300 m of the water column, with a linear variation between. The function fits the climatological profile and is given by :

$$T(z) = 9.8 + 7.7 \, e^{(z/300)}, \qquad ( -500 \, m \le z \le 0 \, m)$$

$$T(z) = 11.25 + 7.857 \times 10^{-4}(z + 500), \qquad ( -1200 \, m \le z < -500 \, m) \qquad [16]$$

$$T(z) = 2.5 + 8.2 \, e^{( \frac{(z+1200)}{600} )}, \qquad ( -4500 \, m \le -1200 \, m).$$

The resulting temperature profile (Figure 11) was introduced into the model to provide initial values at each of the 10 levels. The same initial temperature profile was used in each of the numerical experiments. The model computes density from temperature using equation (5).

### 2. The Thermal Forcing

The eastern boundary region off the west coast of the IP has, in the mean, a net heat gain from March through September (Bakun, 1987). This net gain occurs because of reduced latent heat flux and downward sensible heat flux in the coastal region, due to the presence of cold, upwelled water during summer. A surface thermal forcing is applied to simulate the real heat fluxes across the surface and avoid unrealistic low surface temperatures due to continuous upwelling forced by a constant equatorward, alongshore winds.

The incoming solar radiation at the top of the atmosphere $Q_0$ , was specified to be 983.3 $cal \, cm^{-2} \, day^{-1}$, as representative for June and July at latitude 39.5° N. The sum of the net long wave radiation, latent and sensible heat fluxes, $Q_B$ , was computed during

19
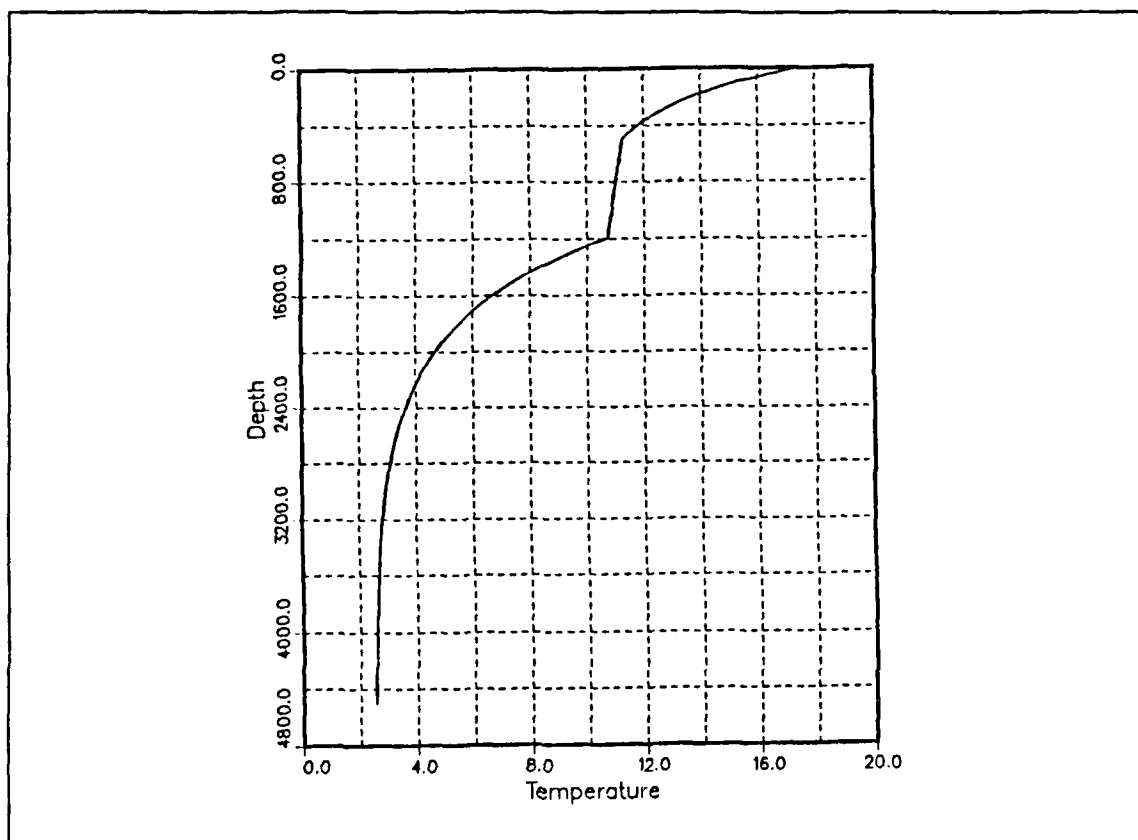
**Figure 11.** Initial temperature profile used in all experiments: Units for depth and temperature are meters and °C, respectively.

the model experiments from standard bulk formulas (Haney *et al.*, 1978), using April through September mean values of cloud cover, relative humidity, surface atmospheric pressure, the model simulated sea surface temperature field, the specified wind, and the air temperature. In the steady wind experiments, the air temperature was chosen initially to produce a zero net heat flux across the surface. Climatological (April through September) values for cloud cover, relative humidity and surface atmospheric pressure of 0.48, 86%, and 1018.3 mb, respectively, were taken from the climatological atlas by Esbenson and Kushnir (1981). Specified values for the wind speed and air temperature used for thermal budget computations in each of the experiments are indicated in Table 2.

**Table 2.** SPECIFIED VALUES OF WIND SPEED AND AIR TEMPERATURE FOR THE HEAT BUDGET OF THE EXPERIMENTS

|  | Exp. 1 | Exp. 2 | Exp. 3 |
|---|---|---|---|
| Spatial mean wind speed (cm/s) | 859 | 900 before day 20, 1425 after day 20 | 485 |
| Air temperature (°K) | 289 | 289 before day 20, 290 after day 20 | 287 |

## 3. Wind Forcing Experiments

### a. Experiment 1 (Large Negative Wind Stress Curl near the Coast)

The wind field used in this experiment (Figure 12) consists of :

- A strong northerly wind of 1426 cm/s (wind stress of about 3.5 $dyne/cm^2$) within 48 km of the coast.

- A sudden decrease of the alongshore wind stress to 754 cm/s (about 0.8 $dyne/cm^2$) between 48 and 64 km off the coast.

- Cyclonic wind stress curl, followed by anti-cyclonic curl, that approaches the climatological summer situation for the offshore part of the study region.

In this experiment we add to the large scale climatological wind field, a strong negative wind stress curl near the coast which corresponds to the observations of McClain et al. (1986) along the west coast of Galicia. This feature, may be induced by orographic influences of the rias, and may not be representative of the entire west coast of the IP. However, we can consider this experiment to be process-oriented and focus on the resulting flow field, with the purpose of understanding the effect of these processes in eastern boundary current regions.

Wind velocities are specified to be constant with latitude inside the forcing region. As previously discussed, there is no wind forcing in the northern and southern areas of the model domain.

### b. Experiment 2 (Poleward Wind Followed by Equatorward Wind)

The purpose of this experiment is to simulate a "spring transition" and determine how the flow and temperature fields respond to such a transition. From day 0 to day 20 the model is run with a steady, poleward wind of 900 cm/s (approximately 1.2 $dynes/cm^2$). From day 21 to the end of the model simulation (day 95), the model is forced with an equatorward steady wind of 1425 cm/s (approximately 3.5 $dynes/cm^2$). Values of 1.2 $dynes/cm^2$ and 3.5 $dynes/cm^2$ are thought to be reasonable for peak values of strong

21
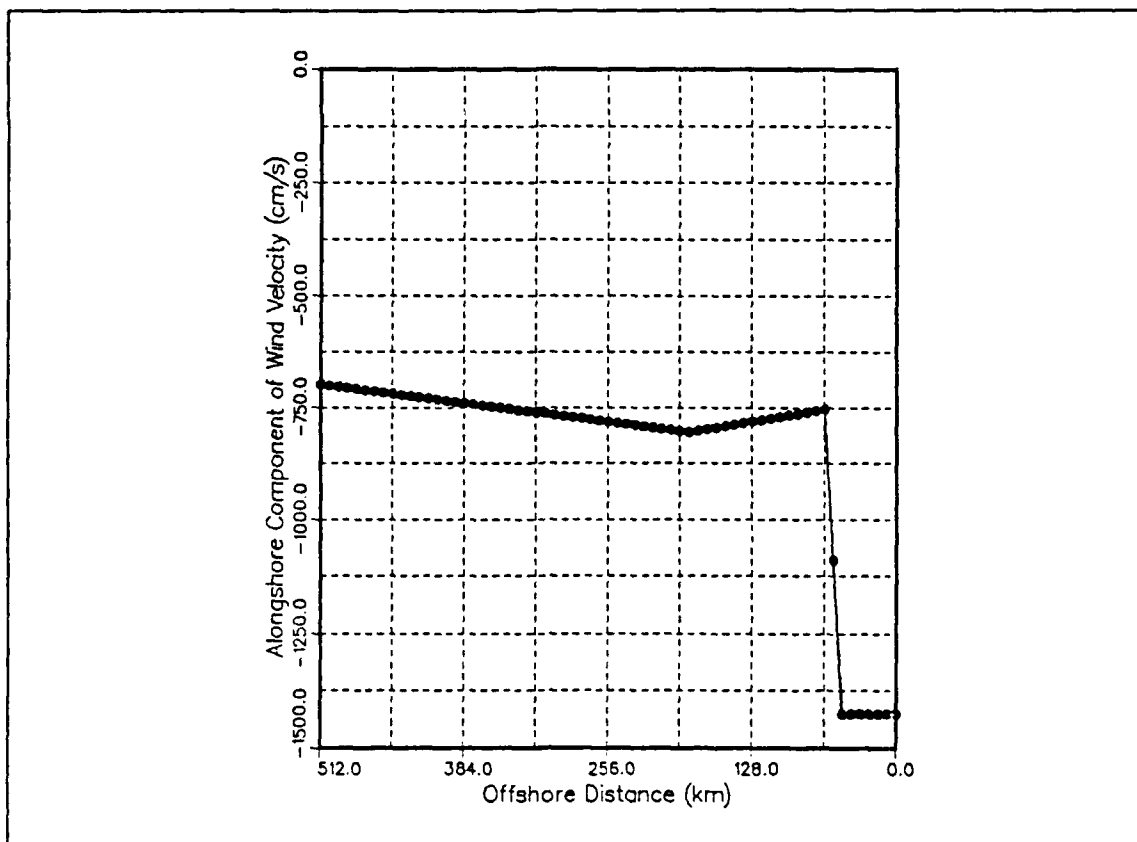
**Figure 12.** Wind forcing for experiment 1

pulses of poleward and equatorward winds, respectively, for pre-upwelling and upwelling seasons. This wind forcing is used here to approximate, in a qualitative sense, the change from a situation of prevailing poleward winds to prevailing and intensified equatorward winds that may happen by March. Note in Figure 3 and Table 4 (Chapter IV) that for the particular year of 1986, the prevailing poleward winds during February change to prevailing equatorward winds by the beginning of March, so that this experiment is not inconsistent with available observations. In other eastern boundary regions, such as off the coast of Oregon, "spring transitions" have been documented to correspond to significant changes in the thermal structure and velocity field over the coastal margin.

22

### c. Experiment 3 (Forcing by a Time Series of the North/South Component of the Wind)

This experiment consists of forcing the PE ocean model with the north/south component of the wind stress, computed from synoptic surface pressure analyses for the period from 1 February to 31 December 1986. This time series (Figure 3) was discussed in section I.B.1. This experiment constitutes the most realistic of the simulations, since it uses "realistic" winds derived from pressure observations in the study area.

# III. APPLICATION OF SPECTRAL ANALYSIS TO THE ESTIMATION OF THE DOMINANT SCALES AND ENERGY OF THE EDDY FIELD

## A. BACKGROUND

In this section we describe the procedure and basis for a program which will be used to estimate the dominant wave lengths and kinetic energy of eddy fields that result from PE ocean model simulations. Spectral analysis is, in general, more suitable to estimate the spectral density function of random stationary processes. However, the method can also be used for deterministic processes, to pick out periodic components in the presence of noise (Chatfield, 1984).

The PE model computes and stores, in memory, daily values for the fields of variables (u,v, and T) at grid points identified by indexes (i,j,k). For variables u and v, both indexes i and j have the integer values 1,2,...,64. For variable T, the indexes i and j have integer values 1,2,...,65. Indexes i and j increase with eastward and northward directions, respectively. Indexes $k = 1,2,...,10$ (associated with the vertical) increase downward. In general (as Chapter IV will show), the resulting eddy fields tend to be generated and concentrated near the coast. The eddies tend to be anisotropic; perturbations develop preferentially along the y direction. For this reason, each spatial series is taken as a sample function corresponding to the values of u,v,T(j) (j = 1,2,...,N), for a given (i,k); That is, discrete values along the northward direction (y) at level (k) and longitude index (i). Since in the model, the maximum j is 65 for temperature and 64 for the velocity components u and v, we used 64 points to compute the discrete Fourier transforms. Figure 13 shows, for purposes of illustration, a typical spatial series for the variable u along a north/south line near the eastern boundary, using data generated in experiment 1. Notice in this particular meridional line that the zonal (u) velocity changes between positive and negative values with magnitudes and spatial scales that correspond to the expected intensity and wave lengths of mesoscale eddies.

Before using the implemented program, one must consider several factors and decide which options to use. For instance, if there is relatively high variance at very low wave numbers and one wants to pick out a relative maximum in the spectrum at low wave numbers, one must consider the use of a prewhitening technique. This technique can help to pick out a relative maximum in the spectrum at higher wave numbers. It can also reduce the leakage of low wave number energy into higher wave number beams in
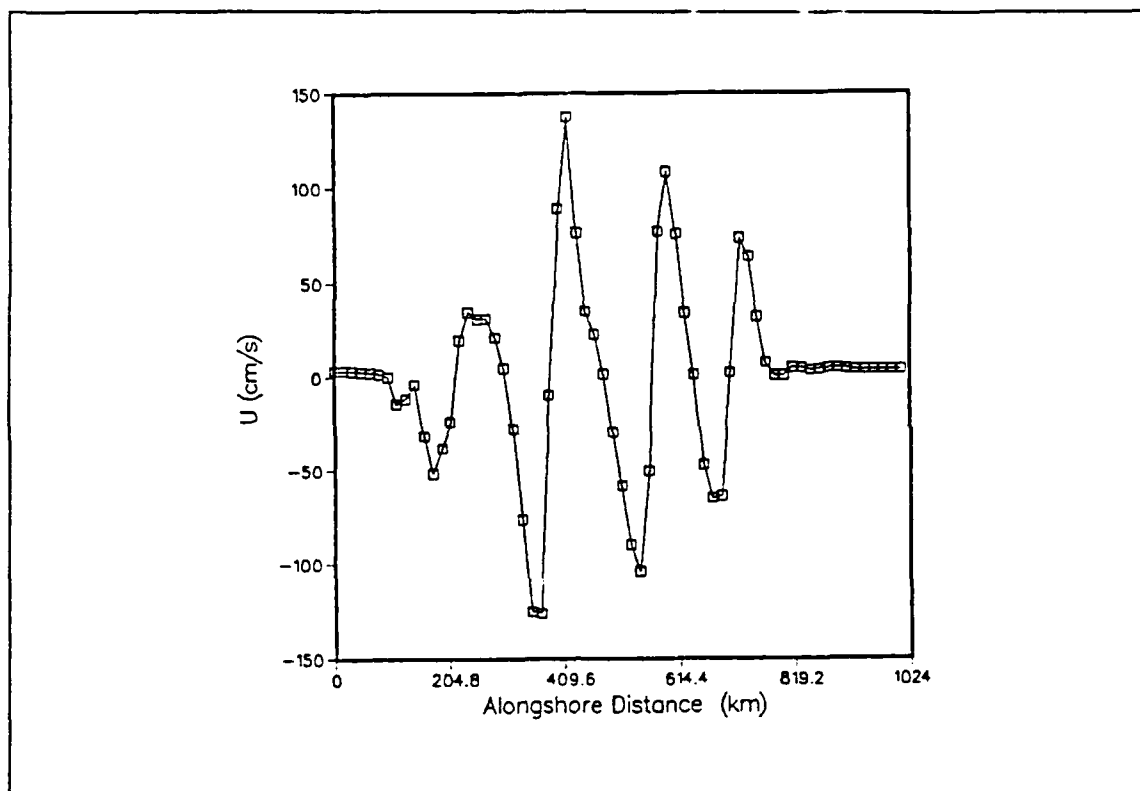
**Figure 13.** A representative spatial series of zonal (u) velocity (cm/s) along a north/south line in the model: The symbols, connected by straight lines, correspond to values of the variable (u) at grid points (i = 55, k = 1, j = 1,2,...,64) for experiment 1, on day 50.

the presence of a very red spectrum (such as in our cases, which have a very red spectrum for the high wave numbers). By differentiating the series, the spectrum can become more nearly white (flat) at the frequencies of interest, and smearing due to leakage of the energy in adjacent wave number beams can be reduced. A particular study case which tests the use of the different options is discussed later in this chapter.

## B.  COMPUTATION OF THE SPECTRAL DENSITIES

An individual spatial series of u,v,T(j) (j = 1,2,...,N), for fixed (i,k) will be referred to as g(j). The mean, $\bar{g} = \frac{1}{N}\sum_{j=1}^{N} g(j)$, is removed from each g(j) to get perturbations $g'(j) = g(j) - \bar{g}$. If a large trend shows up in the values (which usually does not happen in our experiments), $g'(j)$ can be further detrended by subtracting the regression line values from each data point:

25

$$g'_{new}(j) = g'_{old}(j) - (b_0 - my).$$ [17]

The regression line coefficients, $b_0$ and m, are computed by the following formulas :

$$m = \left( \frac{1}{\delta y} \right) \left[ 12 \frac{\sum_{j=1}^{N} y g'(j)}{N(N-1)(N+1)} - 6 \frac{\sum_{j=1}^{N} g'(j)}{(N-1)N} \right]$$ [18]

$$b_0 = \frac{1}{N} \sum_{j=1}^{N} g'(j) - m(N-1)\frac{\delta y}{2}.$$ [19]

In the above formulas, $\delta y$ is the grid spacing along the y direction, $y = (j-1)\delta y$, and $N = 64$ is the number of points in the sample to Fourier transform.

To reduce the leakage problem due to the finite length of the series, one can use a cosine taper, $u_c$, or a Hanning window, $u_h$. The cosine taper window is defined by:

$$u_c(j) = 1 - \cos^2 \left[ \frac{(j-1)5\pi}{N} \right], \quad j \le \frac{N}{10}$$

$$u_c(j) = 1, \quad \frac{N}{10} < j < N - \frac{N}{10}$$ [20]

$$u_c(j) = 1 - \cos^2 \left[ \frac{(N-j)5\pi}{N} \right], \quad j \ge N - \frac{N}{10}.$$

The Hanning window is defined by :

$$u_h(j) = 1 - \cos^2 \left[ \pi \frac{(j-1)}{N} \right], \quad 1 \le j \le N.$$ [21]

Then, $g'_{new}(j) = g'_{old}(j)u(j)$, $(j = 1,2,....,N)$, where $u(j)$ represents either window.

The Fourier transform integral, applied to a finite record $g'(y)$, $0 \le y \le L$, is

$$X(l) = \int_0^L g'(y)e^{-i2\pi ly} dy,$$ [22]

where l is the y component of the wave number vector and $i = \sqrt{-1}$. The above integral can be discretized as

$$X(l) = \sum_{j=1}^{N} g'(j) \exp\left[ -i\frac{2\pi}{L}(l-1)(j-1)\delta y \right]\delta y. \qquad [23]$$

Now, $l = 1,2,...,N$ is the index associated with wave numbers $\frac{(l-1)}{L}$, and $L = (N-1)\delta y$ is the length of the series. Wave number is defined as the inverse of the wave length.

Dividing by $\delta y$,

$$\frac{X(l)}{\delta y} = \sum_{j=1}^{N} g'(j) \exp\left[ -i\frac{2\pi}{(N-1)}(l-1)(j-1) \right], \quad l = 1,2,....,N. \qquad [24]$$

Summation on the right-hand side of (24) is computed by the discrete Fourier transform subroutine for $l = 1,2,....,N$. Values $\frac{X(l)}{\delta y}$ are kept only for $l = 1,2,...,N/2+1$, that is, up to the Nyquist frequency.

The one sided spectral density for the series g(j), at discrete wave numbers is given by

$$G_r(l) = \frac{2[X(l).X(l)^*]}{(N-1)\delta y}, \quad l = 1,2,...,N/2+1. \qquad [25]$$

The subscript r denotes a particular sampling series along grid points $j = 1,2,....,64$ and fixed indexes i,k. A superscript * denotes complex conjugation.

At this point, to compensate for the loss of variance due to the application of a window, $G_r(l)$ is multiplied by a scale factor. The scale factors used are 2.0 and 1.1 for the Hanning window and cosine taper window, respectively, which correspond to the ratio between the areas under the box car function (with a constant value equal to unity) along the record and under the window.

In the case of stationary processes, to increase the confidence on the spectral estimates, the discretized Fourier transform integral is taken over a number of sampling series, NS, and the spectral estimates are averaged :

$$G(l) = \frac{1}{NS} \sum_{r=1}^{NS} G_r(l). \qquad [26]$$

27

Each sampling series contributes two degrees of freedom to the spectral estimates. Because in the PE ocean model the variance of the field variables may change in the region where the individual Fourier transforms are taken, the values G(l) represent how the spatially averaged variance is distributed in the wave number domain in the region of the model being considered.

## C.  PREWHITENING

The procedure for prewhitening consists of differentiating the series in the space domain and, after estimation of the one-sided spectral energy densities for the transformed series, using the transfer function to integrate in the wave number domain, which results in an estimate of the spectrum for the original data series. The application of this technique assumes that $g(j)$ is a stationary process with a continuous power spectrum and that the transformation (differentiation) is stable, that is, the variance of the output is finite. With these assumptions, the relation $G(\omega) = \dfrac{G_{diff}(\omega)}{\omega^2}$ holds (Chatfield, 1984).

The differentiation is approximated by :

$$g'_{diff}(j-1) = \frac{g'(j) - g'(j-1)}{\delta y} , \quad j = 2,3,...,N$$

$$g'_{diff}(N) = 0 .$$

[27]

After computing the spectrum $G_{diff}$, the transfer function, $\omega^2 = [2\pi \dfrac{l}{(N-1)\delta y}]^2$, $l = 1,2,...,N/2+1$, is used to integrate the spectrum of the differentiated series to compensate for the prewhitening :

$$G(l) = \frac{G_{diff}(l)}{\omega^2} .$$

[28]

During the testing of the programs, several cases were run which involved changing the choices of the window (Hanning versus cosine taper) and experimenting with the use of prewhitening versus no prewhitening. Figures 14, 15, 16, and 17, show plots of spectral densities estimated for different combinations of prewhitening, no prewhitening, Hanning window, and cosine taper window. The sampling lines $g(j)$, $j = 1,2,...,64$ correspond in the model domain to indexes $i = 54,55,56,57$, and $k = 1,2$.

To help in the analysis of results regarding the conservation of variance for the different cases, Table 3 shows the values for the ratios of variances associated with u, v, and T, as computed from integrating the averaged spectrum, G(l), and the averaged variances as computed directly from the individual samples, $g'(j)$.

28
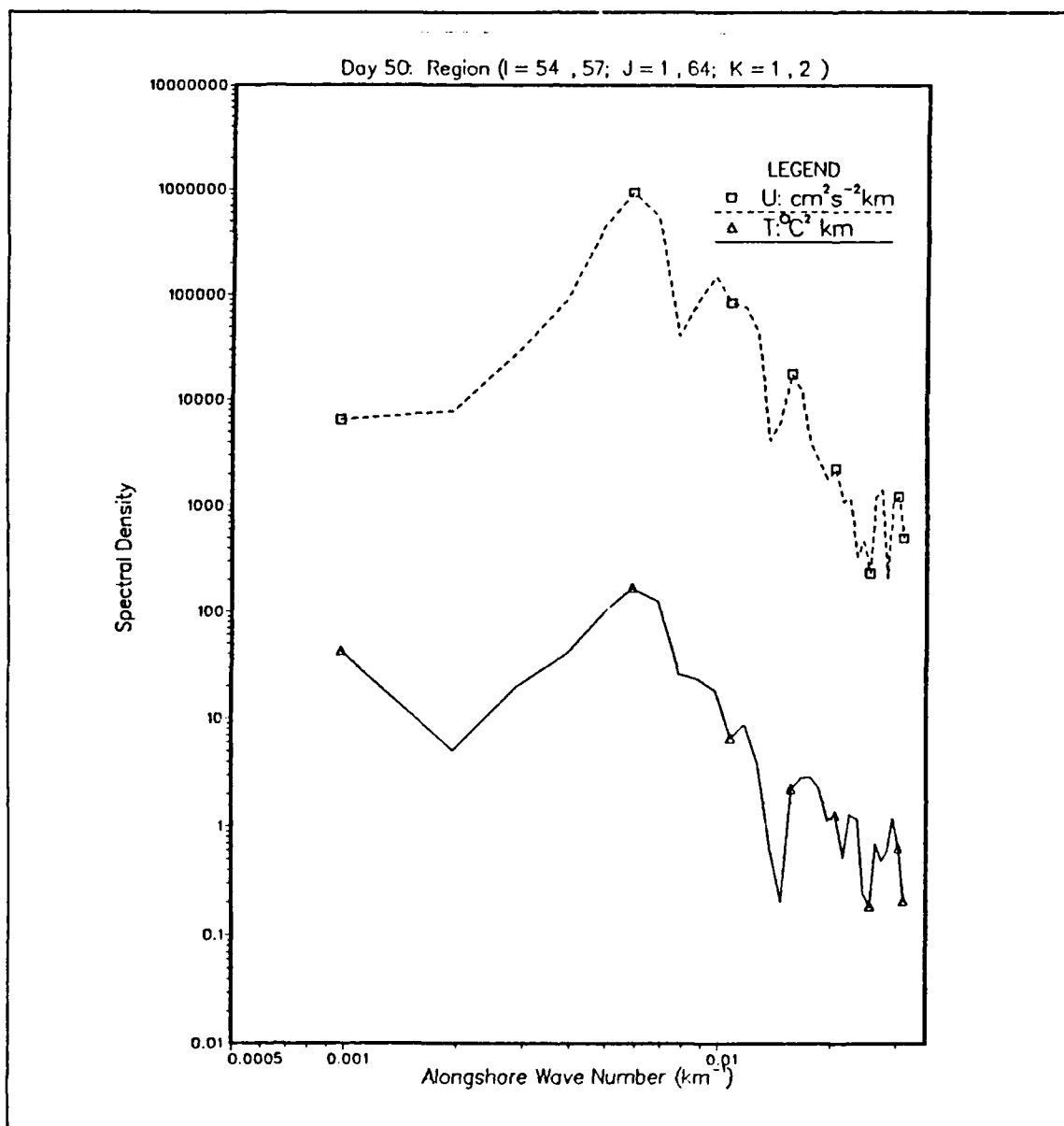
**Figure 14.** Spectral densities with prewhitening and Hanning window, for zonal velocity and temperature for experiment 1 on day 50: Units are $(cm/s)^2 km$ and $(°C)^2 km$ for the spectral densities of velocity and temperature, respectively.
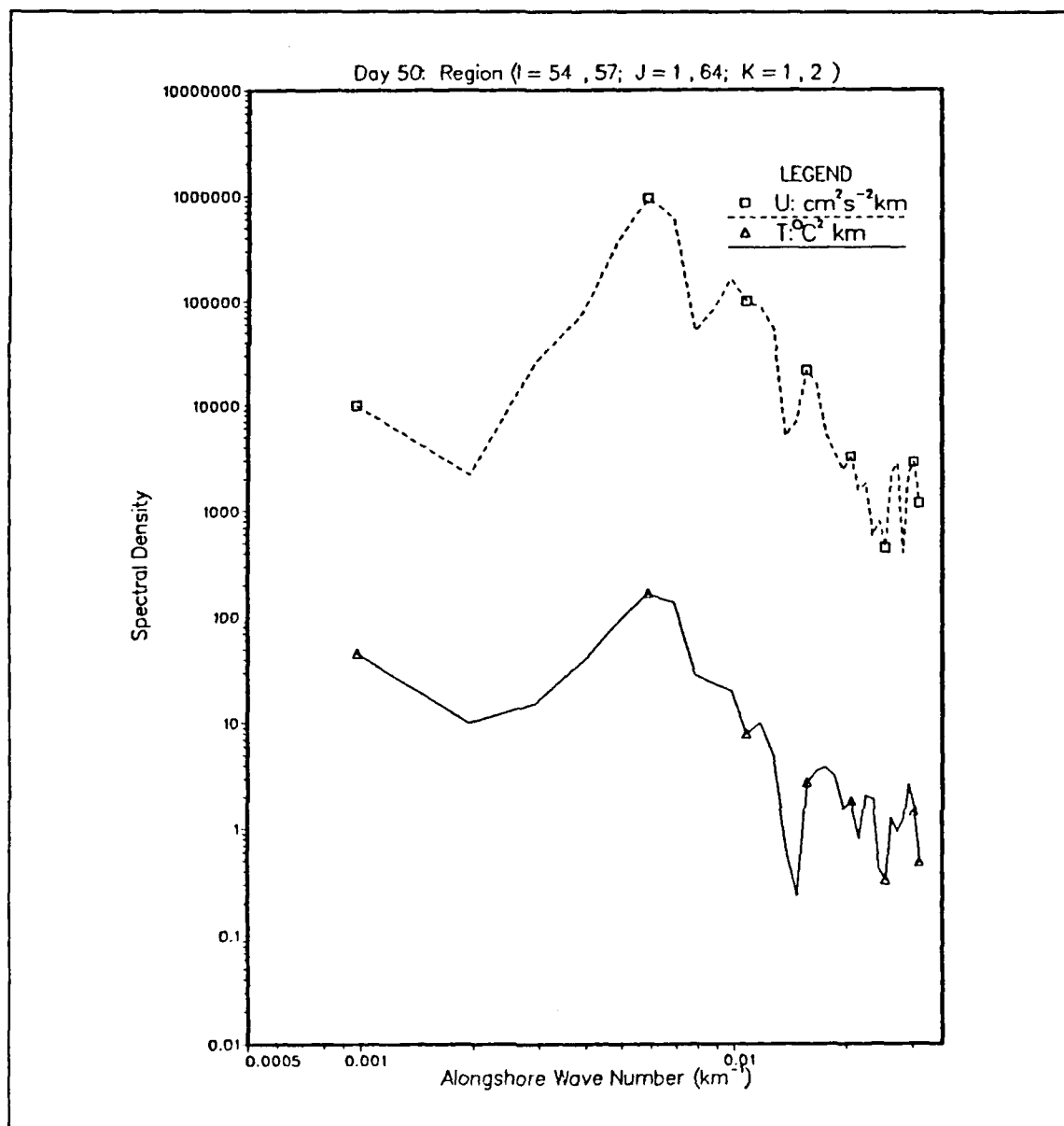
**Figure 15.** Spectral densities without prewhitening but with Hanning window, for zonal velocity and temperature for experiment 1 on day 50: Units are $(cm/s)^2 km$ and $(°C)^2 km$ for the spectral densities of velocity and temperature, respectively.
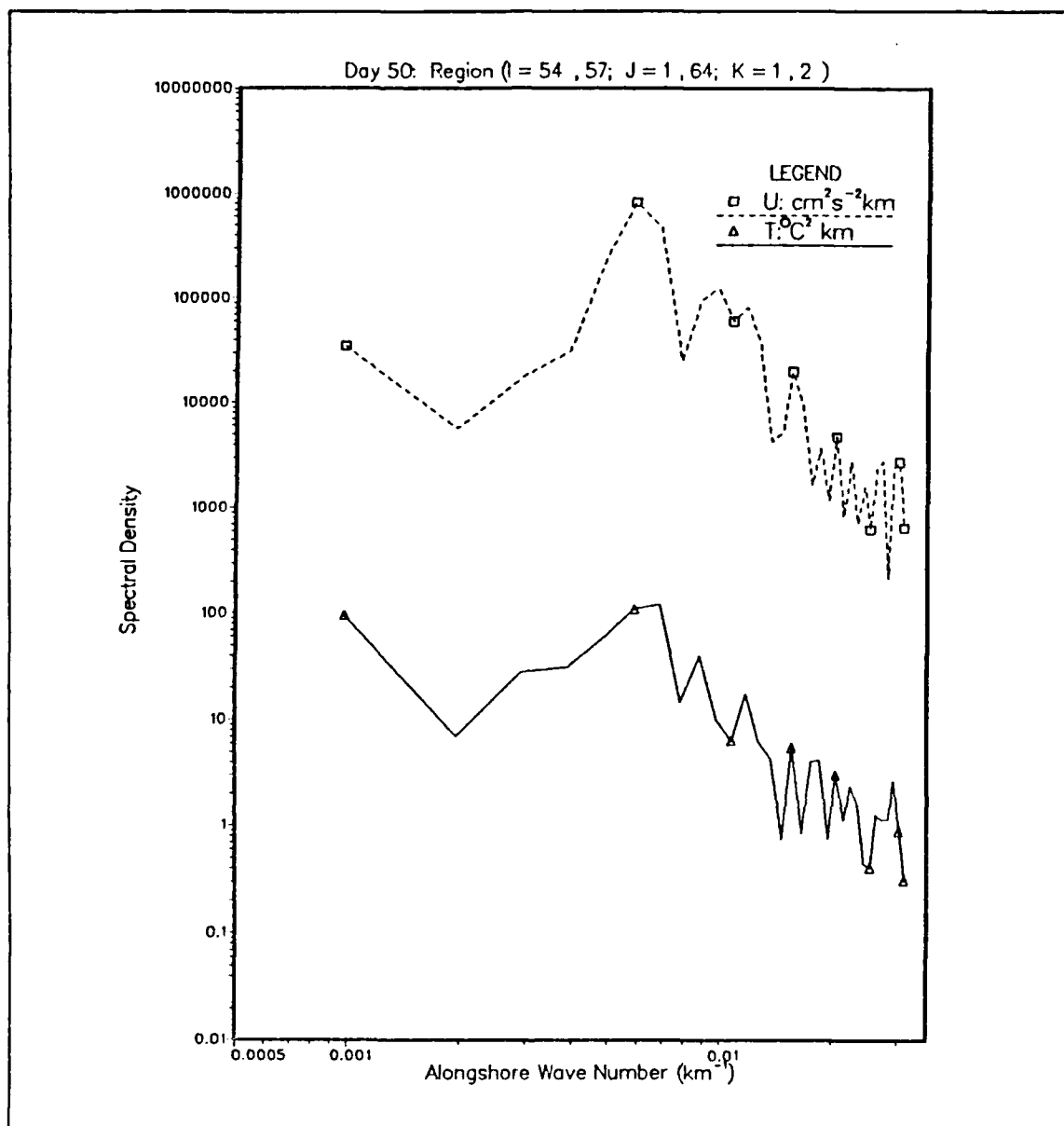
Figure 16.  Spectral densities without prewhitening but with cosine taper window, for zonal velocity and temperature for experiment 1 on day 50:  Units are $(cm/s)^2 km$ and $(°C)^2 km$ for the spectral densities of velocity and temperature, respectively.

31
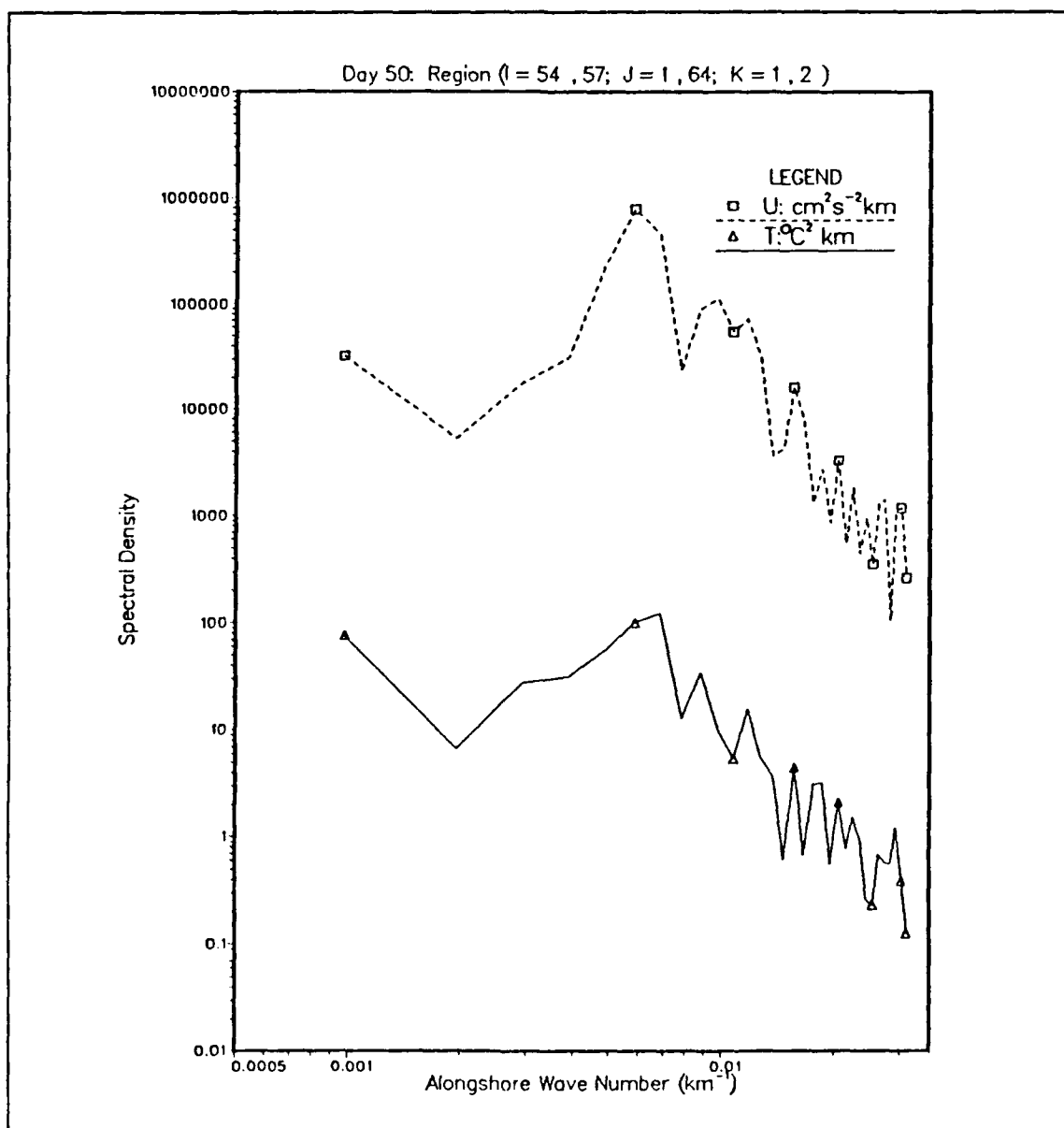
**Figure 17.** Spectral densities with prewhitening and cosine taper window, for zonal velocity and temperature for experiment 1 on day 50: Units are $(cm/s)^2 km$ and $(°C)^2 km$ for the spectral densities of velocity and temperature, respectively.

32

**Table 3. RATIO OF VARIANCES AS COMPUTED FROM THE INTE-GRATION OF THE AVERAGED SPECTRUM AND AS COMPUTED DIRECTLY FROM THE SPATIAL SERIES**

|  | u | v | T |
|---|---|---|---|
| Prewhitening and Hanning | 1.36 | 0.96 | 1.04 |
| No Prewhitening and Hanning | 1.41 | 1.11 | 1.12 |
| No Prewhitening and Cosine Taper | 1.10 | 0.99 | 1.00 |
| Prewhitening and Cosine Taper | 1.05 | 1.18 | 0.91 |

Looking at the summary of results, the cosine taper window does a better job (compared with the Hanning window) in conserving variance in both the prewhitening and no prewhitening cases. Notice that the average value of the ratios shown in Table 3 is closer to unity for the cases using the cosine taper window. In general, the ratios shown in Table 3 are relatively close to unity, except for the variable u in the cases associated with the first two rows of Table 3 (in which a Hanning window was used). In those cases, the values for the ratios are 1.36 and 1.41, and are probably due to overcompensation of variance by applying the scale factor of 2.0 for a Hanning window. From these results it follows that a cosine taper window and no prewhitening should give better estimates for the mean eddy kinetic energy computed by integrating the spectral densities.

From the plots of spectral densities for variables u and T (Figures 14, 15, 16, and 17) one notes the following :

- Comparing cases without prewhitening and with prewhitening using the cosine taper (Figures 16 and 17), it is seen that the shape of the spectrum is about the same; prewhitening does not seem to affect the results in a considerable manner.

- Comparing the cases of no prewhitening using the Hanning window and the cosine taper window (Figures 15 and 16), notice that the Hanning window yields a smoother spectrum at the higher frequencies due to larger suppression of the side lobes in the Fourier transform.

- Comparing the cases of the Hanning window with prewhitening and without prewhitening (Figures 14 and 15), there is not much difference in the shape of the spectrum, except for very low wave numbers. For the very low wave numbers, the prewhitening appears to smooth the spectrum for the variable u but not for T. However, the cosine taper does a better job in separating two peaks at very close frequencies (resulting in better resolution) due to a narrower main lobe of the Fourier transform of the cosine taper window compared with that of the Hanning window.

33

From the above considerations, it is suggested that if one desires to pick out the relative maximum from the spectrum, one may get better results using a Hanning window either with prewhitening or without prewhitening, since it does a better job in reducing leakage, unless the relative maxima are very close in wave number (the use of a logarithmic scale helps to show more detail in the spectrum over a wider range of wave numbers, compared to a linear scale).

## D. EDDY KINETIC ENERGY

Having computed the spectral densities for fluctuations $u'$, $v'$, and $T'$, for a given region in the model, and for a given day, we may look towards the computation of the daily sequence of the spatial mean eddy kinetic energy. To do this, take $\sigma^2_{u,v} = \sum_{l=1}^{N/2-1} G_{u,v}(l)\delta l$ to approximate $KE'_{u,v}$. The value, $\delta l = \dfrac{1}{L}$, is the wave number resolution, and $KE'_{u,v}$ represents the contributions of $u',v'$ to the mean eddy kinetic energy. Then $KE'_{total} = \sigma^2_u + \sigma^2_v$ represents the spatial mean (in the region defined by i,j,k) eddy kinetic energy associated with both $u'$ and $v'$ (an example is shown in Figure 18). If one desires the eddy kinetic energy for interpretation of experimental results, it is more accurate to compute the energy directly from the fields of u and v, rather than by integrating the spectral densities.

A daily sequence of the spectral estimates for $u'$ is shown in Figure 19. The choice of a linear rather than a logarithmic scale allows easier visualization of the dominant peaks. The combination of Figure 18 and Figure 19 shows very clearly how the spatially averaged eddy kinetic energy and dominant wave lengths can change with time for a given region of the model, for a particular simulation.

34

**EDDY KINETIC ENERGY**
i from 6 to 64 , j from 1 to 64 , k from 1 to 1, experiment 1
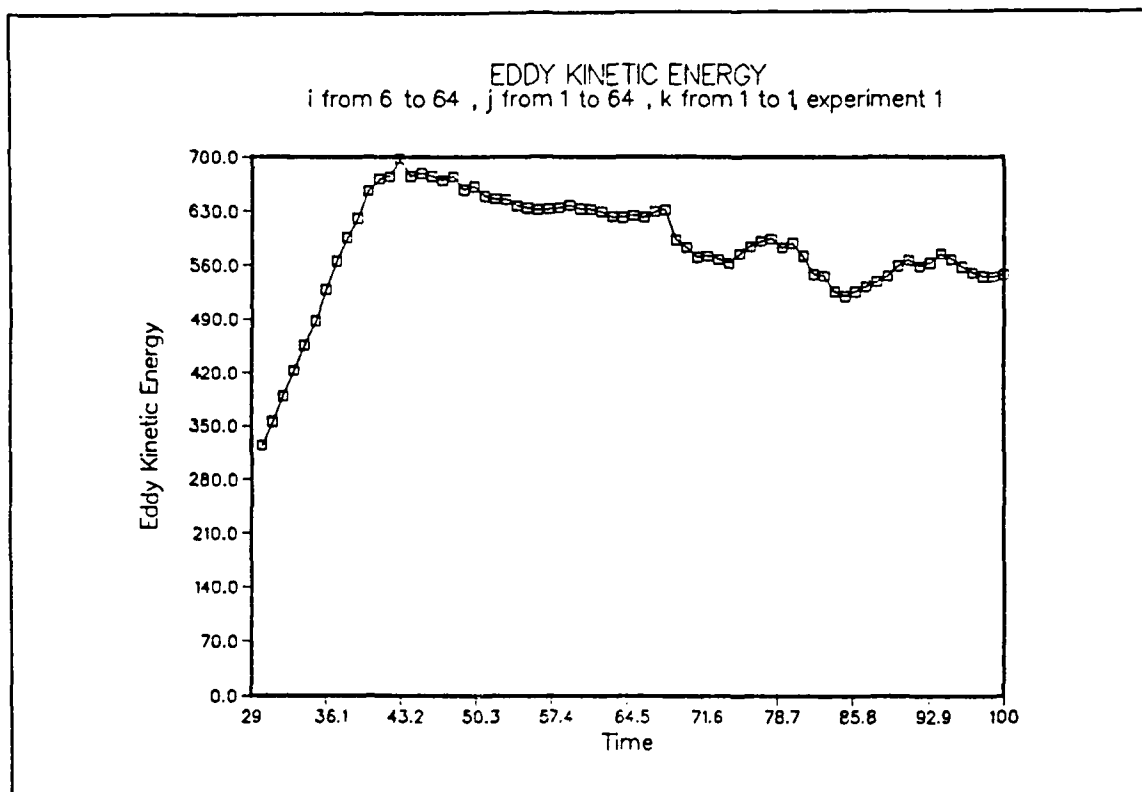
Figure 18. Time sequence of eddy kinetic energy computed by adding the integrated, spatially averaged spectral densities of zonal (u) and meridional (v) components of the velocity: Units are $cm^2\,s^{-2}$ for eddy kinetic energy and days for time.
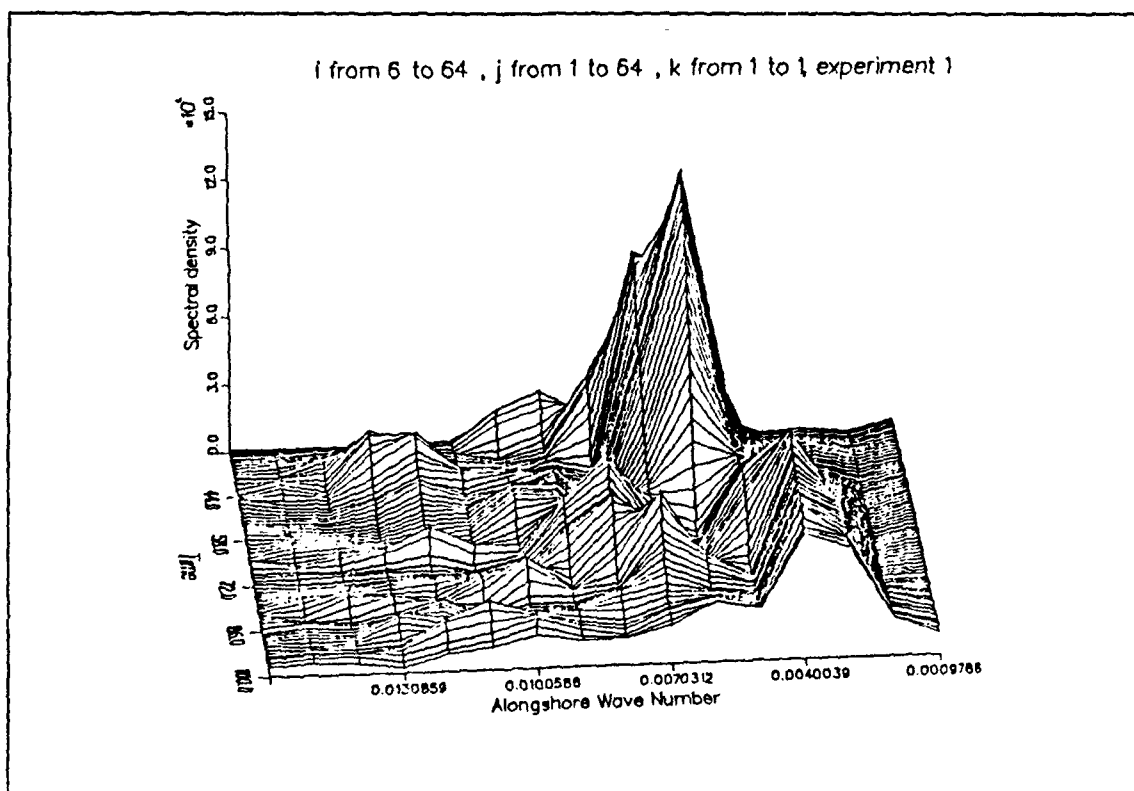
**Figure 19.** Time sequence of the spectral densities of variable (u), constructed by averaging the spectral densities of alongshore lines of grid points for experiment 1, from day 30 to 100: Units are $(cm/s)^2 km$ for the spectral densities of the (u) velocity and days for time.

# IV. RESULTS OF WIND FORCING EXPERIMENTS

## A. STEADY WIND FORCING EXPERIMENT

### 1. Experiment 1 (Large Negative Wind Stress Curl near the Coast)

A similar experiment was conducted by McClain *et al.* (1986) to study the flow field forced by of a negative wind stress curl observed off the west coast of Galicia. The diagrams of the applied wind forcing and the resulting current velocity field and interfacial displacements for the McClain et al. (1986) experiment, are shown in Figures 20 and 21. The southward flow adjacent to the coast was driven by the southward coastal wind and the northward flow offshore was associated with the negative curl of the wind stress (McClain *et al.*, 1986). This same type of structure in the wind field was used in experiment 1 for the study region off the west coast of the IP.

In experiment 1 the wind forcing (Figure 12) consisted of: a large negative wind stress within 48 km of the coast; a large negative wind stress curl in the band between 48 and 64 km from the coast; a positive wind stress curl between 64 and 184 km; and offshore of 184 km, a negative curl, the latter structure based on the climatological wind stress curl for the IP during the upwelling season (Bakun, 1987). These winds change only in the cross-shore direction and are steady in time. As in all other experiments, only the alongshore component of the wind is used.

### a. Development of the Coastal Jet and Offshore Countercurrent

On day 5, due to the equatorward wind stress, a surface westward flow (Figure 22 (left)) results, due to Ekman transport away from the coast, as expected. The largest negative values (magnitudes over 10 cm/s) for the flow are seen in a meridional band with its axis located approximately 60 km from the coast. Also seen in Figure 22 (right) is the surface dynamic height field (relative to 2400 m), which shows a ridge, with its axis extending alongshore approximately 55 km from the coast. A cross-section taken in the middle of the domain (Figure 23), shows that the upper ocean isotherms slope downward toward the coast at distances between approximately 82 and 57 km from the coast and slope upward within 57 km of the coast. The opposite slopes for the isotherms fall in regions where the gradient ($\frac{\partial u}{\partial x}$) at the surface has opposite signs (compare Figure 23 and Figure 22 (left)). The change in sign of the zonal gradients of the surface dynamic height field, of the zonal velocity, and of the upper ocean temperature field, corresponds to the region where the wind stress curl is negative (i.e., between 48 km and

37
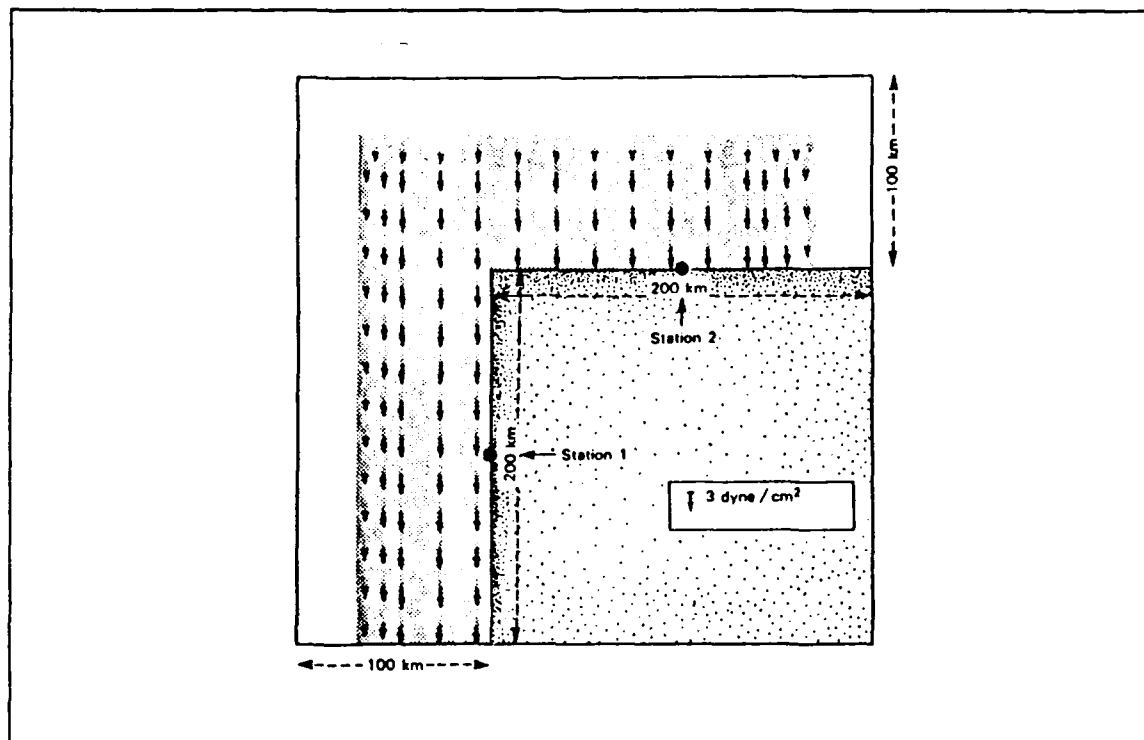
**Figure 20.** Numerical model basin geometry and the definition of the southward wind field applied in the simulation of McClain et al. (1986).

64 km from the coast). The upwelled isotherms near the coast are consistent with a divergence of the flow in the Ekman layer under the influence of the equatorward wind with a compensating vertical motion to replace the surface water. Farther offshore, with the decreasing velocities of the equatorward wind, the offshore Ekman transport is reduced resulting in surface layer convergence and downwelling consistent with the pattern of isotherms seen in Figure 23. Because the surface dynamic height field is computed by vertically integrating the specific volume anomaly (which is directly proportional to the temperature), the ridge shown in Figure 22 (right) coincides with the location where upper ocean isotherms have a maximum downward displacement. Further, the region of imposed negative wind stress curl (distances from the coast between 48 and 64 km) coincides with the locations of both the ridge of the surface pressure and the change in sign of the slopes of the upper ocean isotherms. The pressure gradient force, due to the surface slope and horizontal gradient of temperature density, changes in sign across this region of negative wind stress curl so that there results an equatorward surface jet within
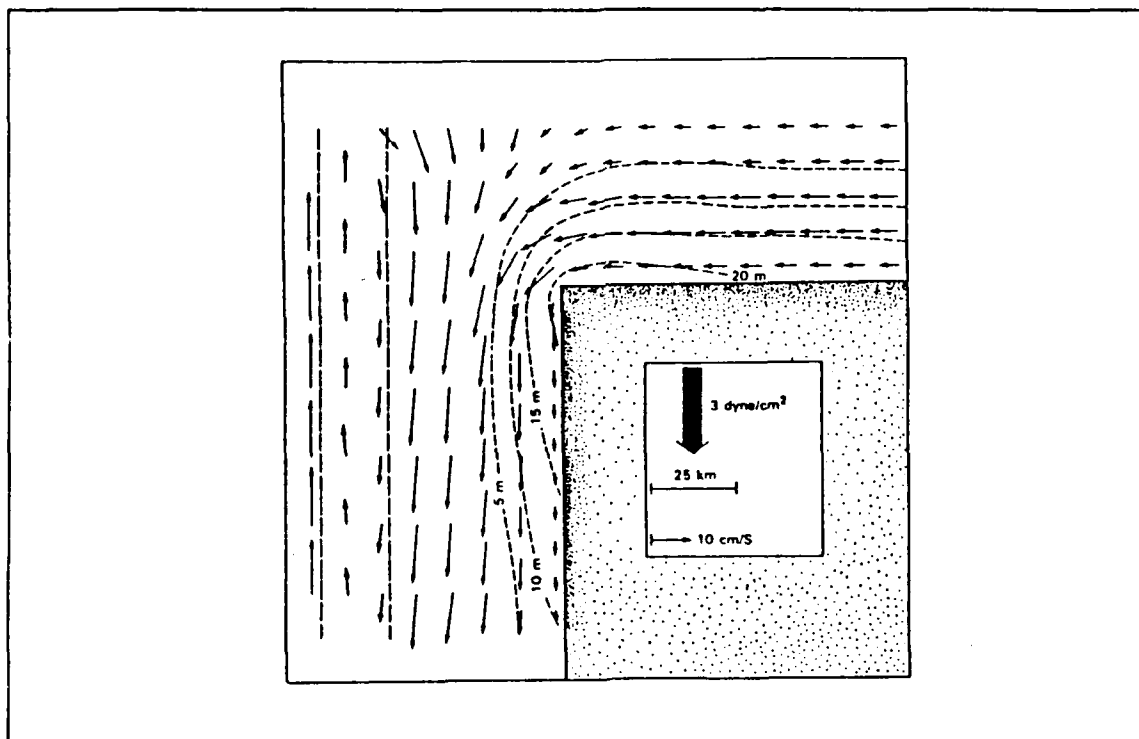
**Figure 21.** The flow field and pycnocline displacement resulting from the wind forc-
ing shown in **Figure 20:** Dashed lines are lines of constant displace-
ment of the interface, and the shaded area defines the area of strong
wind stress curl. The maximum wind stress is 3 $dynes/cm^2$ (from
McClain et al., 1986).

approximately 55-60 km from the coast and a poleward surface jet offshore. This is
clearly identified in a zonal vertical section of the alongshore averaged v component of
the velocity (Figure 24), which shows the separation between jets at about 57 km from
the coast. The equatorward jet has an alongshore averaged maximum of about 30 cm s
at 10 km from the coast, and a depth of about 320 m. The poleward jet has a maximum
alongshore averaged velocity of about 15-20 cm/s at 67 km from the coast and a vertical
extent of approximately 220 m. Results of this experiment on day 5 are qualitatively
consistent with the results of McClain et al. (1986), in which the currents forced under
a similar wind field reached a maximum so ·hward speed of 15 cm s shoreward of the
wind shear zone and a maximum northward speed of 14 cm s offshore of the zone.
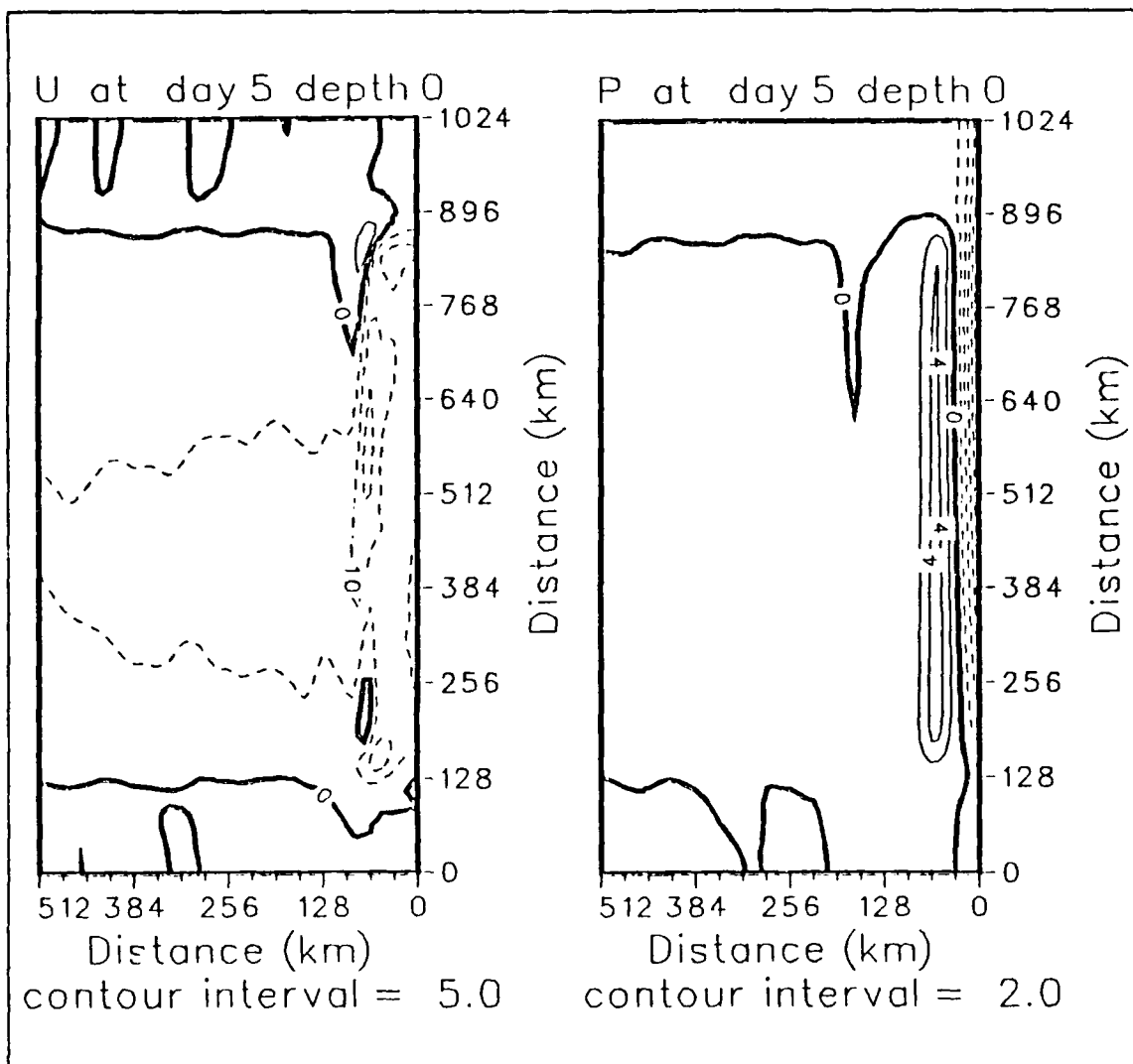
**Figure 22.** Surface isopleths of (left) zonal (u) velocity (cm/s) and (right) dynamic height (cm) relative to 2400 m for experiment 1 at day 5: The contour interval is 5.0 cm s for velocity and 2.0 cm for dynamic height. Dashed lines denote offshore velocities and negative values relative to 2400 m.

By day 20, the coastal equatorward surface jet, within 60 km of the coast, has an intensified maximum alongshore averaged speed of about 60 cm s and has deepened its vertical extent to about 860 m depth. The poleward jet also has an increased maximum alongshore average speed of about 35-40 cm s, and has increased its cross-sectional area by deepening to 560 m depth, and widening to about 123 km from
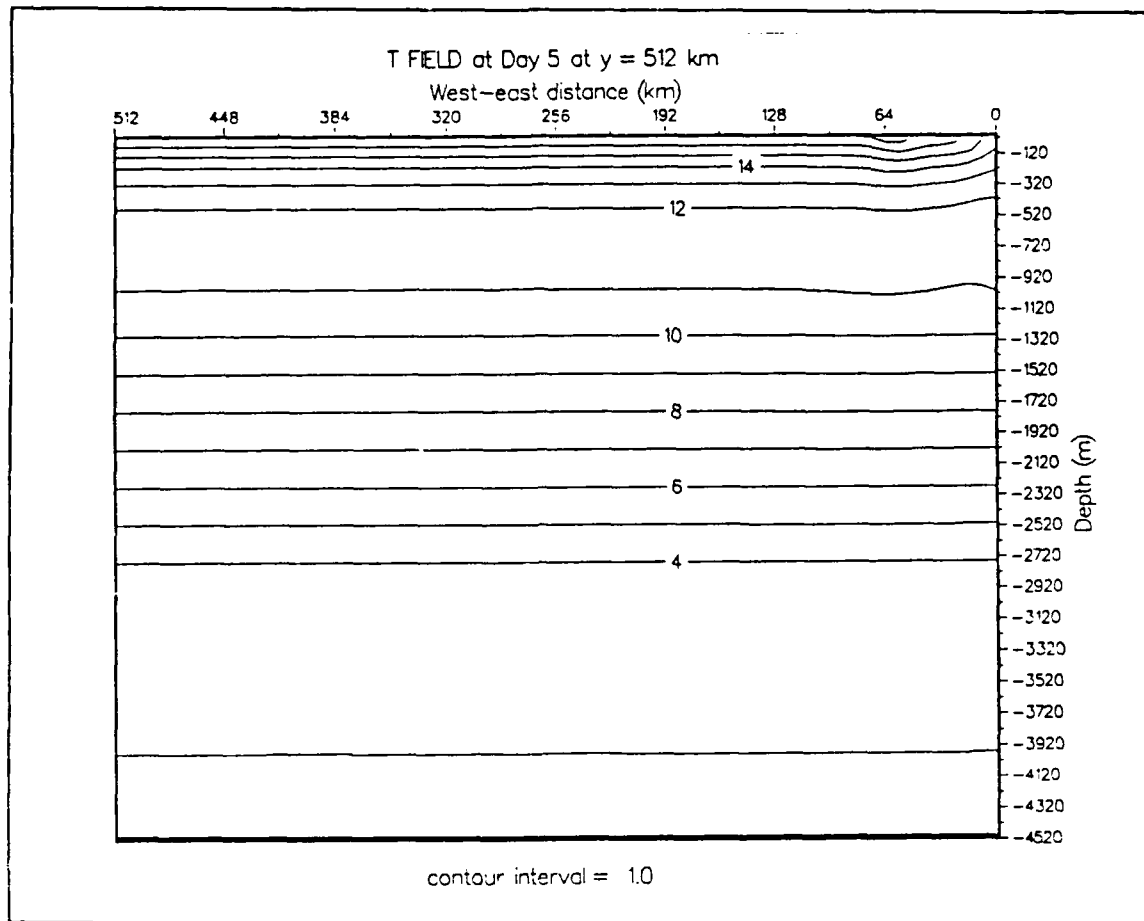
**Figure 23.** **Vertical cross-shore section of temperature (°C) at** y = 512 km **for experiment 1 at day 5:** Contour interval is 1.0°C.

the coast. A new, although weak (approximately 5 cm/s), feature in the system is a poleward undercurrent, which shows up adjacent to the coast between approximately 200 and 500 m (Figure 25). The equatorward surface flow and poleward undercurrent, which result from forcing by an equatorward wind stress in the coastal region, are consistent with the results of McCreary *et al.* (1987) and Batteen *et al.* (1989).

### b. The Generation of Eddies

Superimposed on the dominant poleward and equatorward surface jets (Figure 26 (left)) are eddies, as seen in the surface zonal current field (Figure 26 (right)) at approximately y = 735 and y = 191 km. These perturbations are confined to within 120 km of the coast in the same region as the poleward and equatorward jets as shown in Figure 26(left).

**V FIELD at Day 5 longshore ave.**
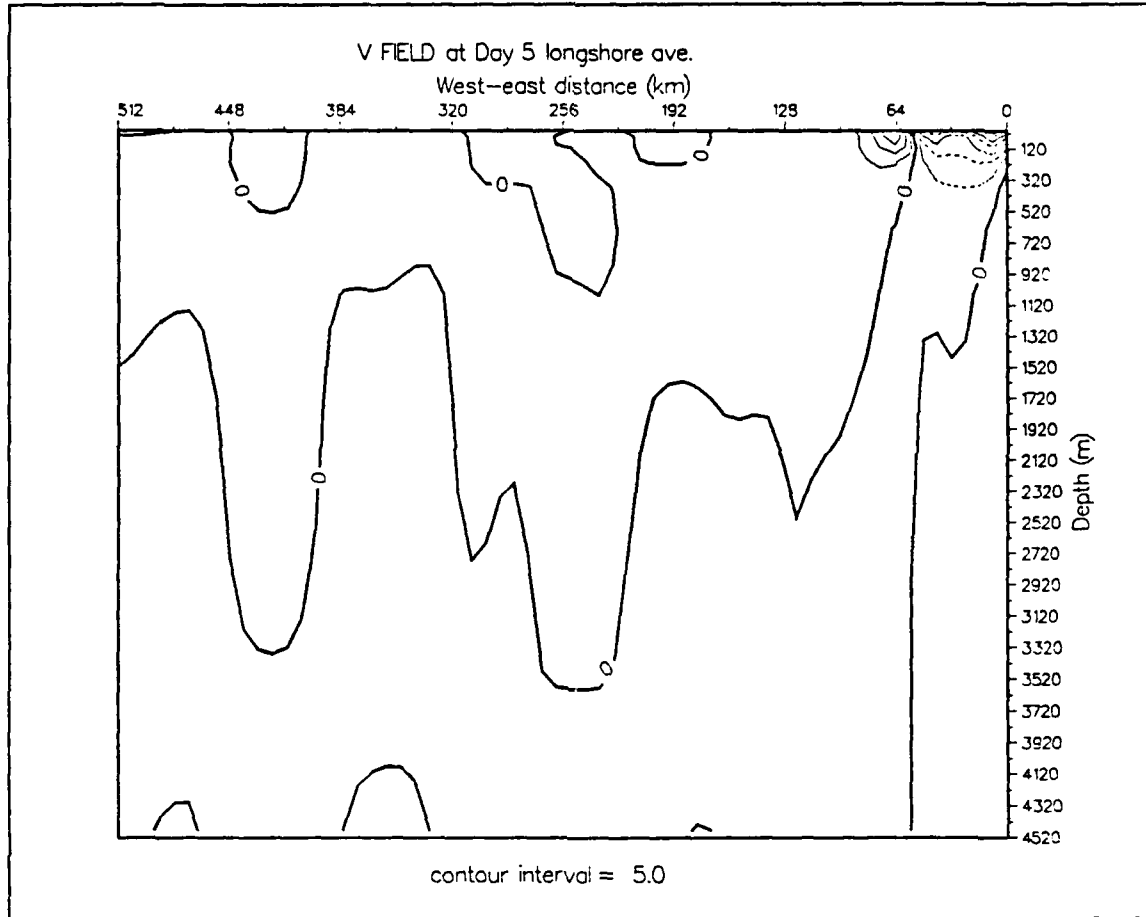
**Figure 24.** Vertical cross-shore section of alongshore-averaged meridional (v) velocity (cm/s) for experiment 1 at day 5:  Contour interval is 5.0 cm/s. Dashed lines denote equatorward flow.

Following Batteen *et al.* (1989), we investigate the necessary conditions for instability by examining the distribution of potential vorticity, q, in time-averaged cross-sections of the coastal flow.  Following Watts (1983), the potential vorticity, q, may be approximated by the expression:

$$q = (f + \zeta) \frac{\partial T}{\partial z} - \frac{\partial T}{\partial x} \frac{\partial v}{\partial z}, \qquad [29]$$

where $\zeta = \frac{\partial v}{\partial x} - \frac{\partial u}{\partial y}$.  A cross-section of the time-averaged (days 21-30) potential vorticity at y = 768 km, is shown in Figure 27.  The choice of days 21 through 30 for the time averaging corresponds to the period in which the instabilities developed.  Away

42

**V FIELD at Day 20 longshore ave.**

West—east distance (km)

contour interval = 5.0
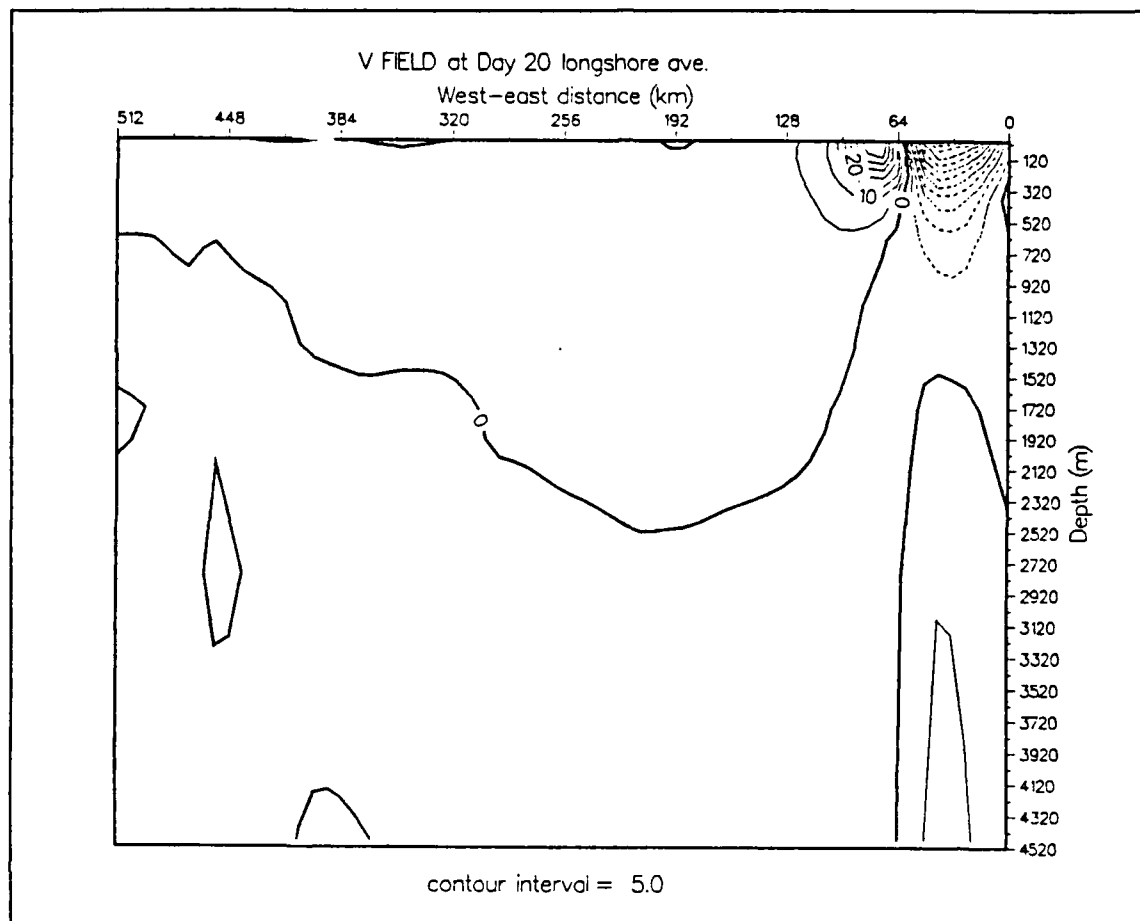
**Figure 25.** Vertical cross-shore section of alongshore-averaged meridional (v) velocity (cm/s) for experiment 1 at day 20: Contour interval is 5.0 cm s. Dashed contours denote equatorward velocities.

from the coastal region, there is a tendency for potential vorticity to be uniform along isothermal surfaces and to change vertically, consistent with the temperature stratification (not shown). A relative maximum of potential vorticity is present at a depth of about 85 m, corresponding to the seasonal thermocline (i.e., the maximum vertical gradient of temperature). In the upper ocean, within 128 km of the coast, the distribution of isolines of potential vorticity is complicated by large horizontal gradients of temperature and velocity shears. The cross stream derivative of potential vorticity (calculated by computing the horizontal derivative ($\frac{\partial q}{\partial x}$) and then multiplying by one grid length ($\delta x$) ) changes sign in the upper ocean (Figure 28), at a distance of 54 km from the coast, corresponding well to the axis where the anticyclonic eddies are gener-
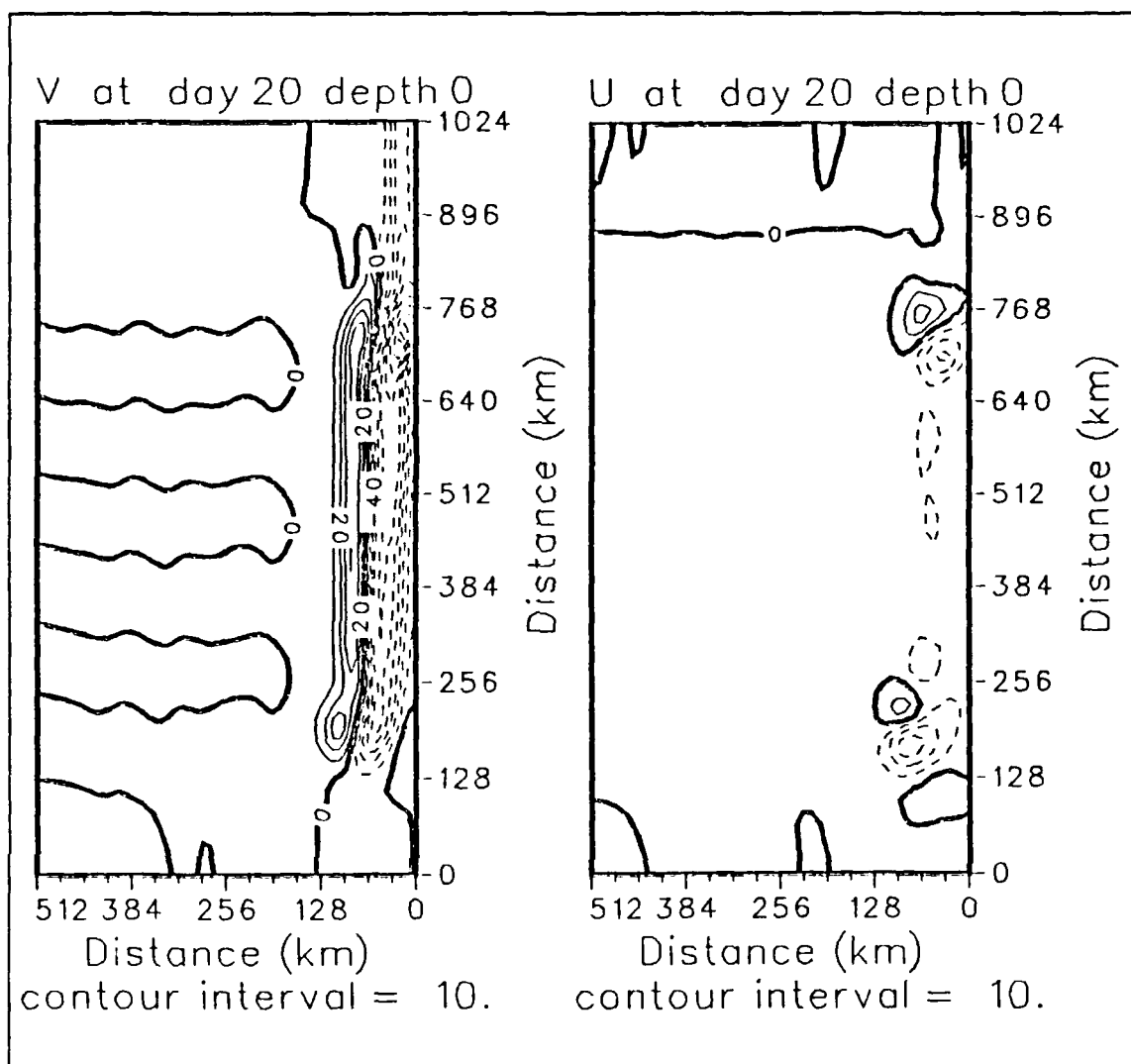
**Figure 26.** Surface isopleths of (left) meridional (v) velocity (cm/s) and (right) zonal (u) velocity (cm/s) for experiment 1 at day 20: Contour interval is 10.0 cm s. Dashed lines denote equatorward and offshore velocities.

ated in the experiment. Because there is a sign change in the zonal direction at this distance from the coast, which satisfies a necessary condition for barotropic instability, barotropic instability is likely the main mechanism for the generation of the anticyclones in experiment 1. Note however, that there is also a sign change in the vertical direction, which satisfies a necessary condition for baroclinic instability. As a result, mixed

(barotropic and baroclinic) instability could lead to the generation of eddies in this experiment.

### c. The Eddy Fields

By day 40, the surface dynamic height field (Figure 29 (left)) shows the existence of four, well developed anticyclonic eddies with center positions at y ~ 252, 438, 604, and 755 km. Because the centers of the eddies nearly coincide with the zone of large negative wind stress curl, the four anticyclonic circulations are likely generated due to the anticyclonic shear of the wind in this region. The three northernmost eddies have circular patterns, with diameters of approximately 147 km, while the southern eddy has an elliptical pattern, with its major axis oriented northeast/southwest. All of the eddies have warm cores (consistent with warm core rings) as seen in Figure 29 (right) and in Figure 30 for the eddy located at y ~ 624 km. The near-surface isotherms associated with the eddies show considerable downward displacements. For instance, as shown in Figure 30, the 17°C isotherm surrounds the eddy at the surface, and is displaced downward to 186 m. The surface temperature pattern (Figure 29 (right)) has four cold water filaments corresponding to places where the circulation of each of the four anticyclones advects the upwelled coastal water offshore. The southern filament is the largest, advecting relatively cold water (below 15.0°C) as far as 185 km offshore.

The spectral densities of the fluctuations of u,v, and T associated with the alongshore component wave number were computed by sampling the fields at the model grid points (upper level, $0 \leq y \leq 1008$ km, distances from the coast between 32 km and 256 km) corresponding to the region with the most eddy activity and are shown in Figure 31. Notice that the peaks of the spectra for u,v, and T show the same alongshore spatial scales. The dominant meridional wave number is approximately 0.0065 $km^{-1}$, which corresponds to a wave length of 154 km. This agrees with the scales of the eddies seen in the surface dynamic height field (Figure 29(left)).

By day 60, the two northern and the two southern eddies have merged coalesced into one northern and one southern eddy (Figure 32 (left)). The dominant alongshore wave number of the eddies (Figure 33) is 0.006 $km^{-1}$ (alongshore wave length of 166.7 km). The resultant eddies continue to enlarge, as shown for day 90 (Figure 32 (right)). This expansion is also seen in the time series of daily spectral densities of the u component of the velocity field (Figure 34).

Note that the southern eddy extends farther offshore than the northern eddy. This can be explained by the $\beta$-effect. The two anticyclones propagate westward at estimated rates of about 1.4 km day and 2.3 km day for the northern and southern
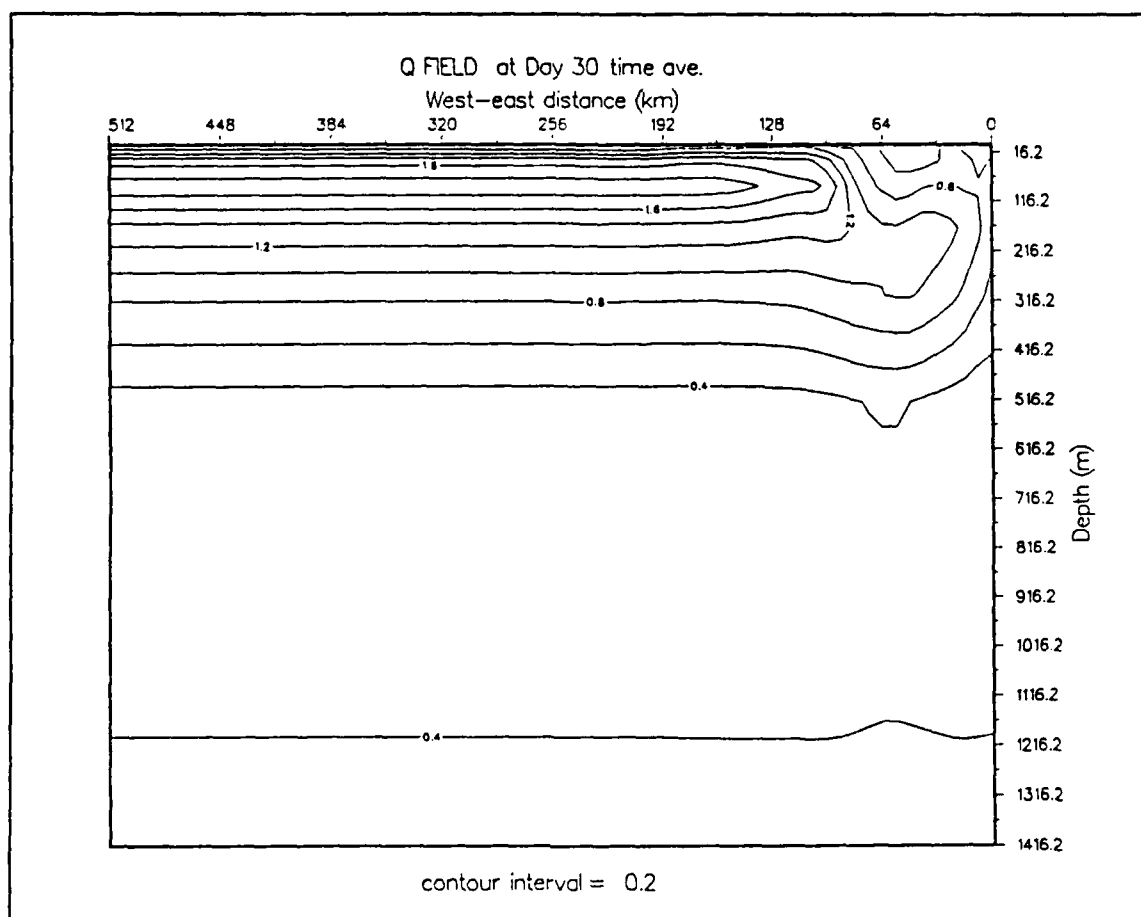
**Figure 27.** Vertical cross-section of potential vorticity (°C /(m s)) for the time-averaged days 21-30 of experiment 1: Values are scaled by $10^6$. Contour interval is 0.2°C / (m s). The vertical cross-section was taken at $y = 768$ km.

anticyclones, respectively. The faster rate of the southern eddy is consistent with a $\beta$-induced motion, i.e., $\beta$ is larger at lower latitudes.

By day 90, the size of the eddies has stabilized. The diameter of the eddies, defined by the 10 cm dynamic height contour, is approximately 166 km (Figure 32 (right)), while the dominant meridional scale of the eddy field is around 300 km, which corresponds to an alongshore wave number of 0.0033 $km^{-1}$, as shown in the spectral density distribution (Figure 35). A vertical zonal section in the middle of the domain shows the thermal structure of the northern warm core ring as a relatively large downward displacement of the upper ocean isotherms (Figure 36). For instance over a zonal
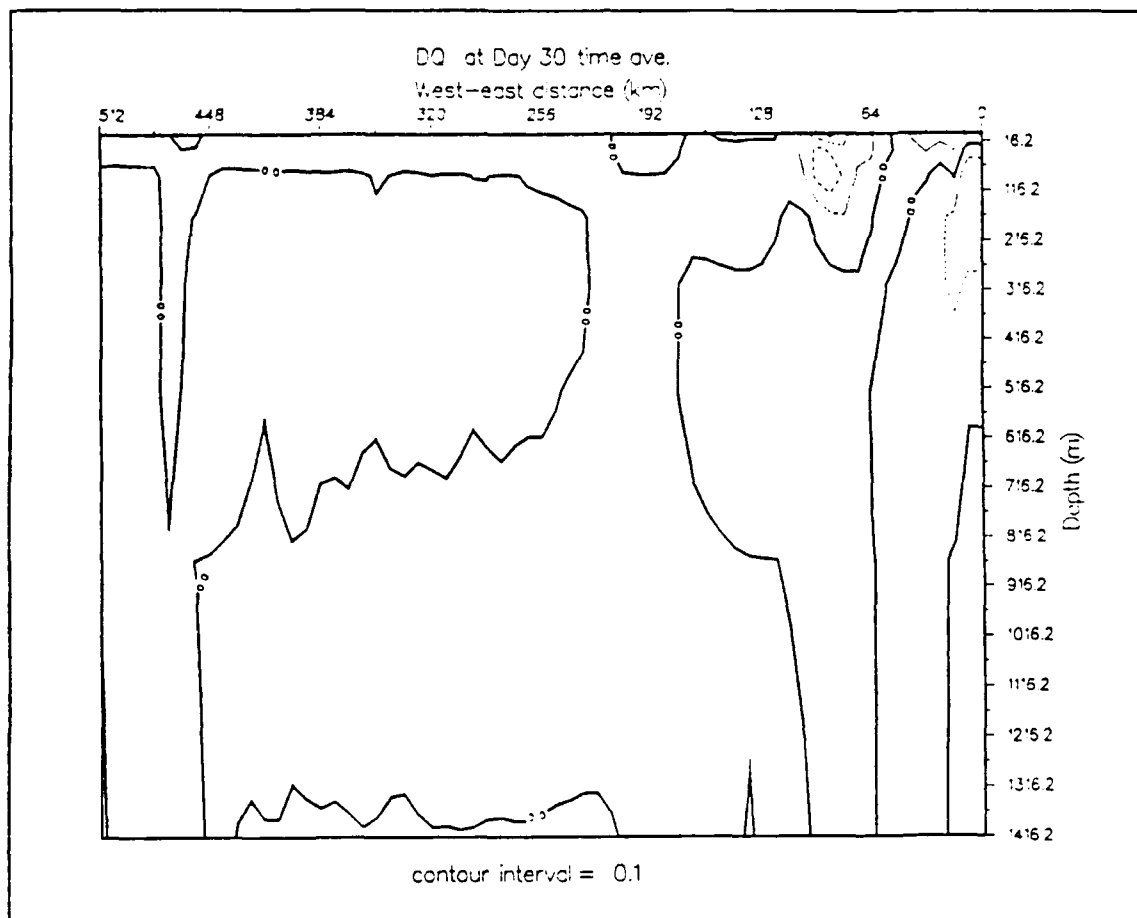
**Figure 28.** Vertical cross-section of the cross-stream derivative of potential vorticity multiplied by the zonal grid size (°C / (m s)) for the time-averaged days 21-30 of experiment 1: Values are scaled by $10^6$ . Contour interval is 0.1°C / (m s). Dashed contours denote negative values. The vertical cross-section was taken at y = 768 km.

distance of 74 km, the 17°C isotherm bends down from the surface to 223 m and then bends up to the surface. This thermal structure represents a considerable amount of available potential energy for converting to kinetic energy associated with this particular eddy. The vertical structure of the v component of the velocity at the same alongshore location (Figure 37) is consistent with the thermal structure (via the thermal wind relation), and shows a poleward flow west of the center position of the eddy (located at 150 km from the coast) and an equatorward flow on the eastern side. In addition, there is a coastal surface jet coincident with the upward slope of isotherms in the nearshore

47
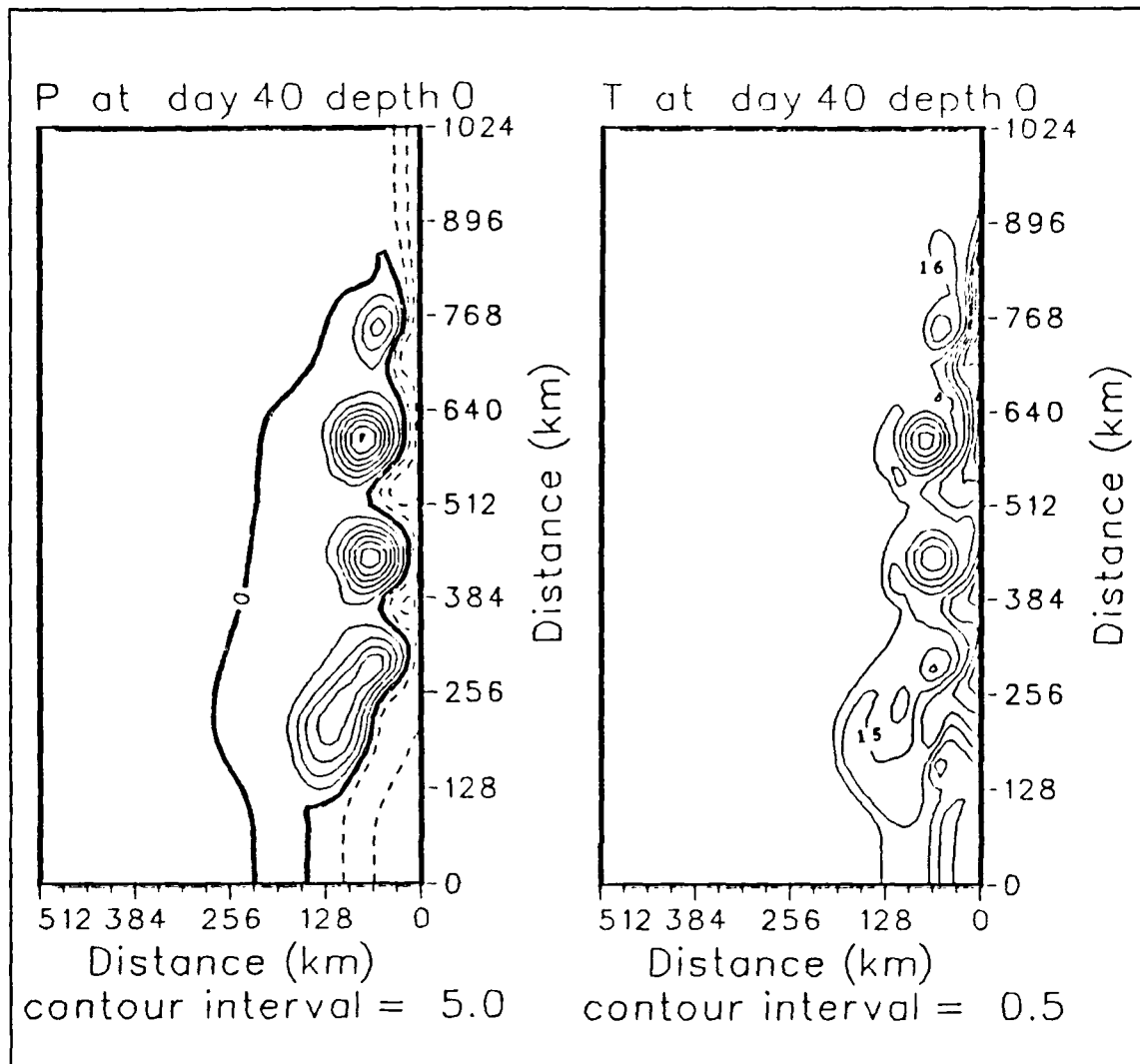
**Figure 29.** Surface isopleths of (left) dynamic height (cm) relative to 2400 m and (right) temperature (°C) for experiment 1 at day 40: Contour interval is 5.0 cm for dynamic height and 0.5°C for temperature. Dashed contours denote negative values relative to 2400 m.

region. This jet, which has a maximum surface velocity of about 60 cm s, interacts with the offshore southward flow of the anticyclonic eddy circulation (at approximately 67 km offshore) resulting in a deep southward flow at this position (v is larger than 10 cm s as deep as 1300 m). By day 90, a plume of cold water (temperatures less than 16°C extending approximately 250 km offshore) lies between the two anticyclones at y = 416 km

48

**Figure 30.** Vertical cross-shore section of temperature (°C) at y = 624 km for experiment 1 at day 40: Contour interval is 1.0°C.

(Figure 38), and appears to have been advected by the southward branch of the northern eddy. A zonal section of the temperature field across the cold filament shows sinusoidal-like isotherms superimposed on a general upward sloping towards the coast (Figure 39). A cold dome (with an upward displacement of the 15°C isotherm at about 202 km offshore) is associated with a cyclonic meander that is evident in the surface dynamic height field (Figure 32 (right)). A comparison between the spectral densities of the u component fluctuations for days 60 and 90 (Figures 33 and 35) shows that the dominant alongshore component wave number has changed with time towards lower values, resulting in an increase in the meridional scale of the eddies.

From day 90 to the end of the experiment (day 154), the two anticyclones continue to propagate westward at rates of approximately 2.2 and 3.1 km day, respec-
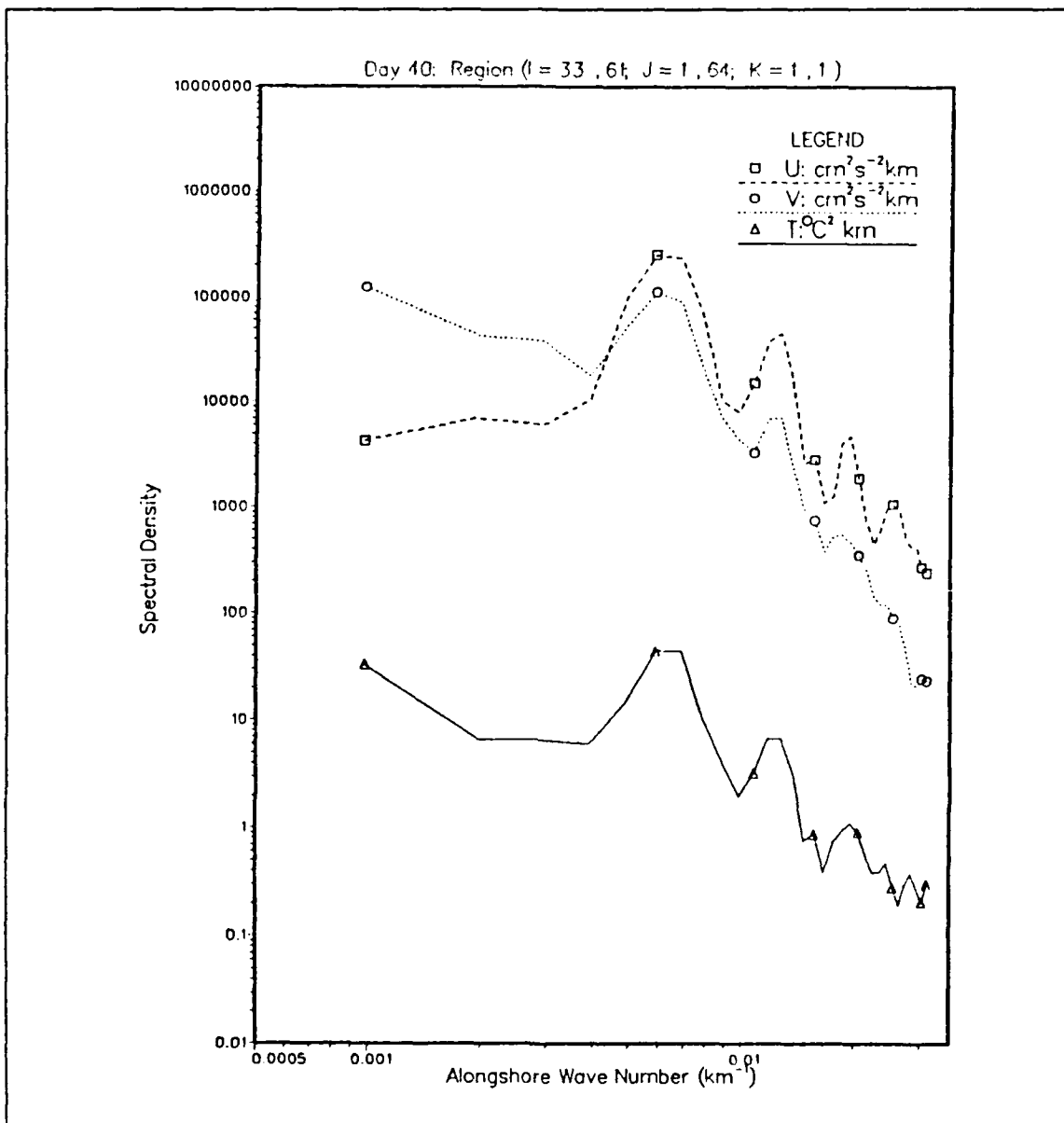
**Figure 31.** Spectral densities for the alongshore wave number of zonal (u) velocity, meridional (v) velocity, and temperature (T) for experiment 1 at day 40: The spectral density estimates were obtained from the spatial series of variables u,v, and T at grid points along $t^1$ meridional lines defined by indices ($i = 33,34,...,61$; $j = 1,2,...,64$; $k = 1$). Units of spectral densities are $cm^2 s^{-2} km$ for u and v, and $(°C)^2 km$ for T.
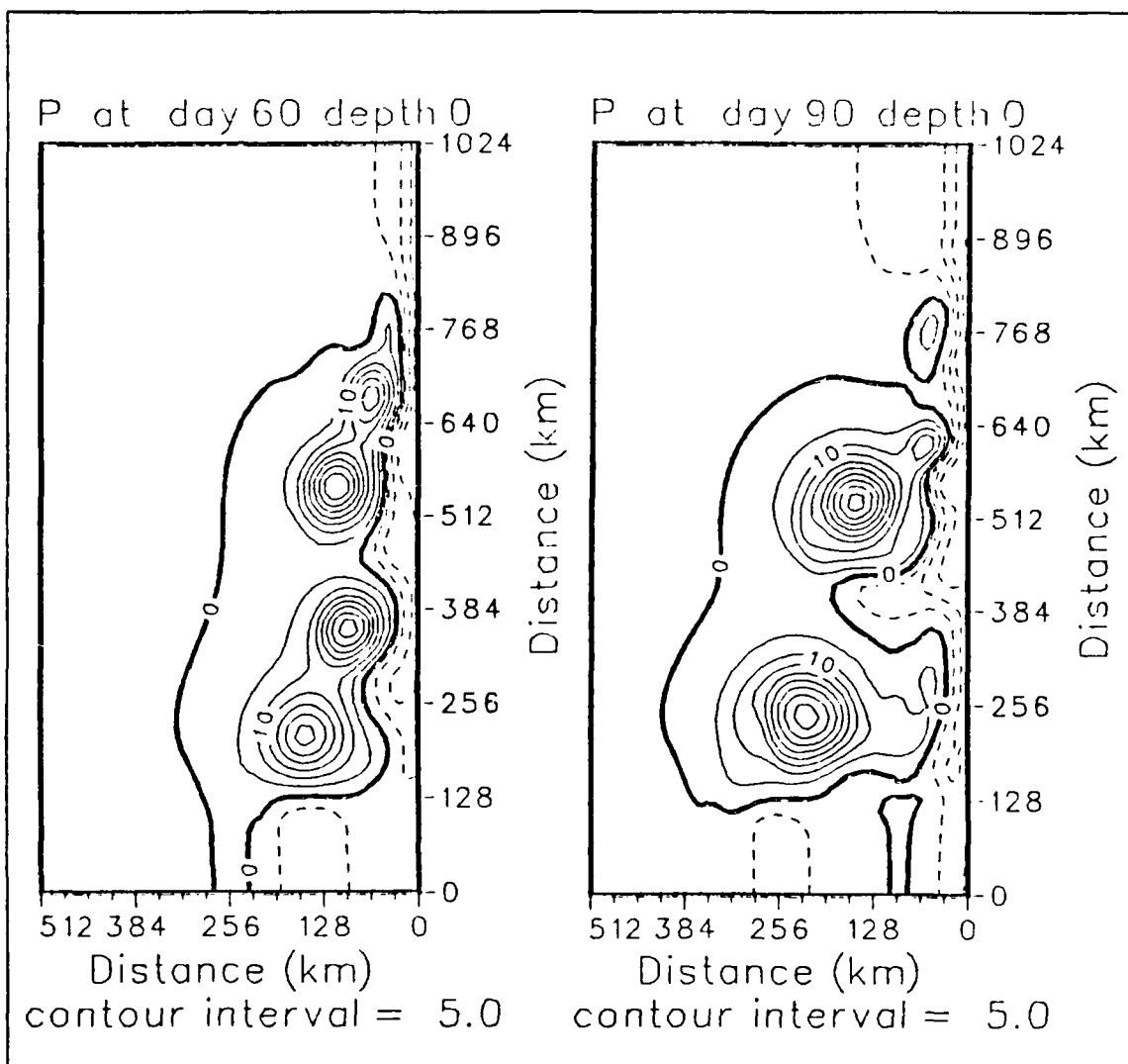
**Figure 32.** Surface isopleths of dynamic height (cm) relative to 2400 m for day 60 (left) and day 90 (right) for experiment 1: Contour interval is 5.0 cm. Dashed lines denote negative values.

tively, for the northern and southern eddies. This westward propagation of the eddies can be seen by comparing the surface dynamic height field in Figure 32 (right) with Figure 40. By day 150, the two large eddies have propagated farther offshore and two new anticyclones appear in the same region of negative wind stress curl as before, at approximately $y = 768$ and $y = 384$ km. The thermal structure (not shown) of these new warm core rings is consistent with the velocity field (via the thermal wind relation).
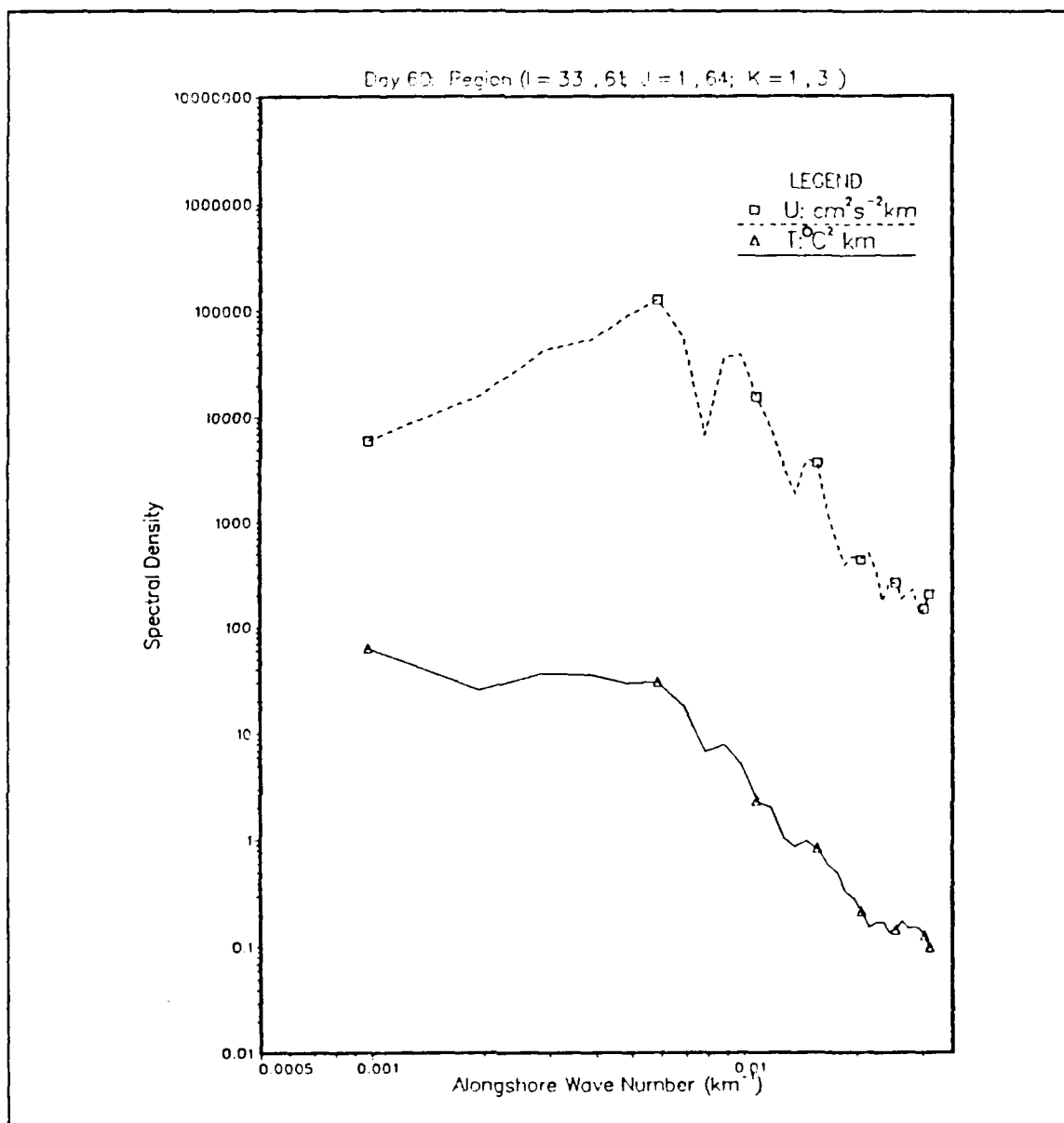
**Figure 33.** Spectral densities for the alongshore wave number of zonal (u) velocity and temperature (T) for experiment 1 at day 60: The spectral density estimates were obtained from the spatial series of variables u and T at grid points along the meridional lines defined by indices (i = 33,....,61; j = 1,2,....,64; k = 1,2,3). Units of spectral densities are $cm^2 s^{-2} km$ for u and $(°C)^2 km$ for T.
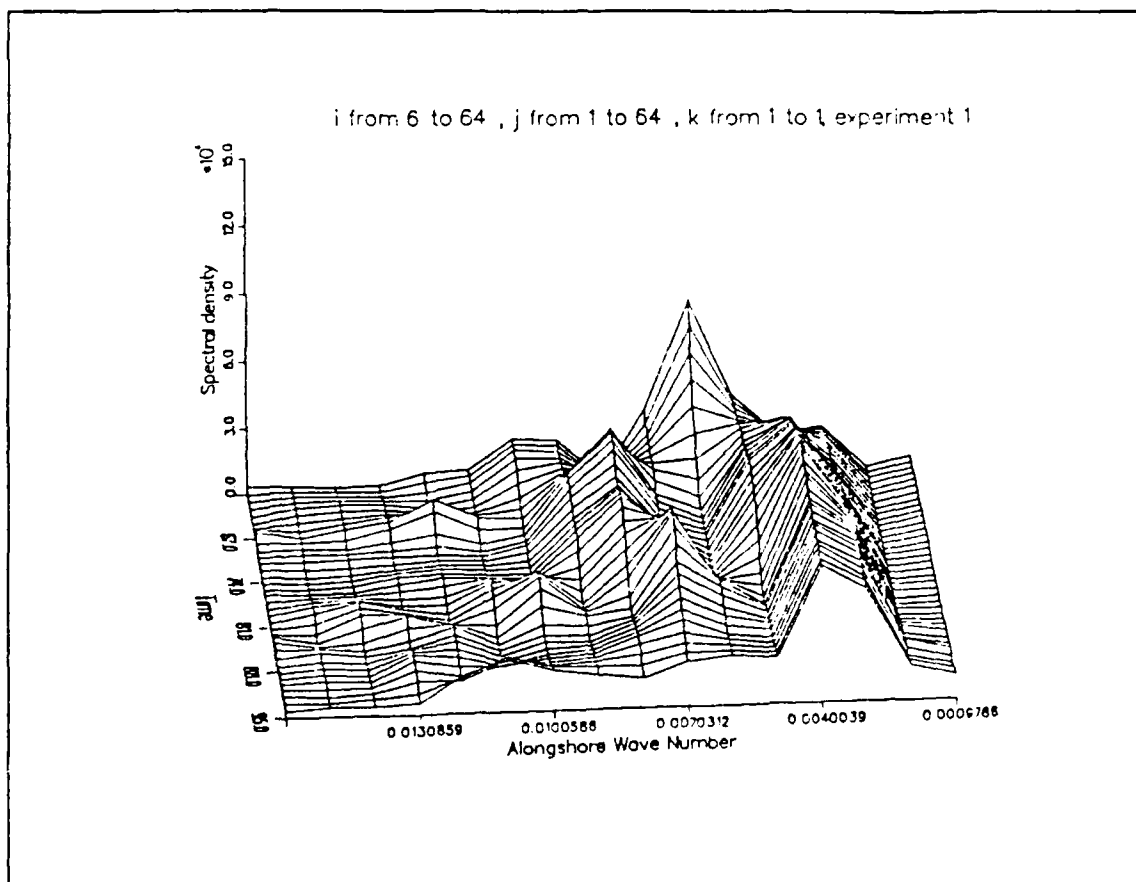
Figure 34.　Spectral density versus time of the alongshore wave number of zonal (u) velocity for experiment 1 from day 60 to day 95:　The spectral density estimates were obtained from the spatial series of (u) at grid points along meridional lines defined by indices (i = 6,7,...,64; j = 1,2,...,64; k = 1). Units are $cm^2 s^{-2} km$.

## B. TRANSIENT/TIME DEPENDENT WIND FORCING EXPERIMENTS

### 1. Experiment 2 (Poleward Wind Followed by Equatorward Wind)

#### a. Spring Transition

Forcing in this experiment consisted of a spatially uniform poleward wind stress of 1.2 $dynes/cm^2$ during the first 20 days followed by spatially uniform equatorward wind stress of 3.5 $dynes/cm^2$ to the end of the experiment (day 105). This wind forcing is used to qualitatively represent the transition between a pre-upwelling season and the upwelling season that may happen in March or April. The values of wind stress, rather

53
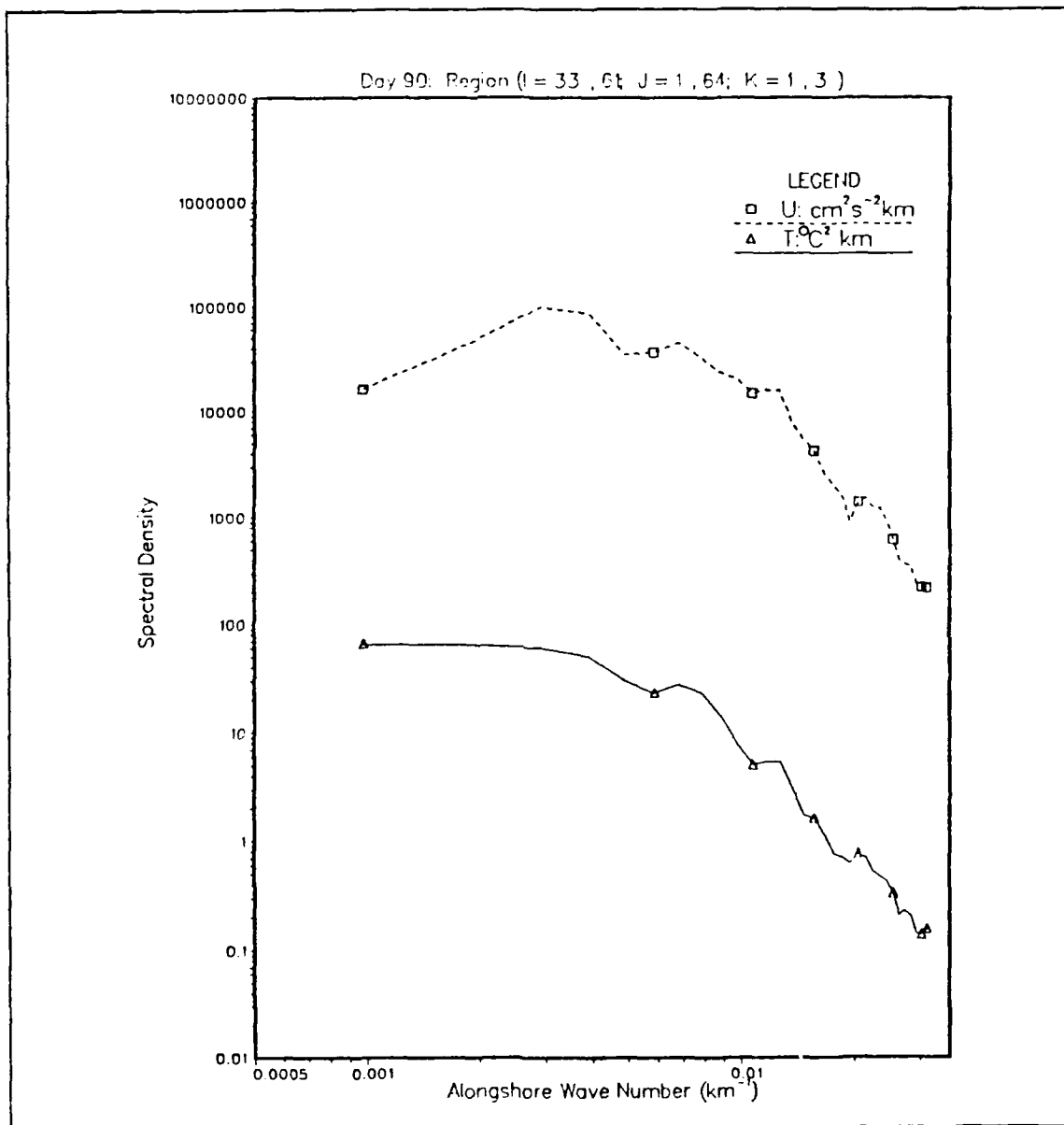
**Figure 35.** Spectral densities for the alongshore wave number of zonal (u) velocity and temperature (T) for experiment 1 at day 90: The spectral density estimates were obtained from the spatial series of variables of u and T at grid points along the meridional lines defined by indices (i = 33,...,61; j = 1,2,...,64; k = 1,2,3). Units of spectral densities are $cm^2 s^{-2} km$ for u and $(°C)^2 km$ for T.
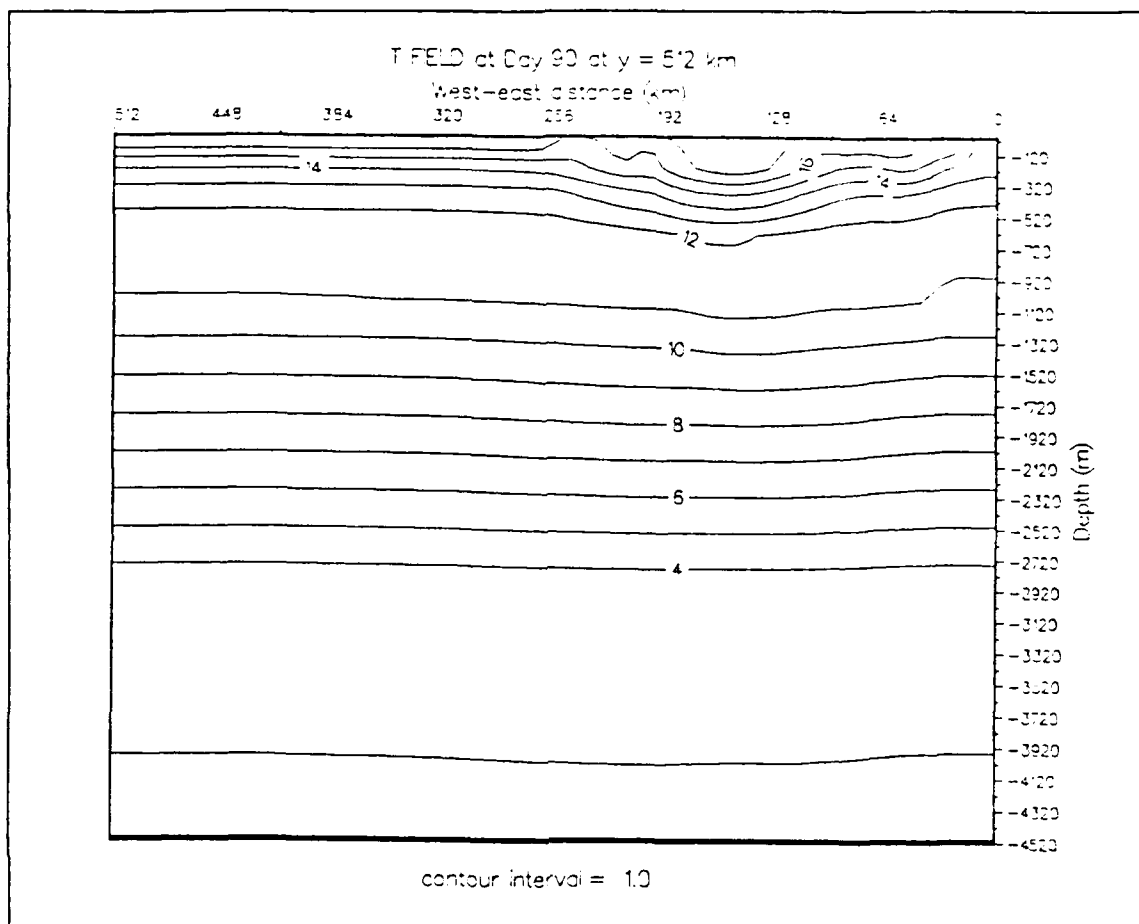
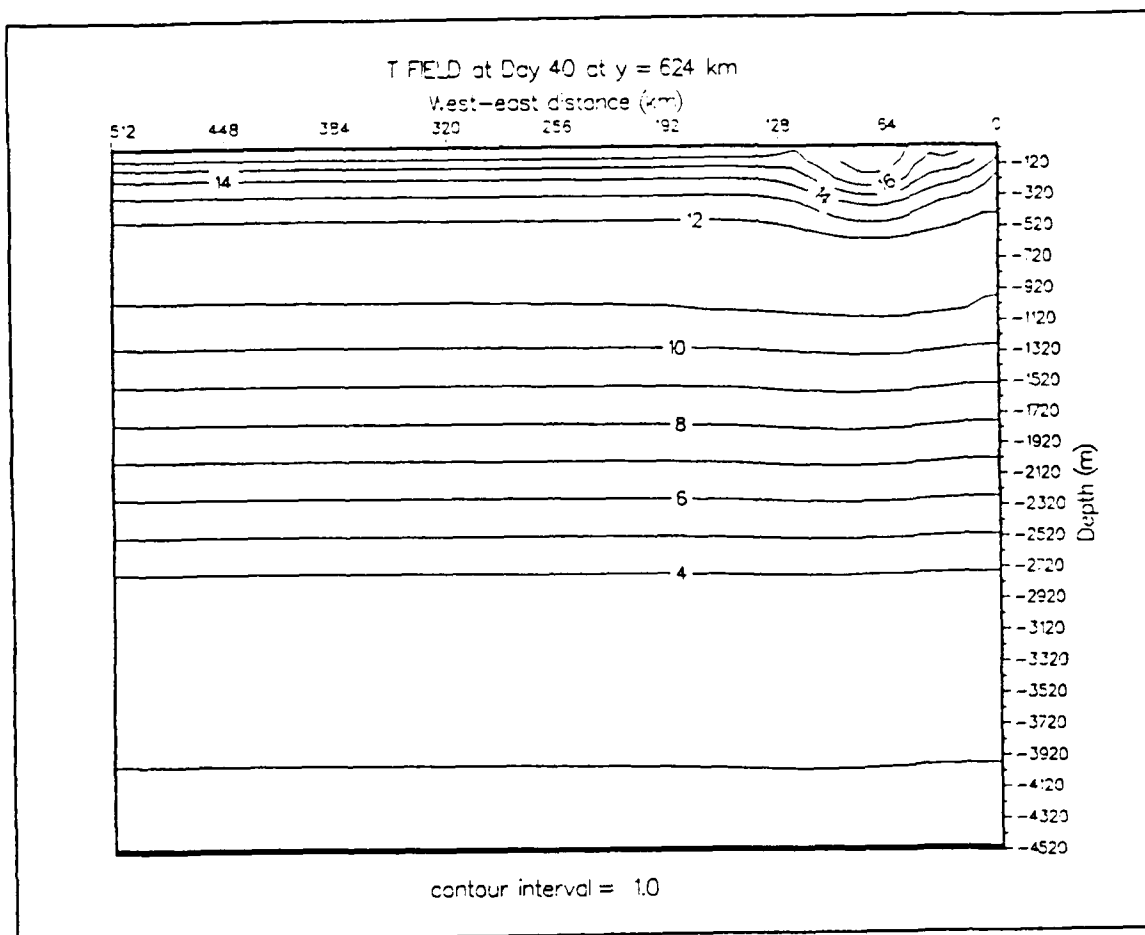**Figure 36.** Vertical cross-shore section of temperature (°C) at y = 512 km for experiment 1 at day 90:   Contour interval is 1.0°C.

larger than the mean climatological values for the region, correspond to peak values of strong wind events in the region for pre-upwelling and upwelling seasons.

Under the forcing of the poleward winds. as expected, the surface flow responds with onshore Ekman transport (Figure 41 (left)), convergence in the surface layer and downwelling. as seen by the tilting of the 17, 16, and 15°C isotherms in the upper 200 m, within approximately 20 km of the coast (Figure 42). On day 20 the surface dynamic heights relative to 2400 m show increasing values towards the coast (not shown) and a coastal surface poleward jet consistently shows up within about 40 km from the coast. with increasing velocities from south to north ( Figure 41(right)). The alongshore averaged meridional (v) velocities ( Figure 43) show that the vertical extent of the surface poleward jet is about 150 m. that the core is  ¸ the surface at about 8 km
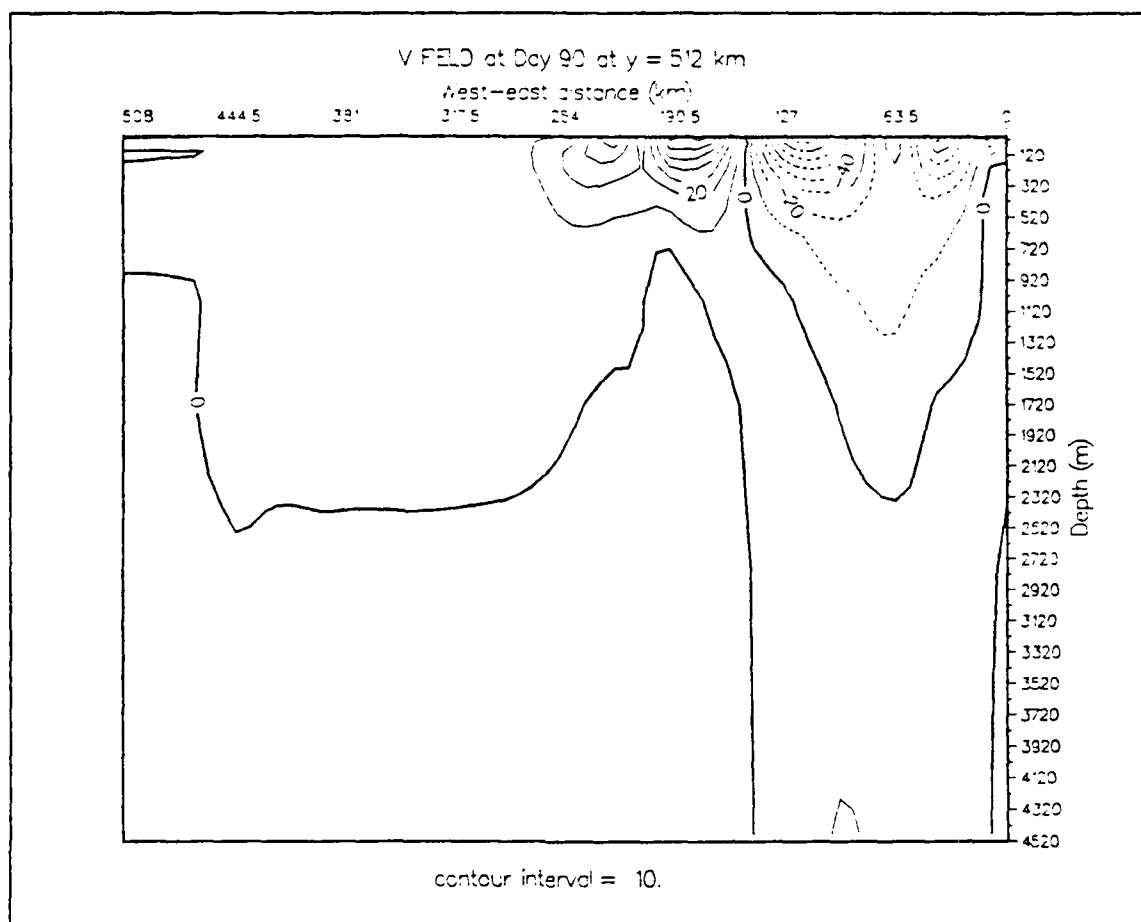
**Figure 37.** Vertical cross shore section of meridional (v) velocity (cm/s) at y = 512 km for experiment 1 at day 90: Contour interval is 10.0 cm s.

offshore, and that there is a weak equatorward undercurrent with an alongshore aver-aged velocity of around 2 cm s at depths between roughly 200 and 520 m, corresponding to the portion of the section where the 14, 13, and 12°C isotherms slope slightly upward towards the coast (Figure 42). While the equatorward undercurrent is not commonly observed near the coasts of eastern boundary regions, with the exception of the Leeuwin current (Thompson, 1984) the surface poleward current under poleward winds is con-sistent with observations on the shelves. For instance, according to Huyer (1983), over the shelf off Oregon during the winter (prevailing poleward winds), there is no mean southward surface flow and no mean vertical shear. The simulated poleward current in the upper 150 m partially corresponds to those observations. However, the vertical shear of the poleward current in the model does not correspond as well to Huyer's (1983) ob-
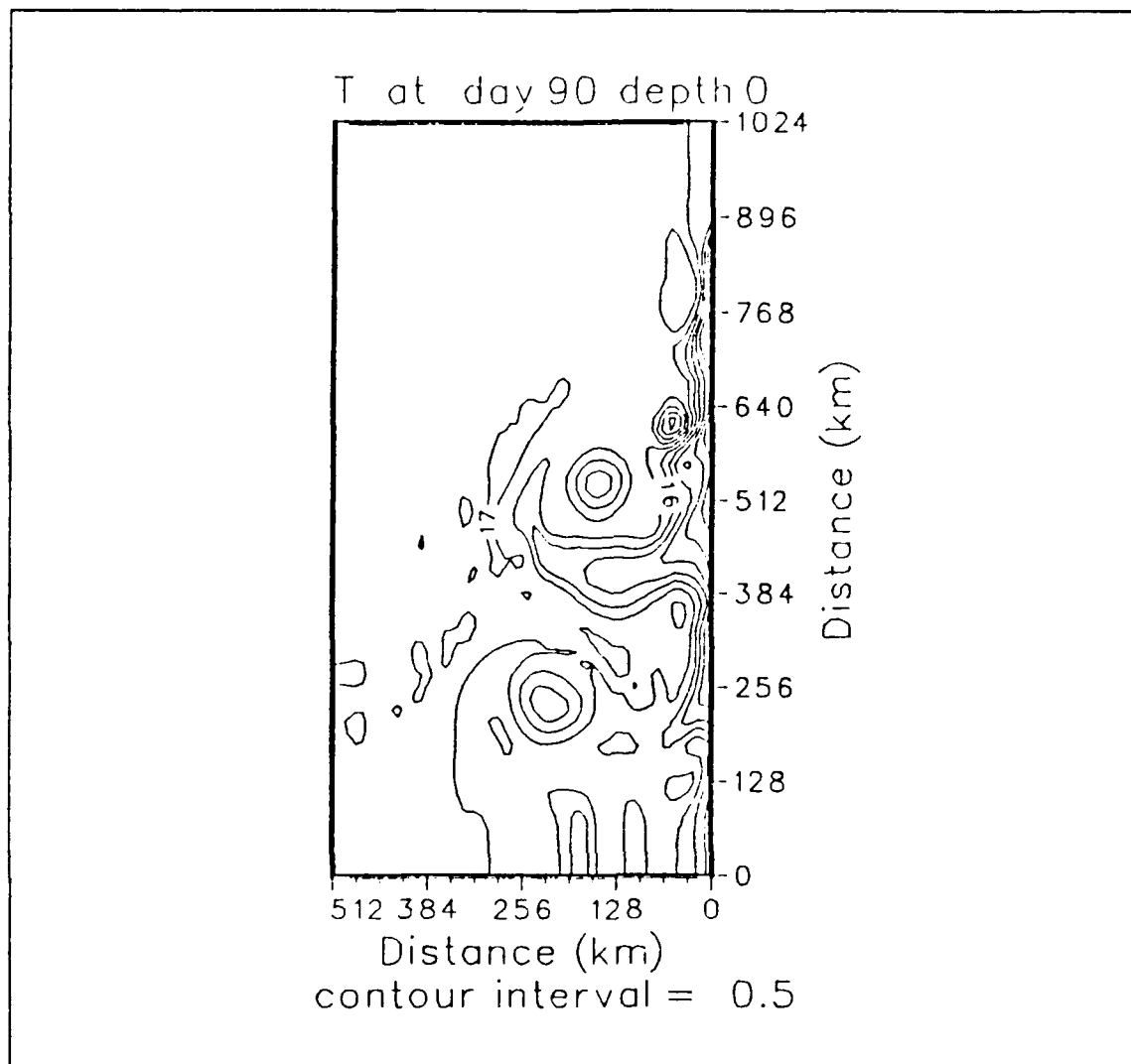
**Figure 38.** Surface isotherms (°C) for experiment 1 at day 90: Contour interval is 0.5°C.

servations. This difference may be caused by the exaggerated downwelling of the isotherms in the model for the coastal region, leading to large horizontal density gradients in the offshore direction and associated vertical shear in the meridional (v) velocities. The core of the poleward jet is placed approximately 8 km offshore in the position where the 17°C isotherm slopes downward from the surface. On actual continental shelves, the location of the core of the poleward jet may be modified by seasonal river
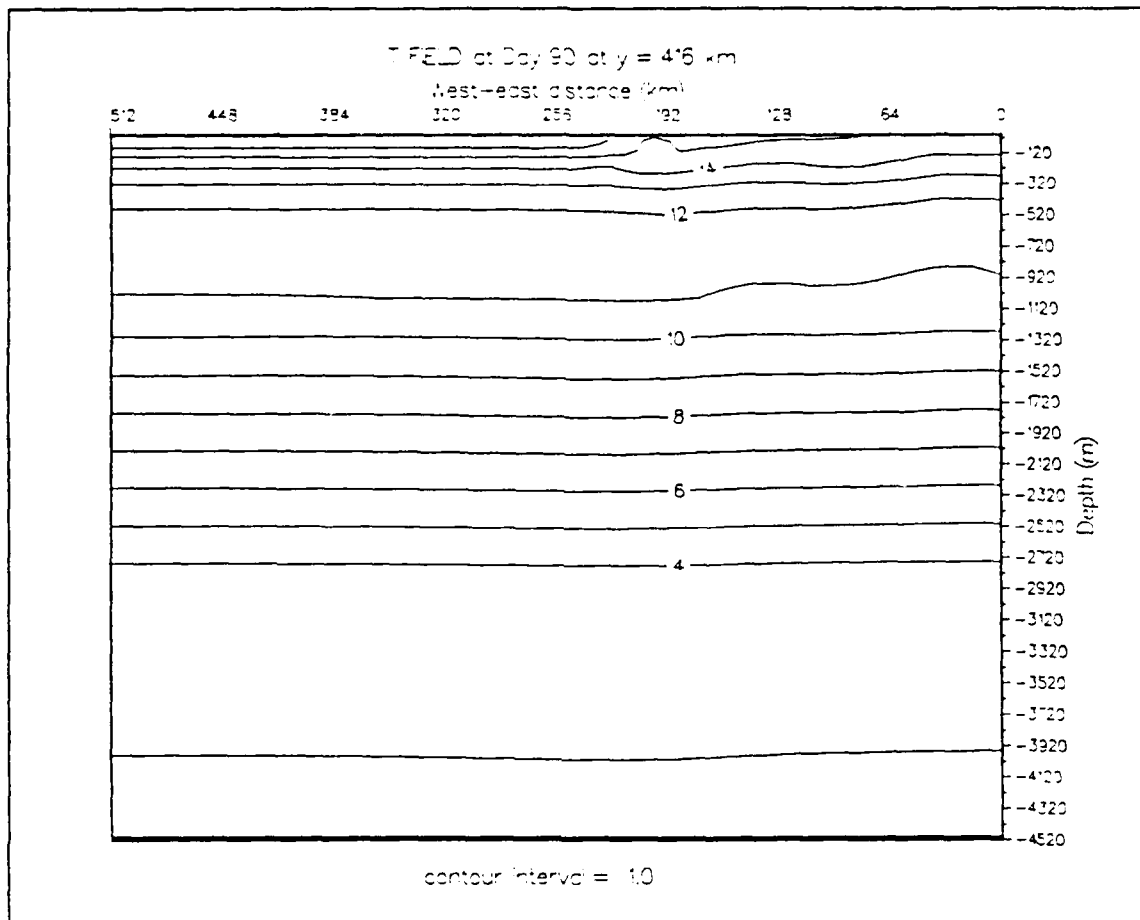
**Figure 39.** Vertical cross-shore section of temperature (°C) at y = 416 km for experiment 1 at day 90: Contour interval is 1.0°C.

discharges that introduce changes in the horizontal stratification of the near coastal waters, but such effects are not addressed in this study.

After the transition to equatorward winds on day 22, a vertical zonal section of temperature in the middle of the domain (Figure 44) shows that the previous downwelled isotherms now tilt upward, particularly near the coast. However, the 15 and 16°C isotherms, at distances from the coast between 26 and 10 km, still show the downward tilting which remains from the previous forcing by poleward winds. By day 22, the poleward surface jet evident on day 20 is not apparent and has been replaced by a relatively deep (vertical extent of about 350 m at the coast), equatorward coastal current (Figure 45). The horizontal maps of zonal (u) velocity at depths of 20 and 70 m (Figure 46) show that the surface Ekman layer may get as deep as about 70 m in the
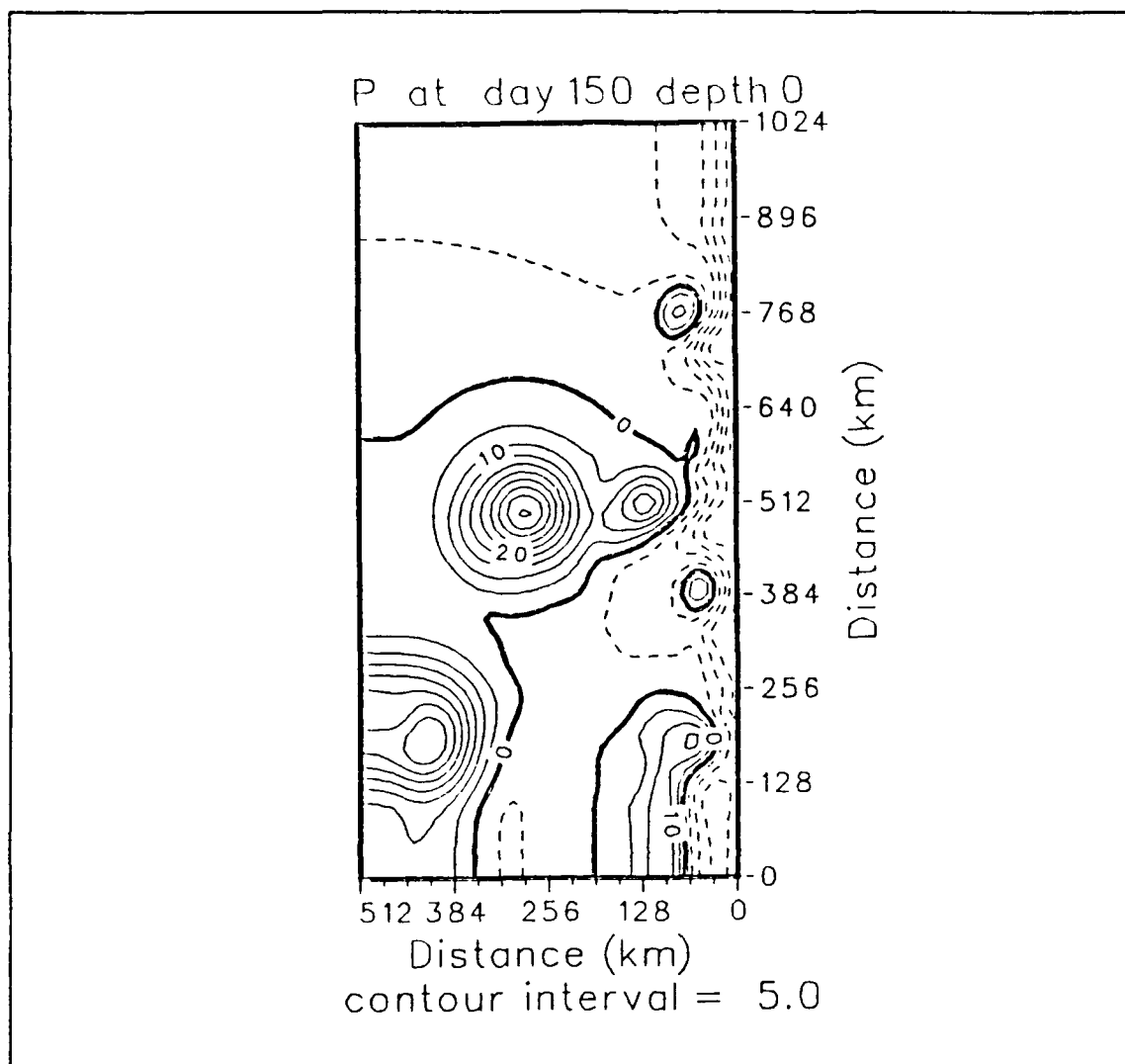
**Figure 40.** Surface contours of dynamic height (cm) relative to 2400 m for experiment 1 at day 150: Contour interval is 5.0 cm. Dashed contours denote negative values.

model. At 20 m, relatively large values of offshore zonal (u) velocity (Figure 46 (left)) are consistent with a typical Ekman layer response to equatorward winds. Below the Ekman layer (depths of typically 20-30 m), observations on the shelves in eastern boundary regions have shown onshore transport in the so called "geostrophic interior regime". The model seems to reproduce a relatively deep Ekman layer, because as demonstrated in Figure 46 (right), the transition between the two regimes may happen at
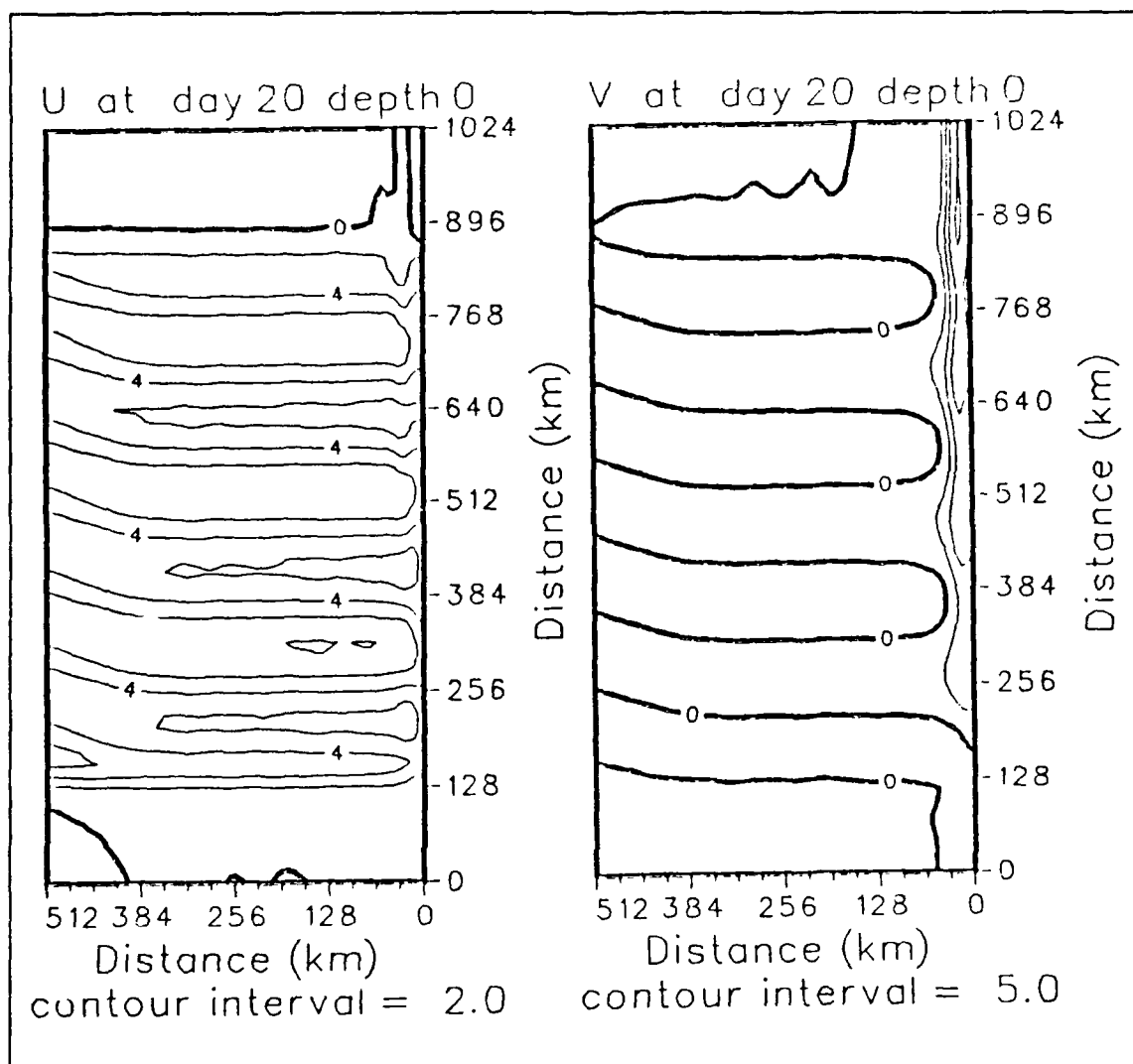
**Figure 41.** Surface isopleths of (left) zonal (u) velocity (cm/s) and (right) meridional (v) velocity (cm/s) for experiment 2 at day 20:   Contour interval is 2.0 cm s for (u) and 5.0 cm s for (v). Dashed lines denote offshore and equatorward velocities.

about 70 m depth. Comparing the results described for days 20 and 22 of this experiment, one may conclude that the model coastal isotherms and velocities respond relatively quickly (one or two days) to a sudden change from moderate poleward winds to strong equatorward winds.

**Figure 42.** Vertical cross-shore section of temperature (°C) at y = 512 km for experiment 2 at day 20:   Contour interval is 1.0°C.

On day 30, after 10 days of equatorward winds, the 16 and 15°C upwelled isotherms have surfaced at distances of about 30 and 13.5 km from the coast, respectively (Figure 47). The surface equatorward jet, with its core located approximately in the position where the 15°C isotherm has surfaced, shows a large vertical shear in the alongshore (v) velocity (Figure 48) that is associated with the frontal-like structure in the upper 70 m of the nearshore water column. In this region, temperature increases in the offshore direction by 2.0°C in 30 km (Figure 47). A poleward undercurrent, with an averaged meridional (v) velocity greater than 5 cm s, also exists nearshore between 320 and 450 m (Figure 48), where the 12°C isotherm bends down towards the coast (Figure 47). By day 30, the system consists of an equatorward surface jet, located within 40 km of the coast, and a poleward undercurrent at depths greater than 186 m, right at

**Figure 43.** Vertical cross-shore section of alongshore-averaged meridional (v) velocity (cm/s) for experiment 2 at day 20: Contour interval is 2.0 cm s.

the coast. At this point we may establish a parallel with observations over the shelf off Oregon that document a "spring transition" under a single upwelling event that began on 25 March and continued intermittently through 31 March, 1975. According to Huyer (1983), this particular upwelling event *"caused the transition from the typical winter regime with level isopycnals and no mean vertical shear to the typical spring summer regime with sloping isopycnals, a mean southward surface current and a strong mean vertical shear"*. We note from our experiment the following differences relative to the typical winter situation off Oregon :

- Before the turning to equatorward winds, the isotherms isopycnals were sloping downward near the coast as opposed to being level.

62

**Figure 44.** Vertical cross-shore section of temperature (°C) at y = 512 km for experiment 2 at day 22: Contour interval is 1.0°C.

- Before the turning to equatorward winds, there was a vertical shear in the poleward current nearshore, associated with downwelling, as opposed to no mean vertical shear.

Nevertheless, starting from slightly different conditions, after 10 days cf 14.2 m s, equatorward winds (in the observations off Oregon, the southward upwelling favorable winds were intermittent with a peak velocity of about 12.7 m s), the model thermal and velocity fields show a change that is consistent with the spring transition observations off Oregon; by day 30, there are upward sloping isotherms/isopycnals, a mean southward surface current, and a strong mean vertical shear. For the study region off the coast of Portugal, there is a lack of observational studies to document the seasonal transition

**Figure 45.** Vertical cross-shore section of alongshore-averaged meridional (v) velocity (cm/s) for experiment 2 at day 22: Contour interval is 5.0 cm s. Dashed lines denote equatorward velocities.

that may occur in March or April and thus we are not sure if a single strong wind event will mark the beginning of the upwelling season.

With time, under the forcing of the steady equatorward winds (compare Figures 47 and 48 with Figures 49 and 50, for days 30 and 50) we note the following changes:

- The surfaced isotherms are displaced farther offshore and the core of the equatorward jet is also displaced offshore, apparently tracking the 14.5°C isotherm.

- The jet widens as far as 64 km from the coast and its maximum alongshore meridional (v) velocity weakens from ~ 35 cm s on day 30 to ~ 28 cm s on day 50.
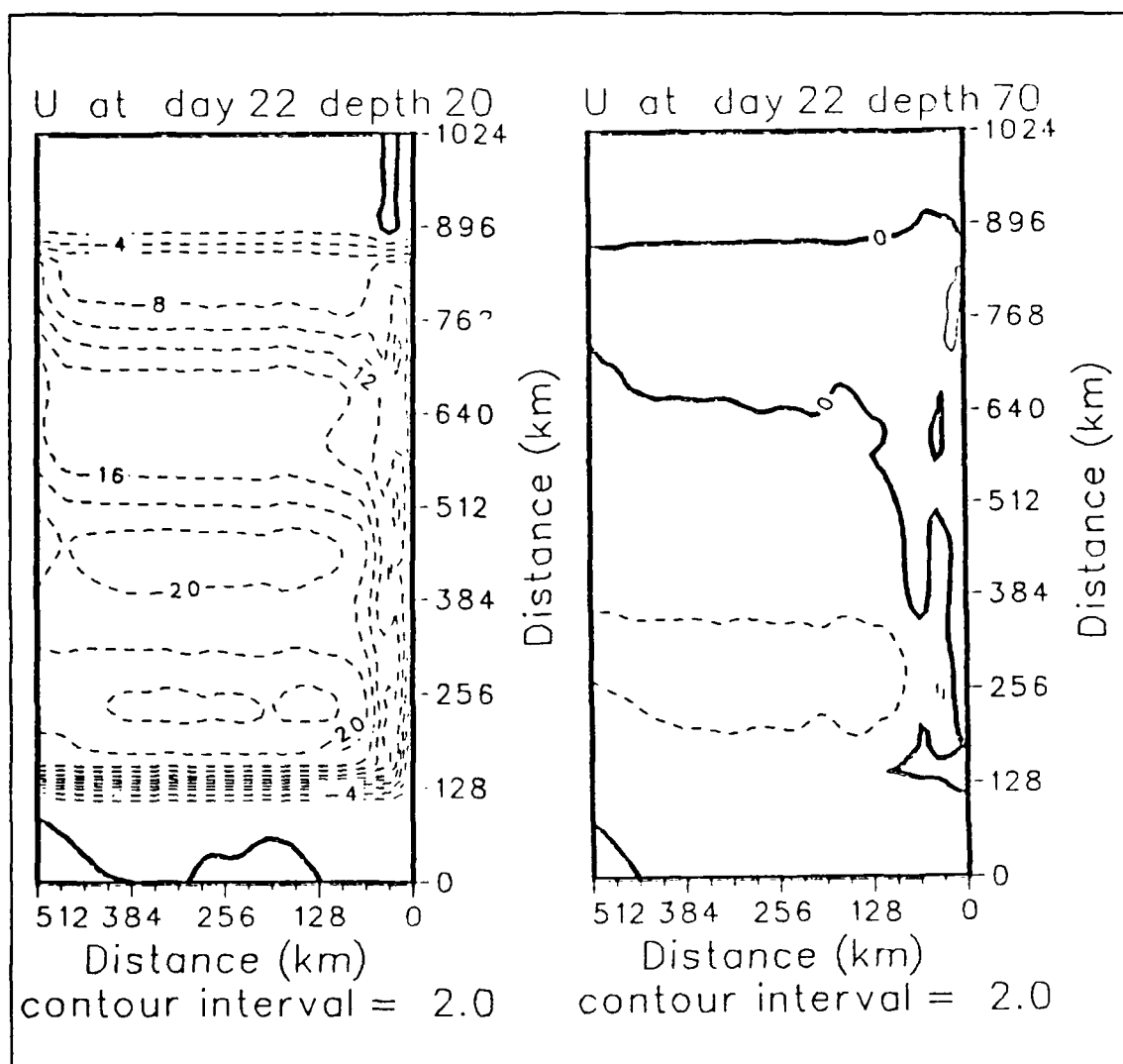
**Figure 46.** Isopleths of zonal (u) velocity (cm/s) at 20 m depth (left) and 70 m depth (right) for experiment 2 at day 22: Contour interval is 2.0 cm s. Dashed lines denote offshore velocities.

- The depth where the southward current changes to a poleward current is seen to shoal somewhat within approximately 20 km of the coast. For instance, on day 30, poleward flow existed at depths greater than about 185 m, while on day 50, the poleward flow was below about 120 m.

- A relatively weak surface poleward countercurrent exists offshore of the equatorward surface jet on day 50.

At this point, the results of the model suggest that as one progresses through the up-welling season, the surface layer front and the core of the equatorward surface jet may
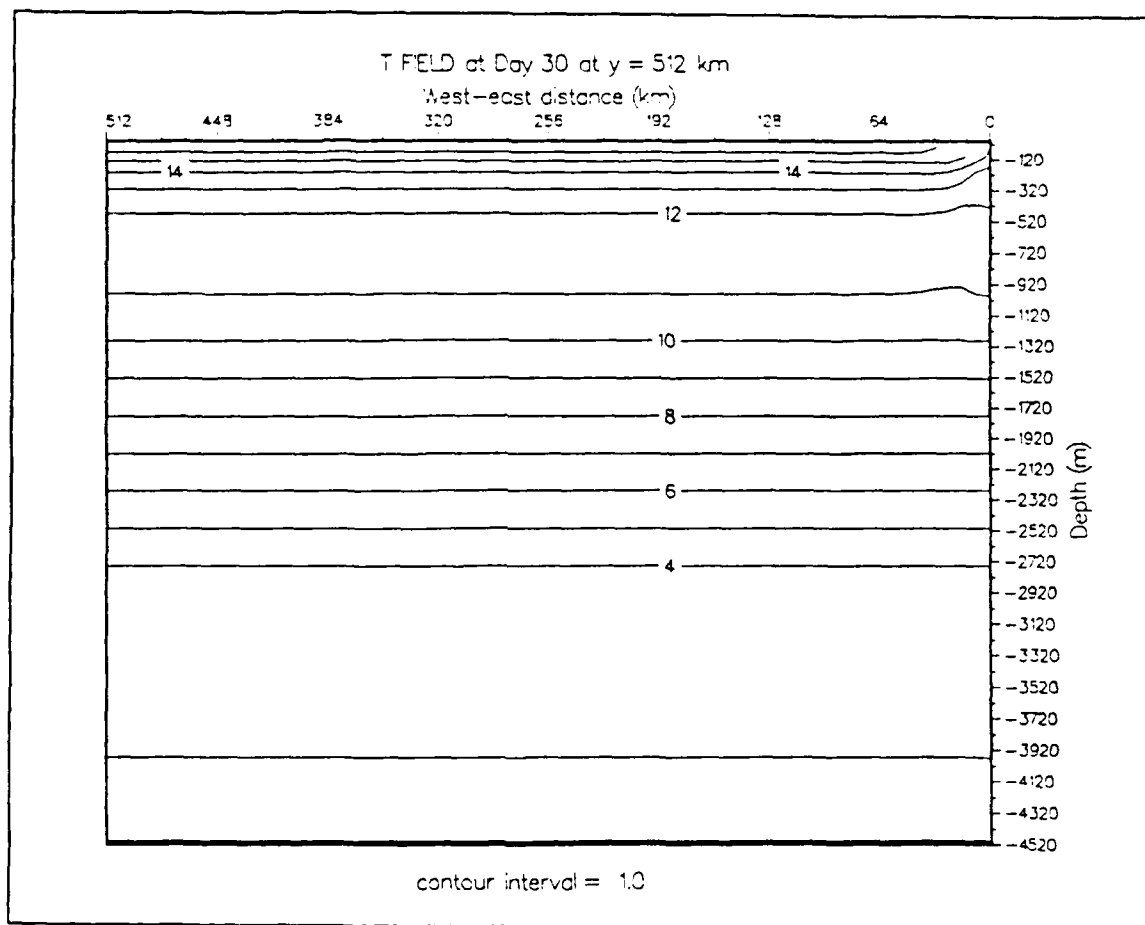
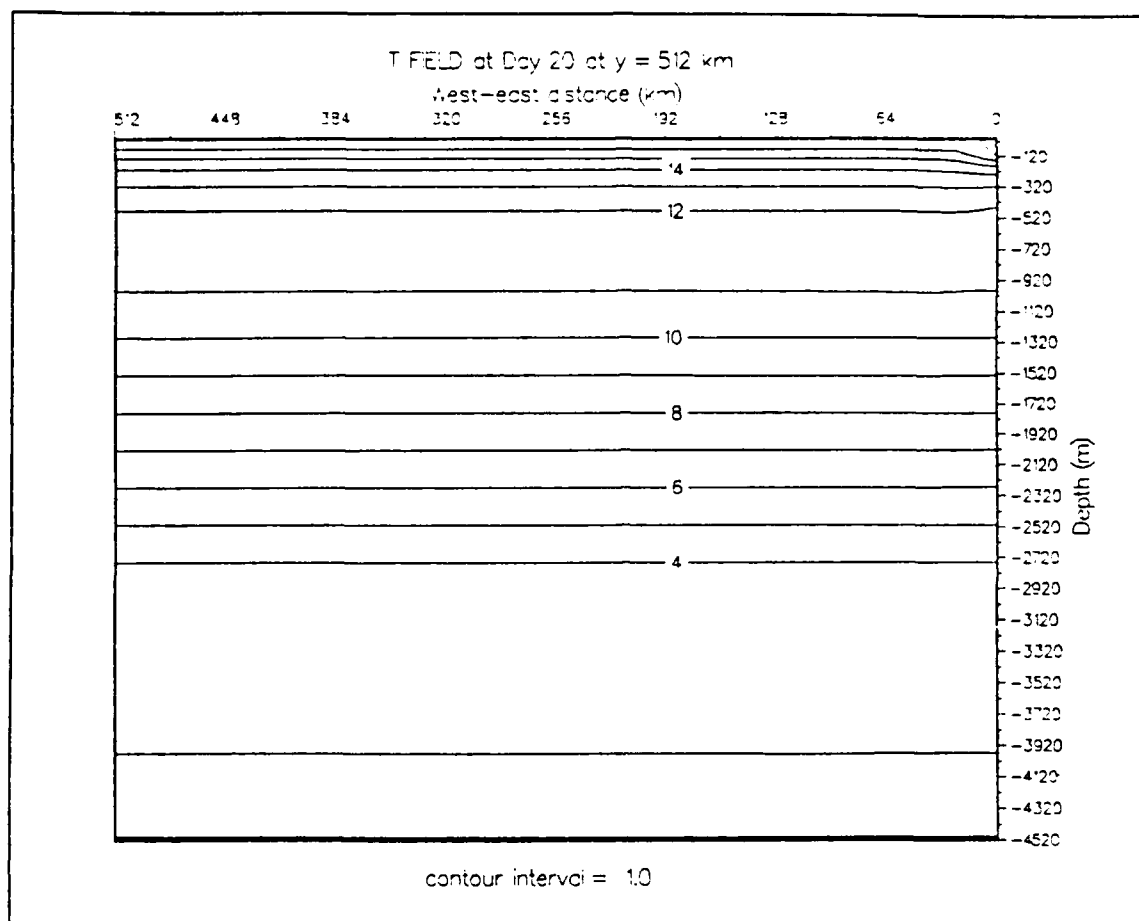**Figure 47.** Vertical cross-shore section of temperature (°C) at y = 512 km for experiment 2 at day 30: Contour interval is 1.0°C.

typically be displaced offshore (as compared to earlier in the season) and that a compensating poleward undercurrent may reach depths that would correspond to the lower portion of a continental shelf. According to Huyer (1983), *"the dominant features are a southward coastal jet at the surface and a poleward undercurrent along the bottom* [and] *the southward coastal jet has its maximum (about 25 cm/s) at 15-20 km from shore* [and] *the poleward undercurrent has a velocity of about 5 cm/s"*. Current meter observations taken off the coast of Portugal at latitude 38°06'N, from 12 June to 7 July of 1980, during the peak of the upwelling season, had mean meridional (v) velocities of -1.69 cm s at 15 m depth, 4.6 km offshore (bottom depth of 50 m) and -2.08 cm s at a depth of 17 m, 21 km offshore (near the shelf break and bottom depth of 150 m; Fiuza, 1984). Thus the model results on day 50 (after 30 days of equatorward winds) seem consistent ob-
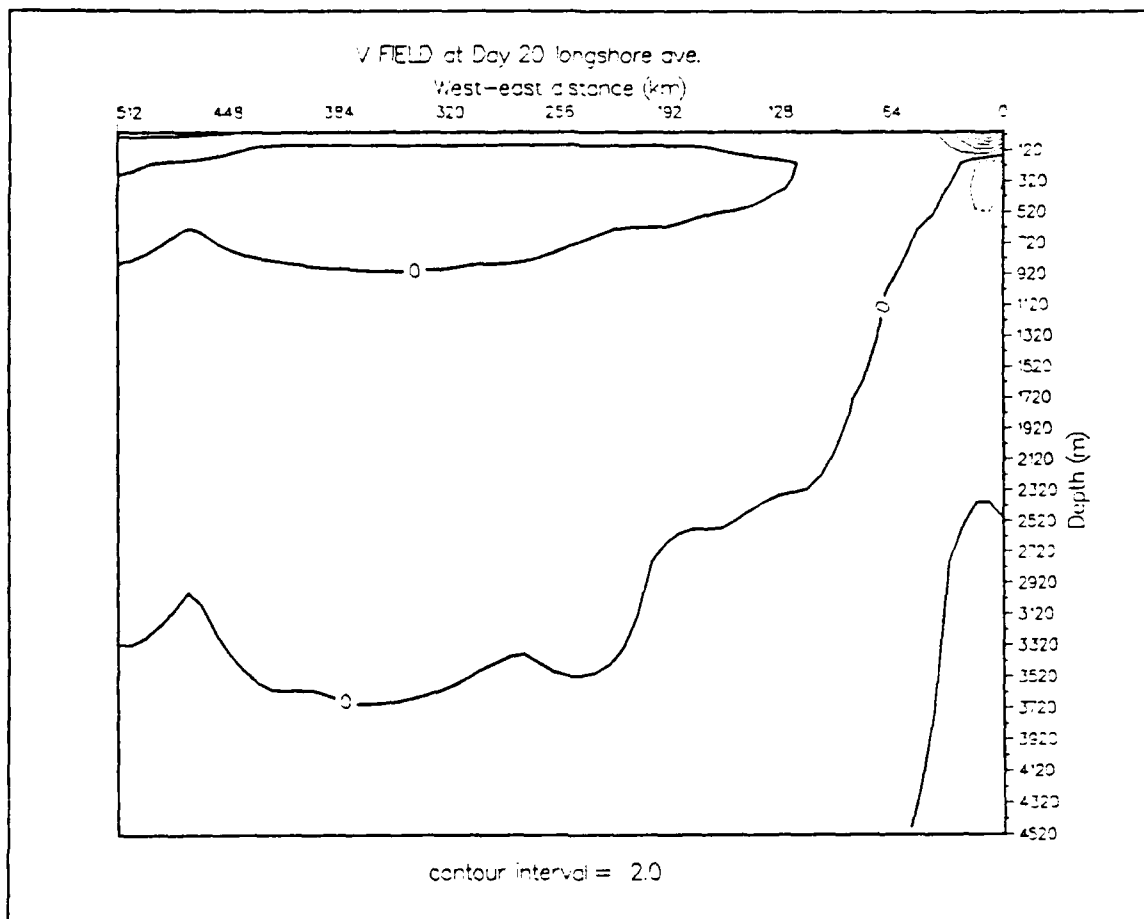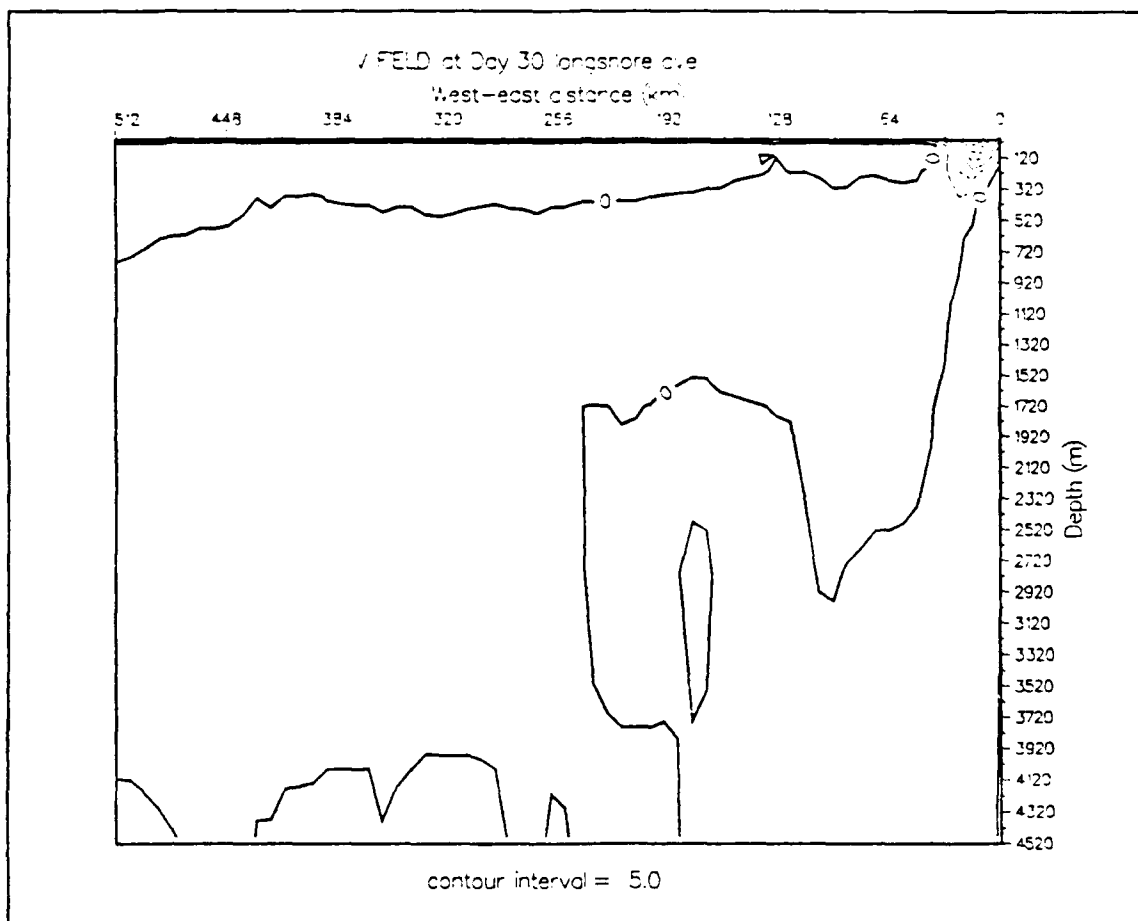
**Figure 48.** Vertical cross-shore section of alongshore-averaged meridional (v) velocity (cm/s) for experiment 2 at day 30: Contour interval is 5.0 cm, s. Dashed lines denote equatorward velocities.

servations off Oregon, by showing the equatorward surface jet with the core at a distance of about 27 km, a maximum velocity of about 28 cm s, strong vertical shear, and weak poleward flow at depths that correspond to the near bottom portion of the water column on the shelf. The model results, however, do not seem to be as consistent with the observations off Portugal, which have rather smaller mean meridional (v) velocities.

### b. Development of Eddies

On day 50 the dynamic heights of the surface (relative to 2400 m) show a high pressure center (positive values over 2 cm) at approximately y = 640 km, 60 km offshore (Figure 51 (left)). The high pressure region has a meridional extent that, with time gets larger zonally and propagates offshore and to the south (compare Figure 51
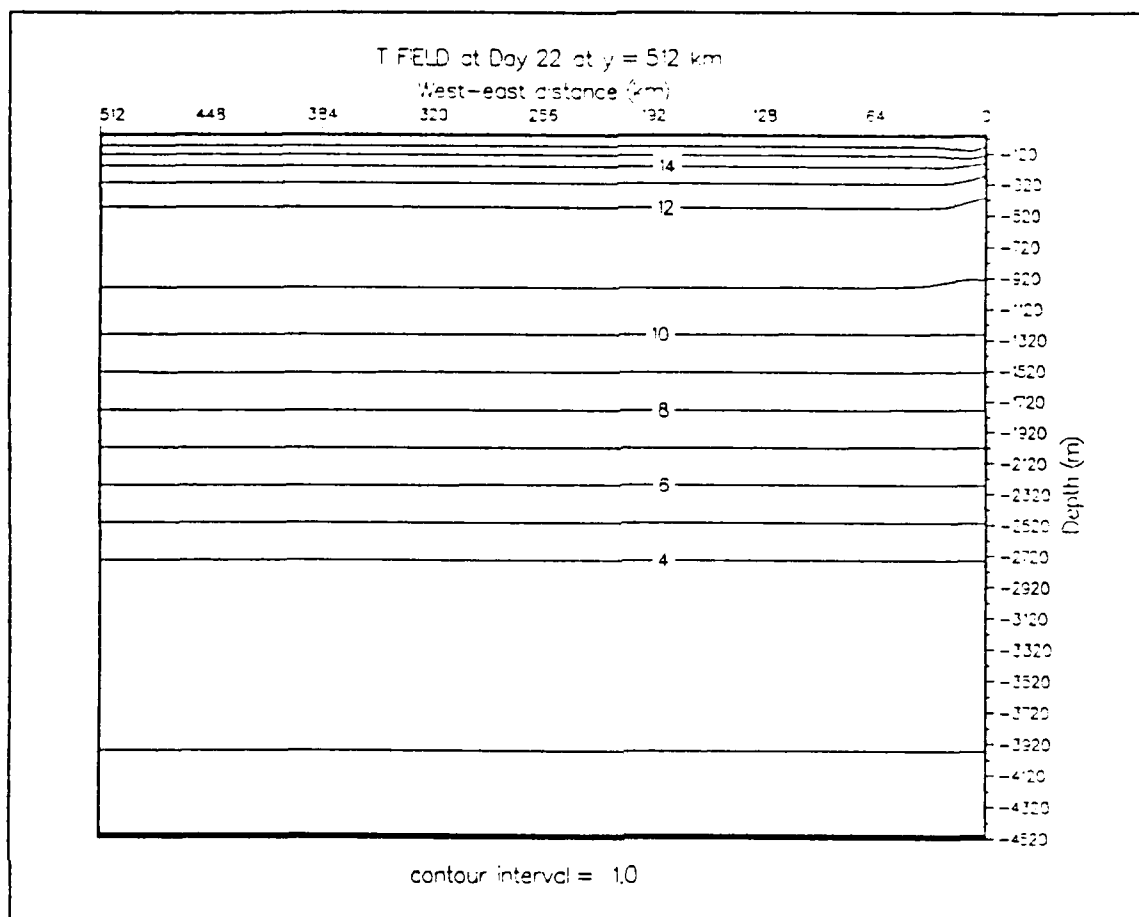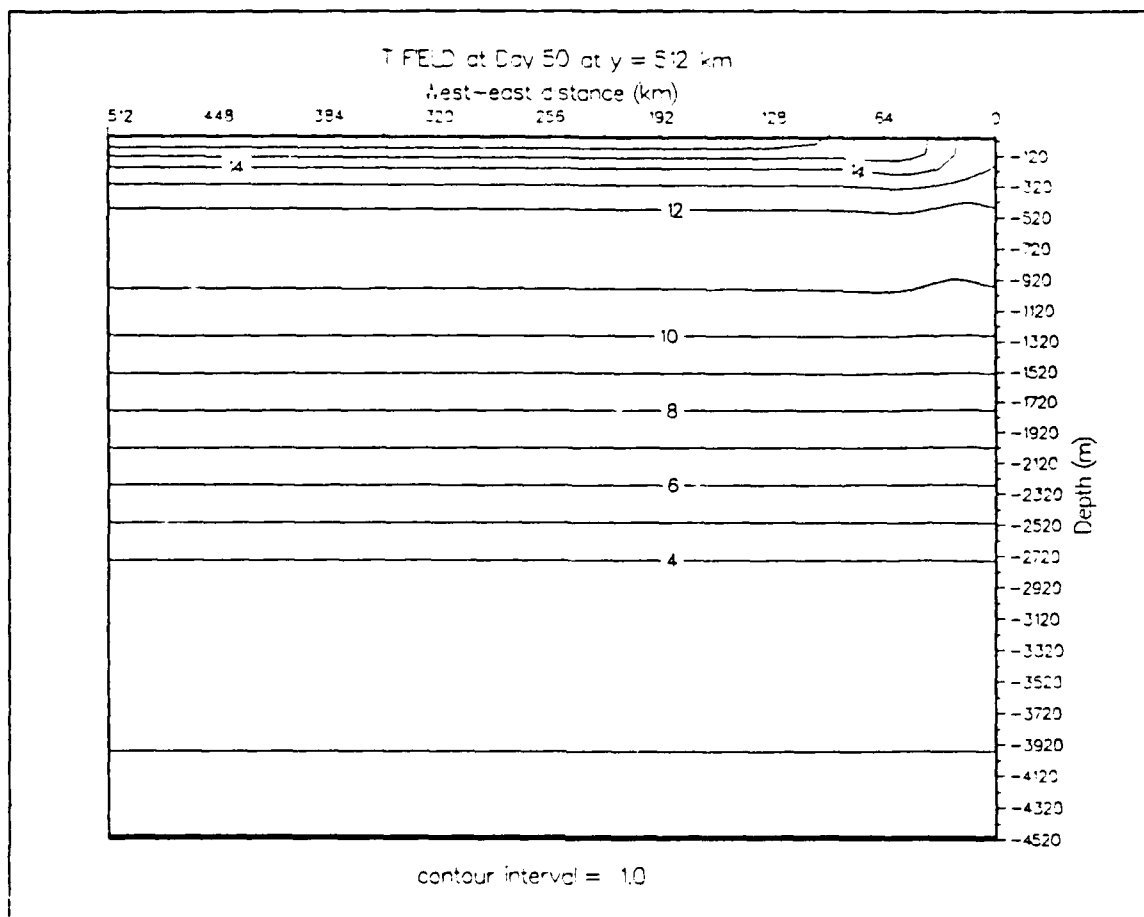
**Figure 49.** Vertical cross-shore section at day 50 of temperature (°C) at y = 512 km
for experiment 2 at day 50: Contour interval is 1.0°C.

(left) and (right)). Such propagation may be explained by the continuous offshore mo-
tion in the upper layer, due to the uniform equatorward wind stress, and also due to the
strong southward mean flow, especially on the eastern side of the ridge. Comparing the
flow field of this experiment (day 50, after 30 days of equatorward wind) with experiment
1 (day 20), the surface high pressure ridge developed at about the same alongshore po-
sition, but in this case of uniform winds took a much longer time to generate eddies. The
absence of negative wind stress curl explains that the poleward surface countercurrent
offshore of the pressure ridge is much weaker and extends much less in the alongshore
direction. In experiment 1, the negative wind stress curl caused a much larger conver-
gence and downwelling of isotherms on the west side of the pressure ridge, leading to
much stronger poleward surface circulation offshore of the ridge, a much larger hori-
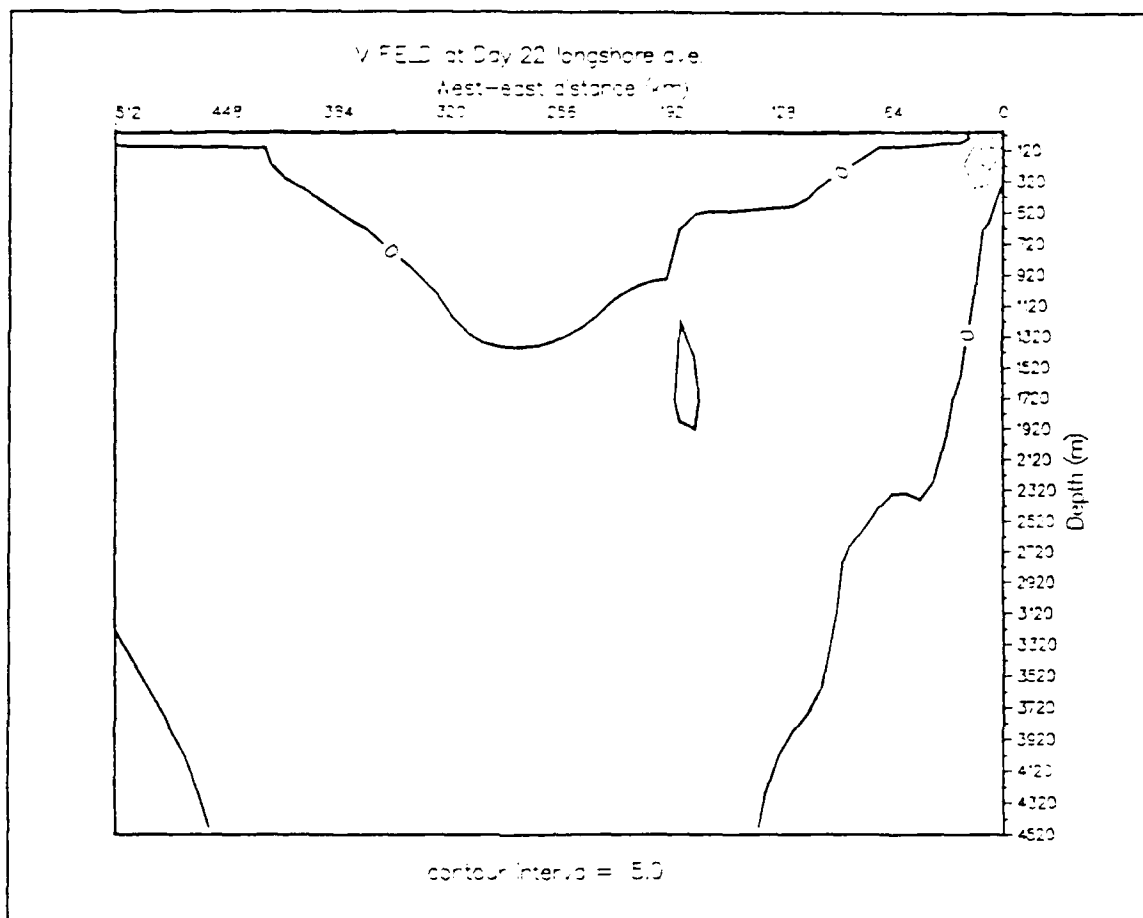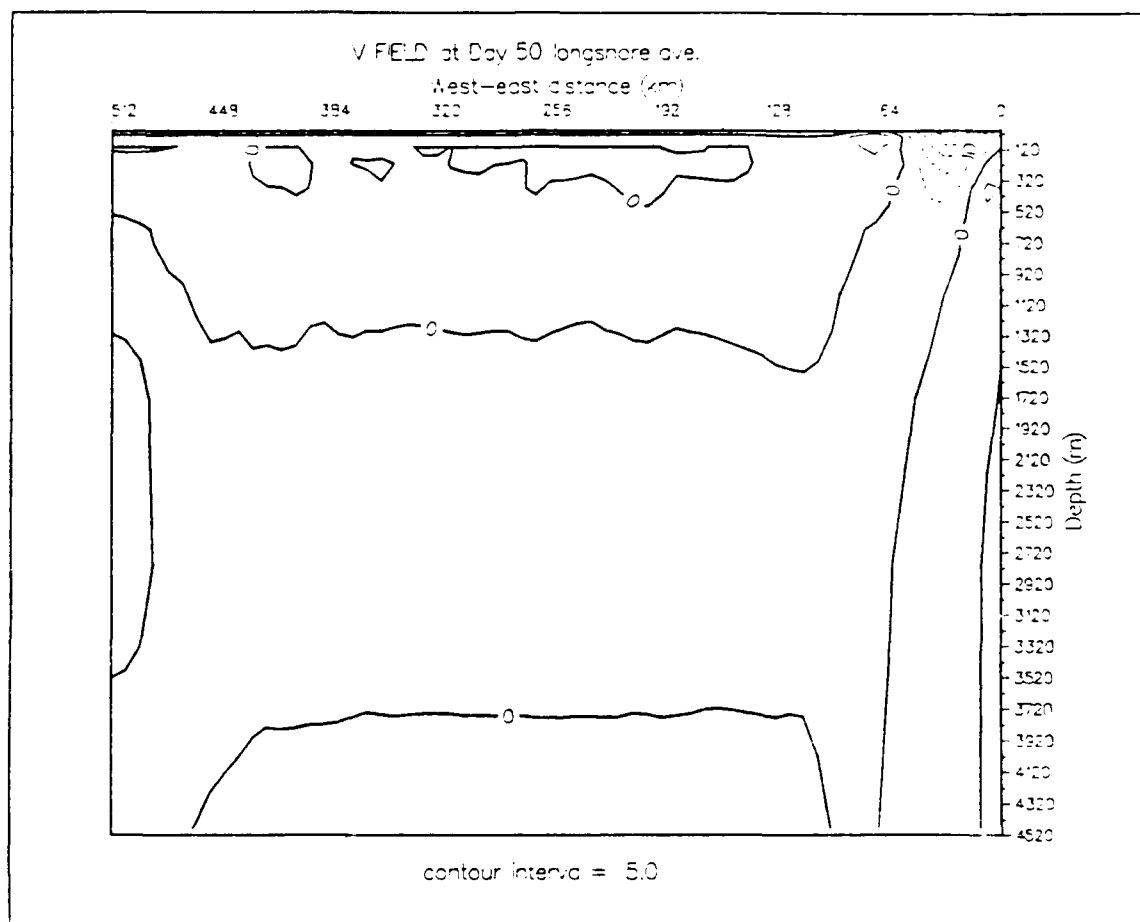
**Figure 50.** Vertical cross-shore section of alongshore-averaged meridional (v) velocity (cm/s) for experiment 2 at day 50: Contour interval is 5.0 cm s. Dashed lines denote equatorward velocities.

zontal shear between the equatorward and poleward surface currents, and an earlier development of eddies due to a predominantly barotropic instability of the mean flow.

By day 75 (after 55 days of equatorward 3.5 *dynes/cm²* wind stress) the surface dynamic height field shows two anticyclonic circulations that develop in the region of the high pressure at positions of approximately y = 593 km and y = 473 km, and one cyclonic circulation that develops within 50 km of the coast at y ~ 54? km (Figure 51 (right)). The surface isotherms for day 75 (Figure 52) indicate that the locations of both anticyclonic circulations correspond to the relatively warmer spots as seen by the concavities of the 16 and 15.5°C isotherms, and that the position of the cyclonic circulation corresponds to a region where colder isotherms extrude offshore. The cross-

**Figure 51.** Surface isopleths of dynamic height (cm) relative to 2400 m for experiment 2 at day 50 (left) and day 75 (right): Contour interval is 2.0 cm. Dashed lines denote negative values.

stream derivatives of the time averaged (days 65-74) potential vorticity (Figure 53) show both zonal and vertical changes in sign in the upper ocean, near the eastern boundary (within approximately 100 km of the coast), so, since the necessary conditions for barotropic and baroclinic instability are met, both mechanisms could be responsible for the generation of eddies in this experiment.

At this point it is interesting to note that in experiment 1 (with negative wind stress curl) a much more intense eddy field with four anticyclonic eddies developed earlier (day 40) and no cyclonic eddies developed in the experiment. Such a response suggests that while in cases with no wind stress curl, the model may generate eddies with both cyclonic or anticyclonic rotations, for cases with forcing by winds with curl, the model is more likely to generate eddies with rotations consistent with the curl.

From day 75 to day 90, the system of two anticyclonic and cyclonic circulations move southward. By day 90, from the meanders of the surface jet at $y \sim 835$ km, approximately 65 km offshore, a new anticyclone is developing (Figure 54 (left)). The pattern of this eddy field continues to intensify until the end of the experiment (day 105) and is displaced southwestward (Figure 54 (left) and (right)), probably due to advection by the mean flow.

## 2. Experiment 3 (Forcing by a Time Series of the North/South Component of the Wind)

### a. General Picture of the Wind Time Series

In experiment 3, the model was forced by a spatially uniform time series of the north south component of the wind. The time series corresponds to the 6-hourly values of the meridional wind from 1 February to 31 December, 1986, computed from Fleet Numerical Oceanography Center synoptic surface atmospheric pressure analyses, interpolated to a three-degree latitude longitude grid centered at position $39°N$, $10°W$.

A summary of statistics related to the wind time series is shown in Table 4. The mean north south wind for the series was -240 cm s with a standard deviation of 475 cm s. The maximum poleward wind was 1490 cm s and the maximum equatorward wind was -1430 cm s. Monthly means of the north south winds oscillated between 139 cm s in December and -667 cm s in July. February and December were the only months with a poleward mean wind. The stronger equatorward winds (mean values with magnitudes over 370 cm s) occurred from May through August. September had a relatively small mean wind of -16 cm s, but in October the mean of -338 cm s indicated an increased influence of equatorward winds. By December, winds were poleward most of the time and the mean value was 139 cm s. The monthly standard deviations of the 6-hourly north south winds oscillated between a minimum of 256 cm s in October and a maximum of 497 cm s in February. The percentage of time with equatorward winds oscillated between a minimum of 39.2% in February and a maximum of 99.2% in July. Overall, this particular time series had prevailing and stronger equatorward mean winds
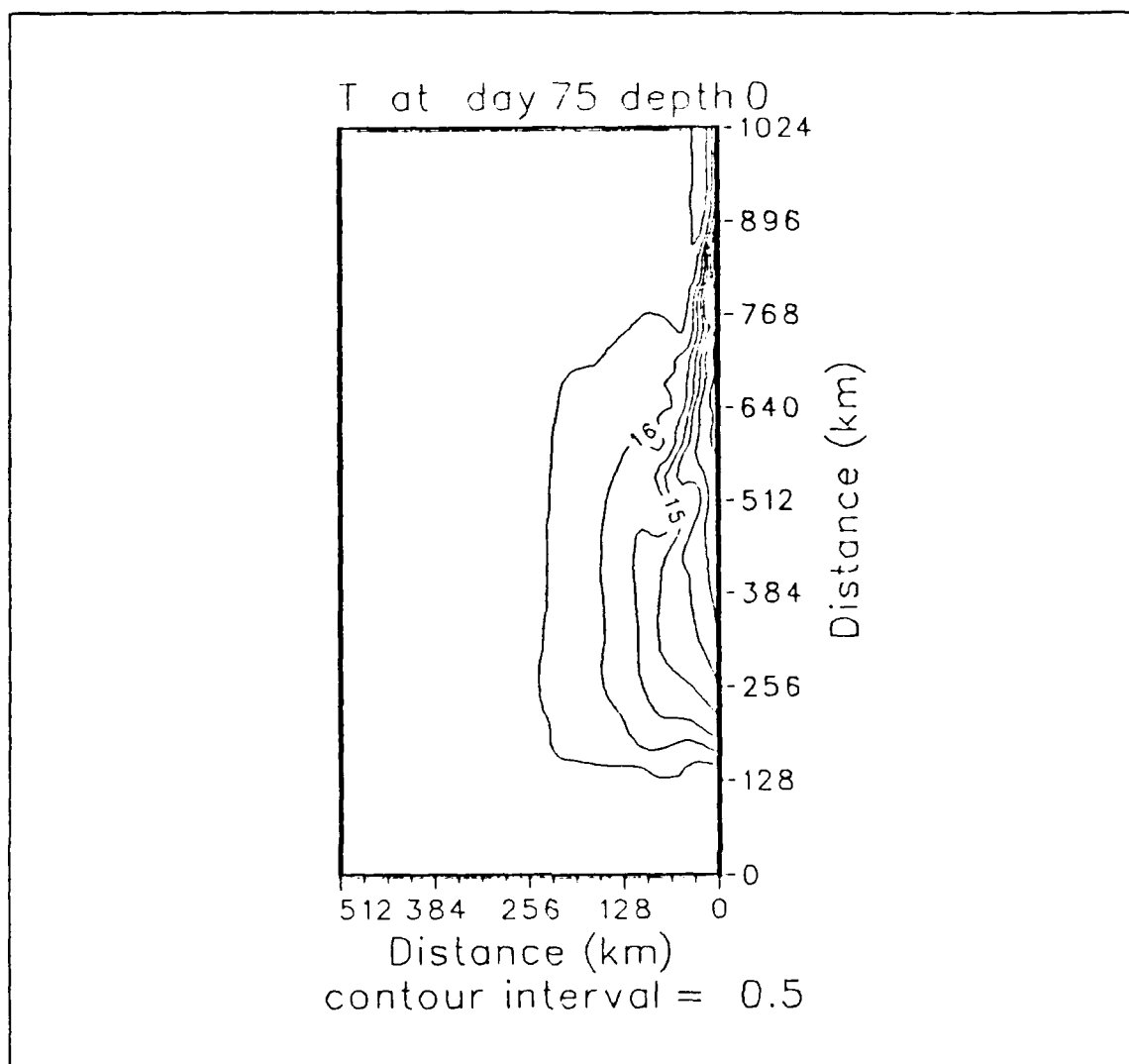
**Figure 52.** Surface isotherms (°C) for experiment 2 at day 75: Contour interval is 1.0°C.

(more than 75% of the time, and means larger than 370 cm/s) during the months from May through August.
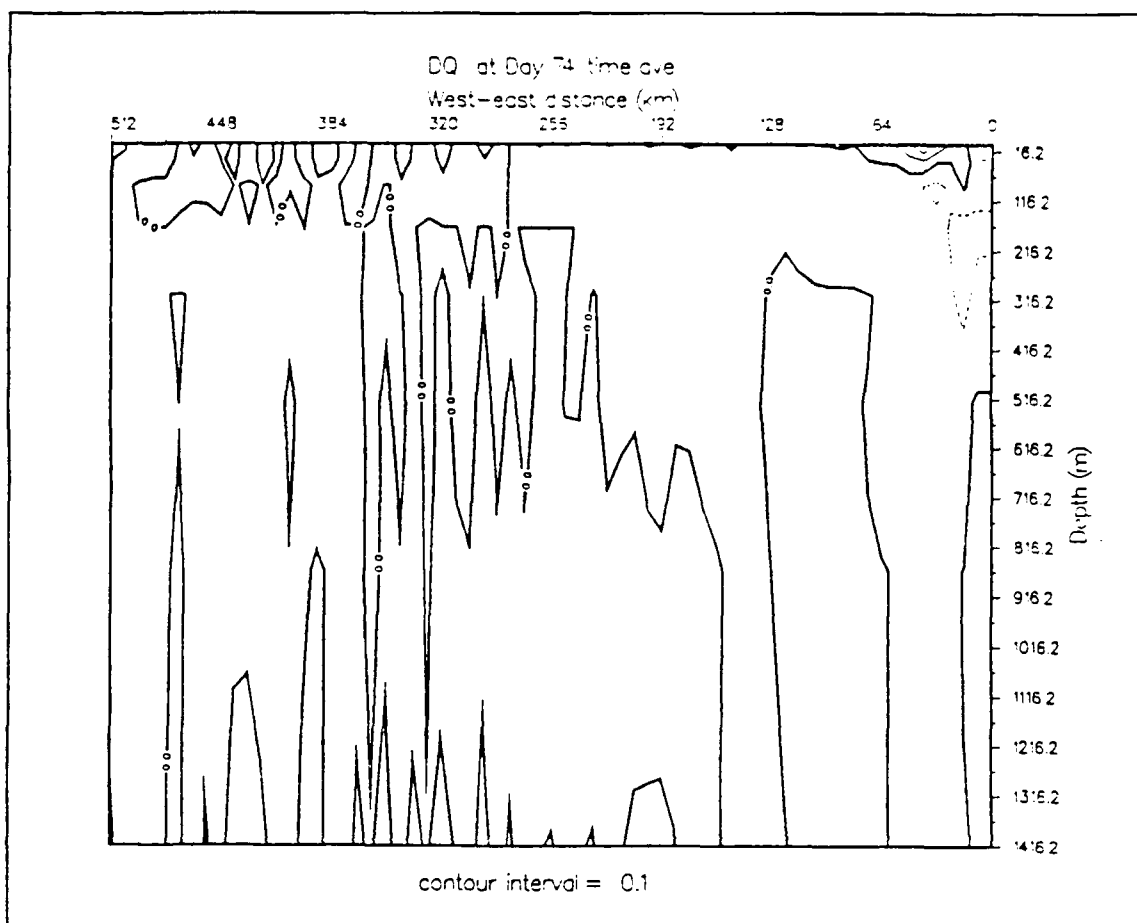
**Figure 53.** Vertical cross-section of the cross-stream derivative of potential vorticity multiplied by the zonal grid size (°C / (m s)) for the time-averaged days 65-74 of experiment 2: Values are scaled by $10^6$. Contour interval is 0.1°C / (m s). Dashed contours denote negative values. The vertical cross-section was taken at y = 544 km.
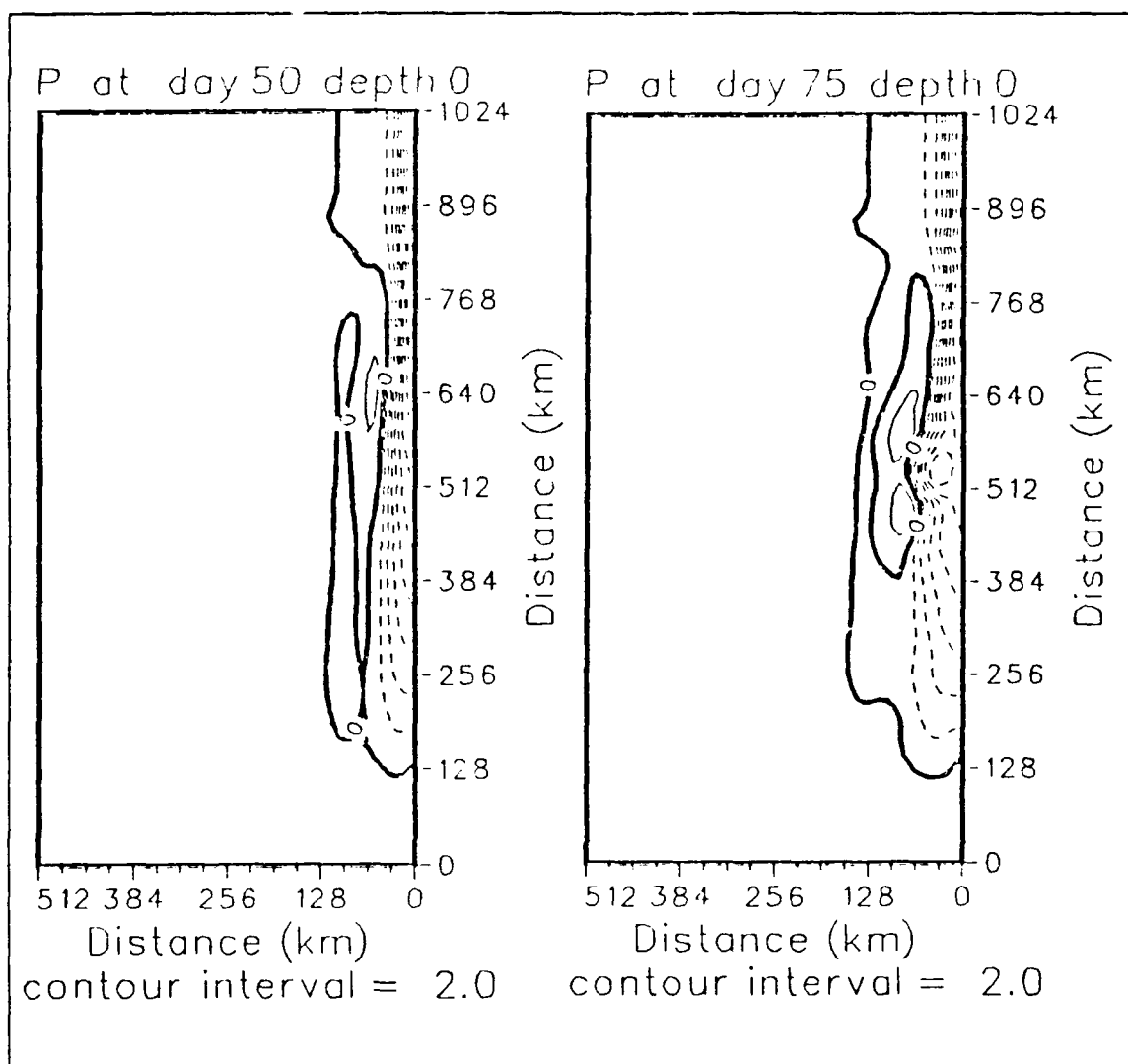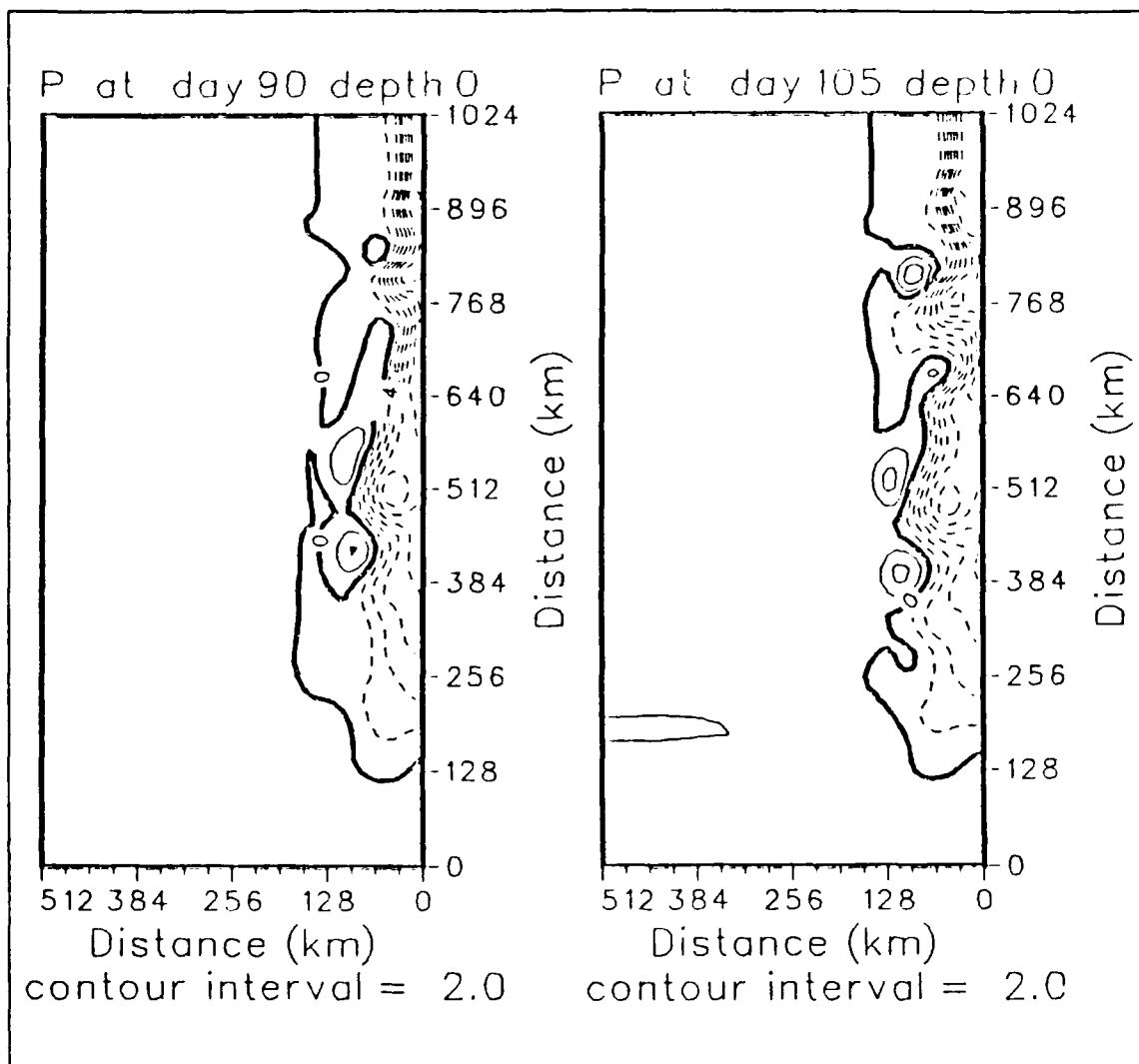
**Figure 54.** Surface isopleths of dynamic height (cm) relative to 2400 m for experiment 2 at day 90 (left) and day 105 (right): Contour interval is 2.0 cm. Dashed lines denote negative values.

Table 4. MONTHLY AND ENTIRE SERIES STATISTICS OF THE NORTH/SOUTH COMPONENT OF THE WIND VELOCITY

| | Mean (cm/s) | Standard deviation (cm/s) | Maximum poleward (cm/s) | Maximum equatorward (cm/s) | Percentage of time with equatorward wind |
|---|---|---|---|---|---|
| February | 109 | 497 | 1390 | -890 | 39.3 |
| March | -287 | 349 | 460 | -1020 | 78.2 |
| April | -254 | 419 | 1020 | -1280 | 75.8 |
| May | -371 | 463 | 710 | -1410 | 75.8 |
| June | -458 | 459 | 550 | -1430 | 80.8 |
| July | -667 | 272 | 200 | -1230 | 99.2 |
| August | -406 | 309 | 570 | -1000 | 88.7 |
| September | -16 | 473 | 1080 | -800 | 60.0 |
| October | -338 | 256 | 590 | -820 | 92.7 |
| November | -55 | 450 | 1230 | -890 | 61.6 |
| December | 139 | 492 | 1490 | -660 | 44.3 |
| February-December | -240 | 475 | 1490 | -1430 | 66.7 |

### b. Response of the Flow to the Wind Forcing

Based on the structure of the time series, a few cases were selected and used to study the response of the flow.

### (1) Poleward Winds

(a) Fluctuating Poleward Winds During a Few Days in the Pre-upwelling Season— Here we focus on the time interval between day 5 (6 February) and day 16 (17 February), in which the dominant poleward winds showed fluctuations with time scales of two or three days (Figure 55). Comparing the cross-sections of alongshore averaged meridional (v) velocity for days 5 and 16 (Figures 56 and 57) we see that the existing equatorward surface current created by previous equatorward winds, eventually disappears and is replaced by a poleward surface coastal current, when the winds reverse. The zonal cross-sections of temperature (not shown) also demonstrate in a consistent fashion with the reversal of the flow, that the 15 and 16°C isotherms in the upper coastal ocean change from an upwelling to a downwelling situation. The response

of the model with a poleward current under the change of forcing to poleward winds is consistent with observations of mean currents over the central Oregon shelf during winter, when the wind is favorable for downwelling (Huyer, 1983).

(b)    Short and Strong Pulses of Poleward Wind— A strong pulse of poleward wind between days 61 and 63 (3 - 5 April) with a peak velocity of about 10 m s (after an existing situation of surface equatorward jet and poleward undercurrent), was used to evaluate the response of the flow. In this short period of time, the equatorward jet rapidly decreases in intensity and shrinks in cross-sectional area, the poleward undercurrent increases in intensity, expands in cross-sectional area, and displaces the weak equatorward current offshore (see Figures 58 and 59). Notice that in comparing this case with the previous one, the equatorward current does persist, but is appreciably weakened, probably due to the less extensive time interval with poleward winds.

### (2)    Equatorward Winds During the Upwelling Season

(a)    Equatorward Winds with Intensification and Relaxation— A common feature of the prevailing equatorward winds during the upwelling season is the sequence of intensification and relaxation with time scales of 4-5 days. Intensification and relaxation are seen along the time record in intervals such as from day 64 to 78 (6 to 20 April), from day 122 to 141 (3 to 22 June),from day 159 to 170 (10 to 21 July), and from day 186 to 210 (6 to 30 August).

The response of the system to intensification and relaxation may be exemplified in the interval between days 135 and 141 (16 and 22 June). Figure 60 shows the time series of the meridional wind velocity for June, which includes the interval used in this example. On day 134 and 135 (16 June) the meridional wind velocities relax very close to zero. The wind then intensifies and reaches a maximum equatorward value of 12.1 m s by the end of day 136 (17 June). Comparing the cross-sections of temperature at $y = 624$ km for day 135 (relaxation, Figure 61) and day 137 (intensification, Figure 61) we notice that the upwelled 15 and $16^{\circ}C$ isotherms respond near the surface with additional offshore displacement, which is consistent with increased offshore Ekman transport (Figure 63 (left) and (right)), as expected by the increased equatorward winds. The vertical structure of the alongshore averaged meridional (v) velocity also shows that, from day 135 up day 137, with the intensification of the wind, the surface jet increases in vertical extent and the cross-sectional area of the poleward undercurrent (values over 2.0 cm s) is considerably reduced (compare Figures 64 and 65).
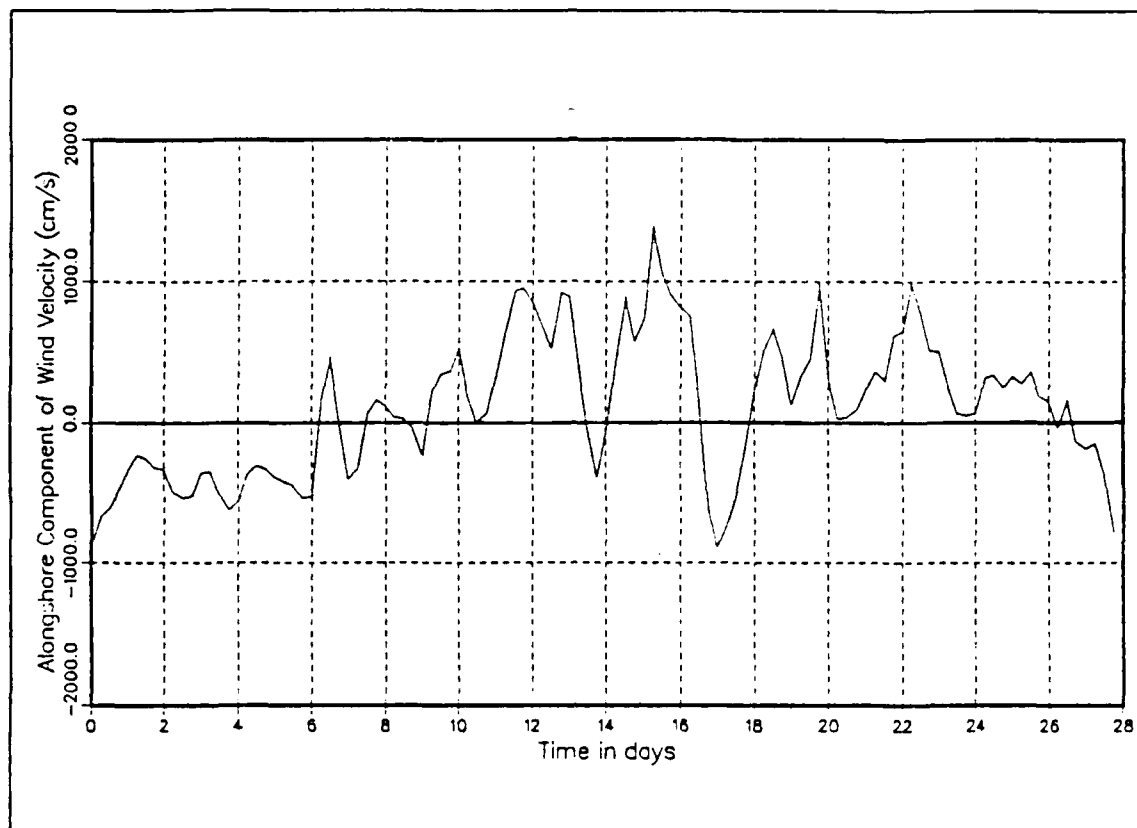
Figure 55.    Time series of the 6-hourly values of the north/south component of the
             wind velocity (cm/s) for February 1986 at position 39°N, 10 °W:    Posi-
             tive and negative values represent poleward and equatorward winds,
             respectively.  Day zero is 1 February 1986.

The meridional (v) velocity in the core of the equatorward jet stays approximately the
same.

From day 137 (18 June) to day 141 (22 June), with the relaxa-
tion of the wind, it is apparent that the equatorward surface current becomes shallower
and the poleward undercurrent increases considerably in size and shoals (Figure 66).
The 15 and 16°C isotherms recede toward the coast responding to the decreased offshore
Ekman transport, due to the relaxation (compare Figure 67 with Figure 62), but the
configuration of the isotherms in the upper 200 m stays upwelled.  Off Oregon, under
variable winds during the upwelling season, observations have shown that isopycnals
remain tilted upward toward the coast while the near-surface density field changes rap-
idly with the wind (Huyer, 1988).  Observed motion of light (warmer) surface waters

V FIELD at Day 5 longshore ave.
West-east distance (km)

contour interval = 2.0

**Figure 56.** Vertical cross-shore section of alongshore-averaged meridional (v) velocity (cm/s) for experiment 3 at day 5: Contour interval is 2.0 cm s. Dashed lines denote equatorward velocities.

onshore when equatorward winds relax and offshore when winds intensify is consistent with the model response just described. An experiment conducted during June and July of 1976, off Portugal in the region of the Nazaré canyon (latitude 39.5°N), using an airborne radiation thermometer to survey sea surface temperature, showed that with the slackening of the northerly winds, the thermal pattern changed consistently with a shoreward penetration of warmer oceanic water (Fiuza, 1982). A sequence of thermal infrared satellite images between 31 August and 2 September 1981, under the action of upwelling favorable winds, showed a continuous band of upwelled waters at the north coast of Portugal, as far south as Cape Roca (latitude 38.6°N), an isolated focus of upwelling on the southwest coast, and offshore (over the slope) a meridional band with

78
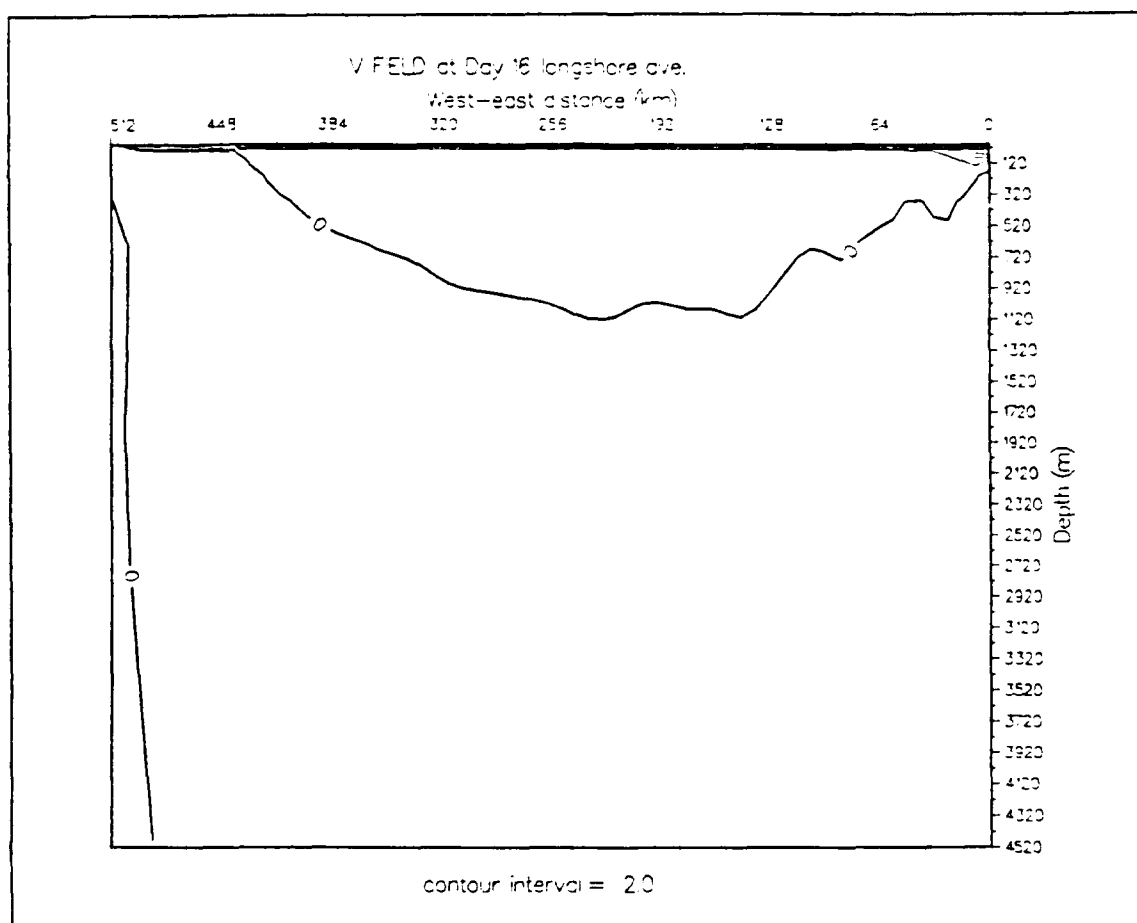
Figure 57. Vertical cross-shore section of alongshore-averaged meridional (v) velocity (cm/s) for experiment 3 at day 16: Contour interval is 2.0 cm s. Dashed lines denote equatorward velocities.

large zonal gradients of temperature. During the subsequent relaxation of the equatorward winds, the satellite data for 3,4, and 10 September 1981 indicated the gradual disappearance of the upwelling focus, the weakening of the thermal gradients, and a progressive shoreward advance of warmer oceanic waters (Fiúza, 1984). Thus, the results that we get in experiment 3, under relaxation of the upwelling favorable winds, seem consistent with observations off both Oregon and Portugal.

(b) Quasi-steady Equatorward Winds During a Few Days After Short Periods of Poleward Winds— A situation that (in this particular year) is repeated a few times, consists of moderate quasi-steady equatorward winds of approximately 5 m s that persist for about 6-9 days, preceded by weak poleward winds. Examples may

**V FIELD at Day 61 longshore ave.**

West-east distance (km)

contour interval = 2.0
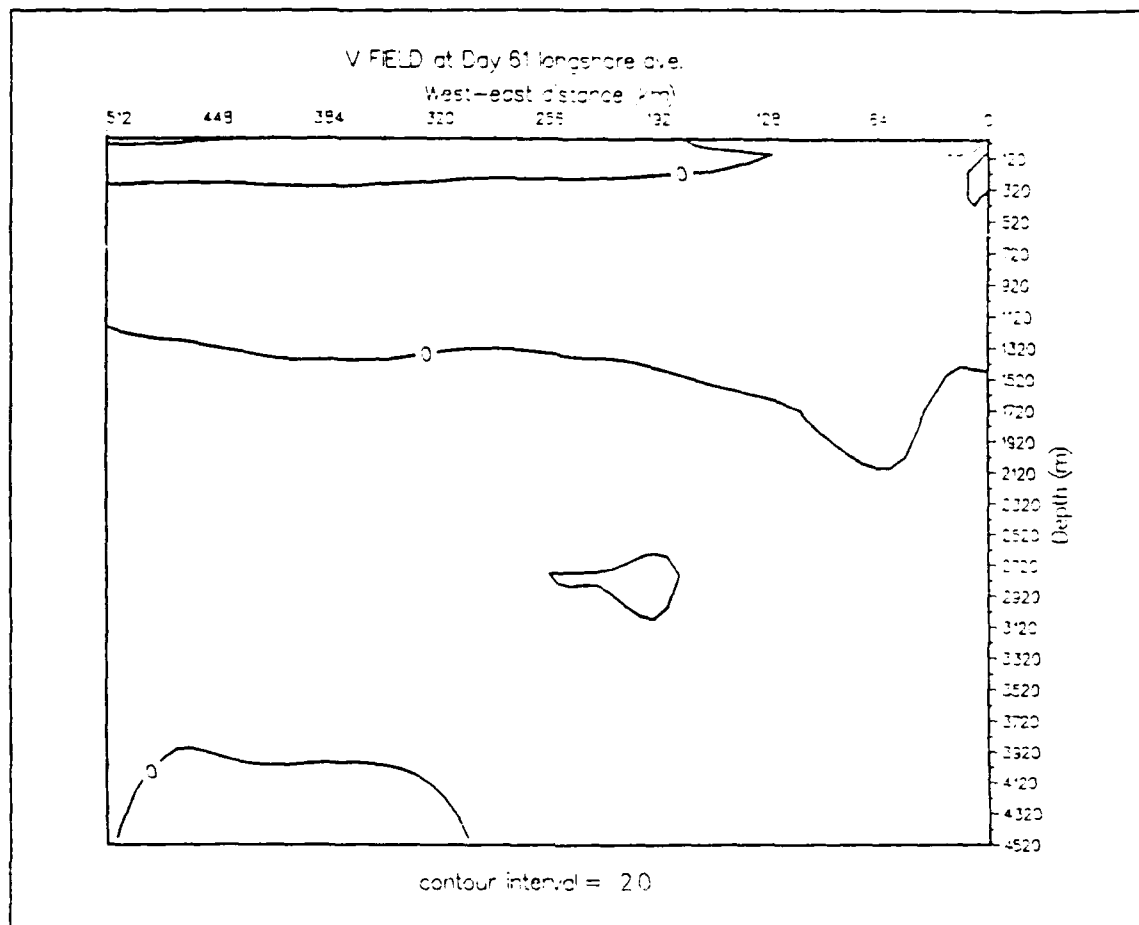
**Figure 58.** Vertical cross-shore section of alongshore-averaged meridional (v) velocity (cm/s) for experiment 3 at day 61: Contour interval is 2.0 cm s. Dashed lines denote equatorward velocities.

be seen in the time series (Figure 3) in the intervals from day 30 to 37 (3 to 10 March), from day 45 to 52 (18 to 25 March), from day 55 to 60 (28 March to 2 April), from day 82 to 91 (24 April to 3 May), from day 97 to 102 (8 to 14 May) and from day 256 to 264 (15 to 23 October). Such situations in this particular series seem to be more frequent in the early upwelling season (March and April). The response of the flow is very similar to that described previously for the intensification. That is, the equatorward surface current near the coast tends to expand in cross-section and the poleward undercurrent is reduced or even disappears, as shown in Figure 68 and Figure 69 which represent the beginning (day 96 or 8 May) and end (day 102 or 14 May) of the interval with quasi-steady, moderate, equatorward winds.
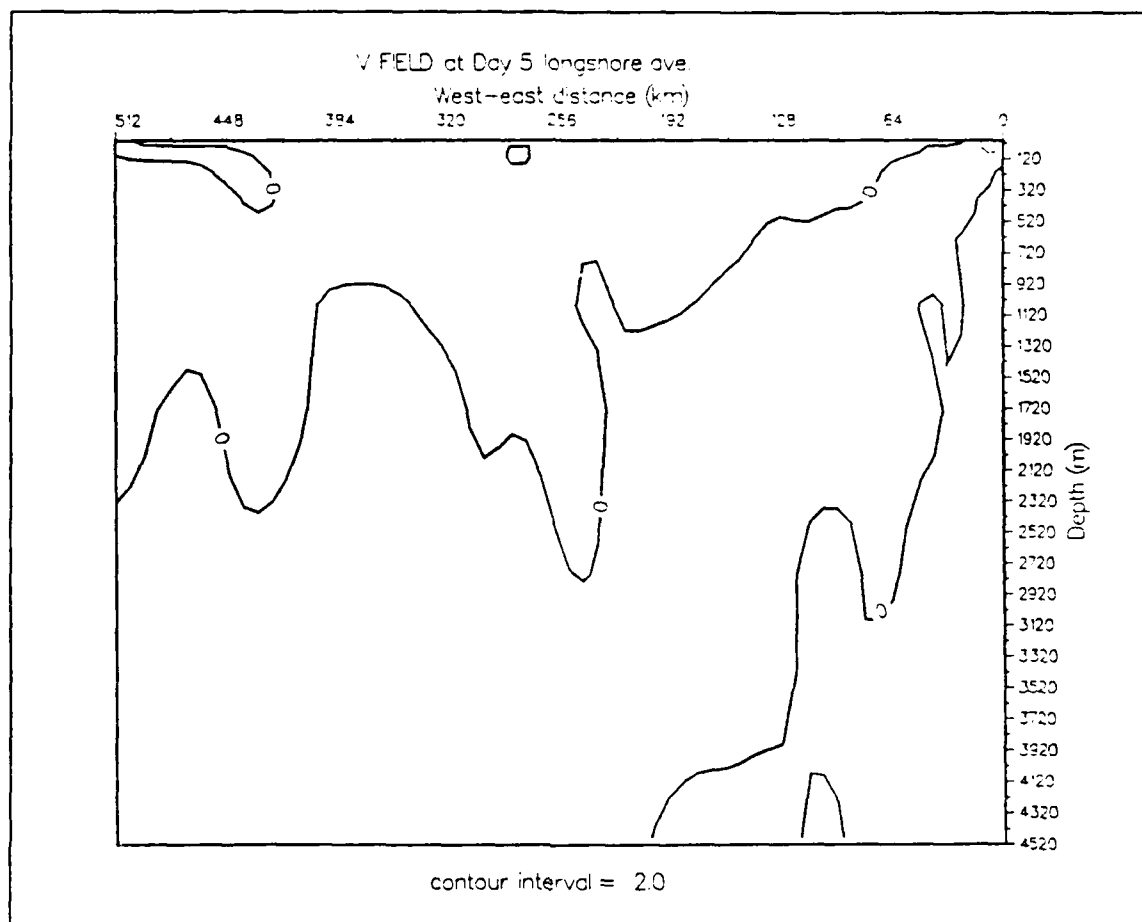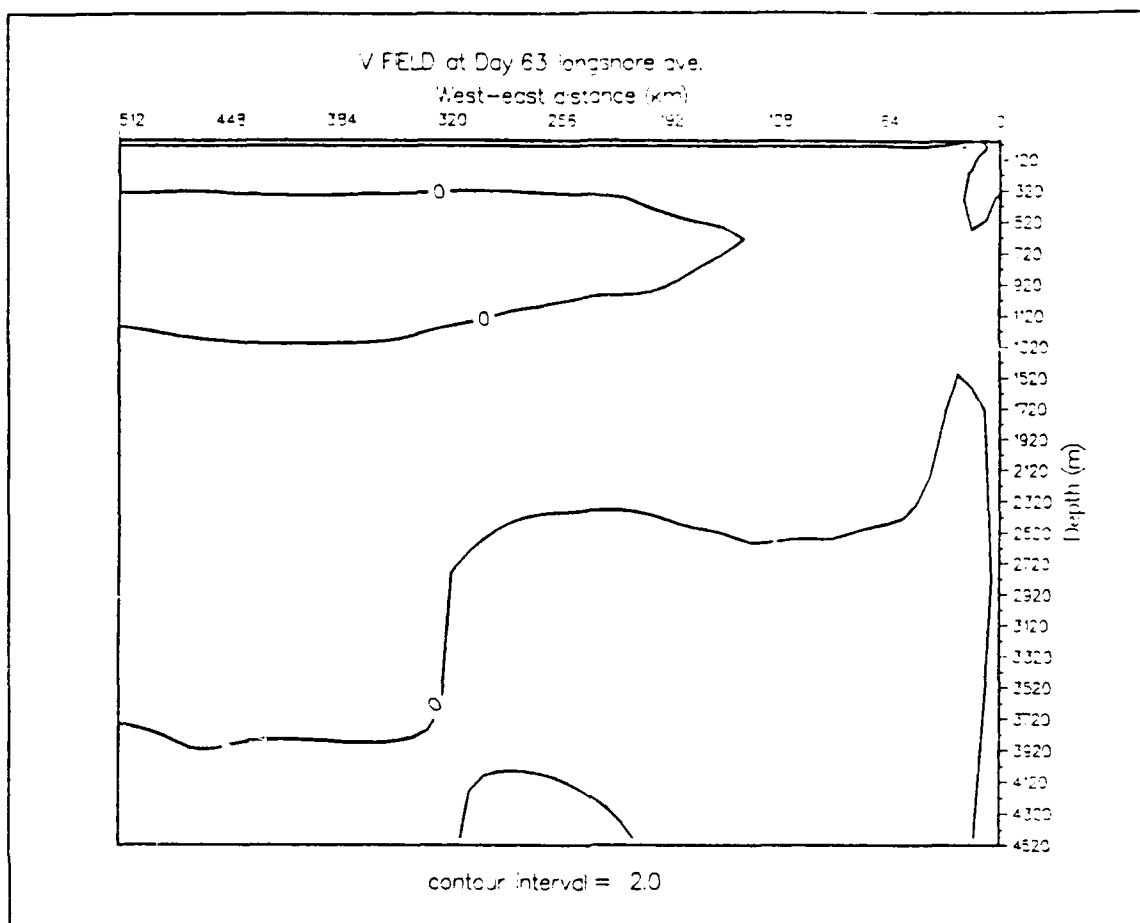
**Figure 59.** Vertical cross-shore section of alongshore-averaged meridional (v) velocity (cm/s) for experiment 3 at day 63:   Contour interval is 2.0 cm s. Dashed lines denote equatorward velocities.

In summary, with increased equatorward winds, the surface equatorward jet responds by expanding its cross-sectional area and increasing its velocity while the poleward undercurrent responds by reducing its cross-sectional size and decreasing its velocity. Relaxation of equatorward winds causes the poleward undercurrent to expand and shoal. Velocities measured on a zonal section off Point Sur, California in November 1988 showed that the inner shelf poleward flow along the coast can be weak to nonexistent during strong upwelling, but strengthens and propagates seaward during relaxations (Reece, 1989). In a consistent fashion, the model responds to intensified upwelling favorable winds by submerging the poleward undercurrent, and responds to wind relaxations by allowing the poleward current to shoal.
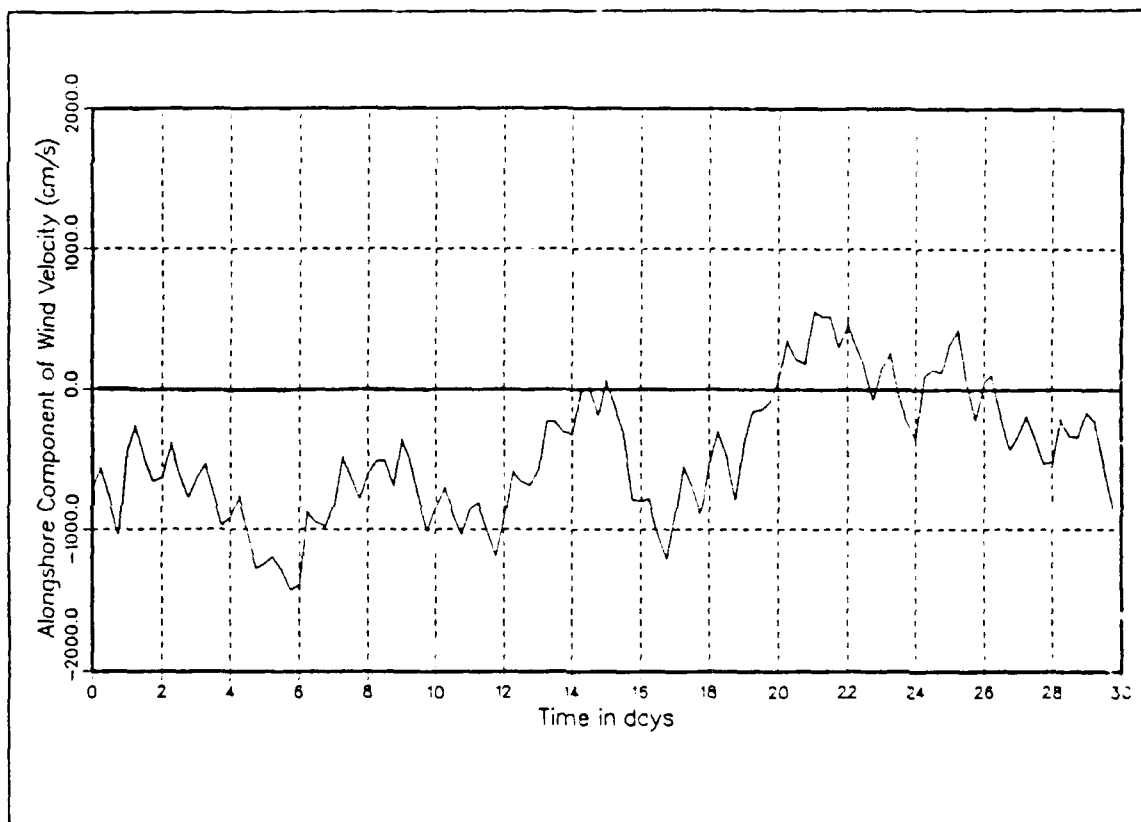
**Figure 60.** Time series of the 6-hourly values of the north/south component of the
wind velocity (cm/s) for June 1986 at position 39°N, 10 °W: Positive
and negative values represent poleward and equatorward winds, re-
spectively. Day zero is 1 June 1986 (day 120 in experiment 3).

*(3)    Development of Eddies During the Upwelling Season.* On day 173 (24
July), as seen in the field of dynamic height of the surface relative to 2400 m (Figure 70
(right)), there is a meandering of the surface jet between positions v ~ 640 km and y ~
896 km, which relates and is in phase with the thermal surface signal shown for the same
date in Figure 70 (left). The estimated wave length for the meander is 125 km.

By day 188 (8 August) the meander has increased in amplitude, a
closed anticyclonic circulation develops at y ~ 748 km, and the surface temperature
pattern shows extended offshore cold water filaments corresponding to the cyclonic cir-
culations of the meandering jet at y ~ 720 km and y ~ 841 km ( Figure 71(left) and
(right)). The cross-stream derivatives of the time averaged (days 180-189) potential
vorticity (Figure 72) show a change in sign from positive above to negative below,
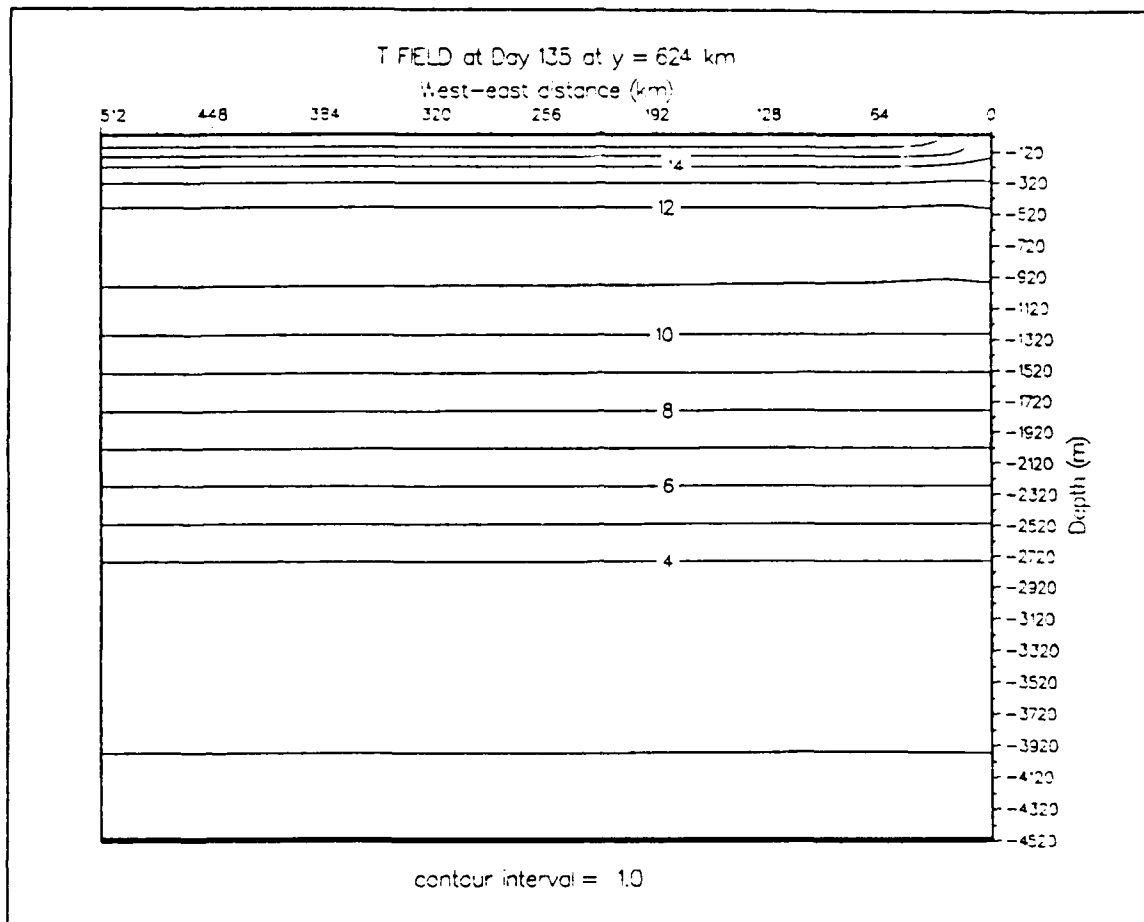
**Figure 61.** Vertical cross-shore section of temperature (°C) at y = 624 km for experiment 3 at day 135:  Contour interval is 1.0°C.

across a horizontal line at a depth of about 35 m, which corresponds to a necessary condition for baroclinic instability. Therefore a possible mechanism for the generation of the eddies during the upwelling season is the baroclinic instability due to the vertical shear associated with the equatorward surface jet and poleward undercurrent.

On day 197 (17 August), as seen in the field of dynamic heights of the surface relative to 2400 m (Figure 73 (right)) the anticyclone has expanded in size (as compared with day 188) and two new closed cyclonic circulations show up at y ~ 832 km and y ~ 704 km. The closed anticyclonic circulation is also identified by the zonal cross-section at y = 736 km representing the vertical structure of the temperature and meridional (v) velocity on day 197 (Figures 74 and 75). In the position of the warm core eddy (centered at about 64 km offshore) the 17°C isotherm is displaced from the surface
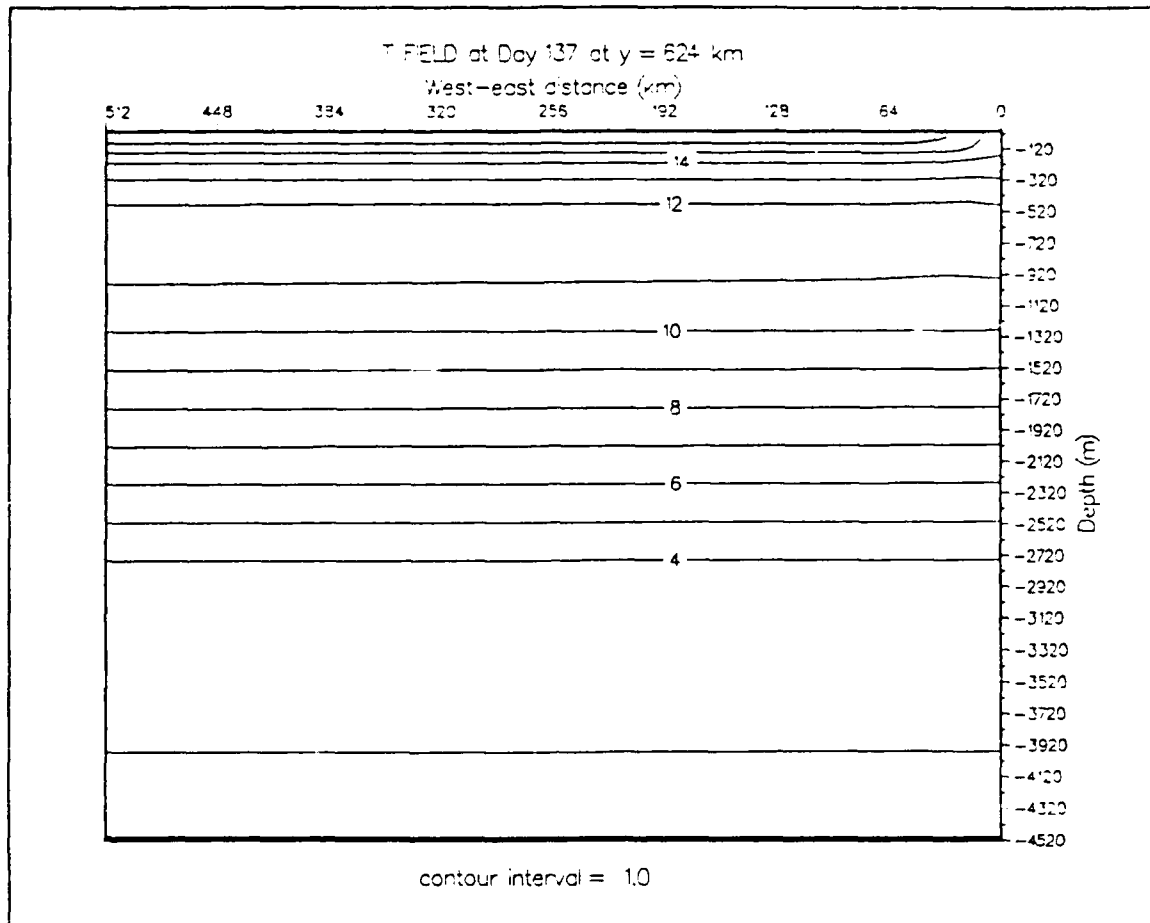
**Figure 62.** Vertical cross-shore section of temperature (°C) at y = 624 km for experiment 3 at day 137: Contour interval is 1.0°C.

downward as much as 38 m and rises back to the surface. Consistent with this thermal structure, the meridional (v) velocity is towards the north (larger than 2 cm s in the upper 100 m) on the west side of the eddy and southward (larger than 2 cm s in upper 300 m) on the east side, where it interacts with the southward coastal jet. The northern and southern closed cyclonic circulations can also be recognized by looking at the structure of the isotherms and meridional (v) velocities in the vertical zonal sections across the eddies. For the southern cyclone, at y = 704 km, the configuration of the coastal isotherms in the upper 300 m shows a cold dome (raised isotherms) in the central position of the eddy (Figure 76). As seen in Figure 77, the distribution of the meridional (v) velocity is indicative of a southward current on the west side of the cyclone (between 24 and 74 km from the coast) and a northward current on the east side of the cyclone
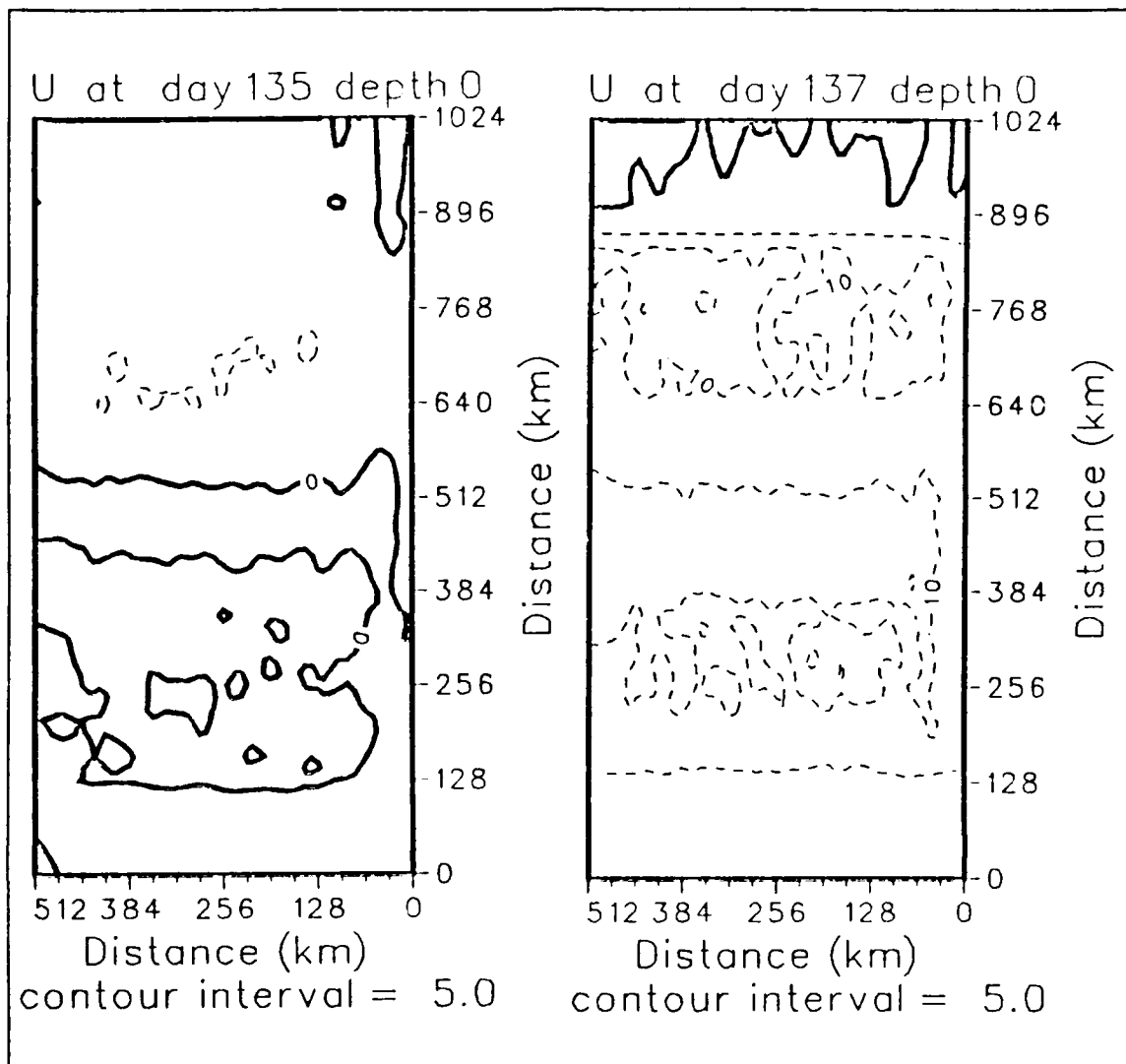
**Figure 63.** Surface isopleths of zonal (u) velocity (cm/s) for experiment 3 at day 135 (left) and day 137 (right): Contour interval is 5.0 cm s. Dashed lines denote offshore velocities.

(within 24 km from the coast). The vertical extent of both cyclonic eddies is estimated to be about 300 m. In between a dipole pair of eddies composed of the anticyclone and the northern cyclone (Figure 73 (right)), lies a cold water filament identified by the relative maximum offshore displacement of the $16.5°C$ isotherm, that at $y \sim 705$ km gets as far as 62 km from the coast (Figure 73 (left)).

**Figure 64.** Vertical cross-shore section of alongshore-averaged meridional (v) velocity (cm/s) for experiment 3 at day 135: Contour interval is 2.0 cm s. Dashed lines denote equatorward velocities.

By day 213 (2 Septemb.: J second closed anticyclonic circulation is apparent in the field of dynamic height of the surface relative to 2400 m at approximately y = 848 km (Figure 78 (left)). The structures of the temperature and meridional (v) velocities in the zonal vertical sections (not shown) are also indicative of a warm core ring with an anticyclonic circulation centered at about 77 km offshore. The vertical extent of the anticyclonic eddy, as seen from the meridional (v) velocity and temperature structures (not shown), is about 450 m.

From day 213 to day 225 (from 2 to 14 September), each of the cyclonic circulations splits in two and results in four closed cyclonic circulations, that span the coast with the dominant axis along the coast (Figure 78 (left) and (right)). The

86
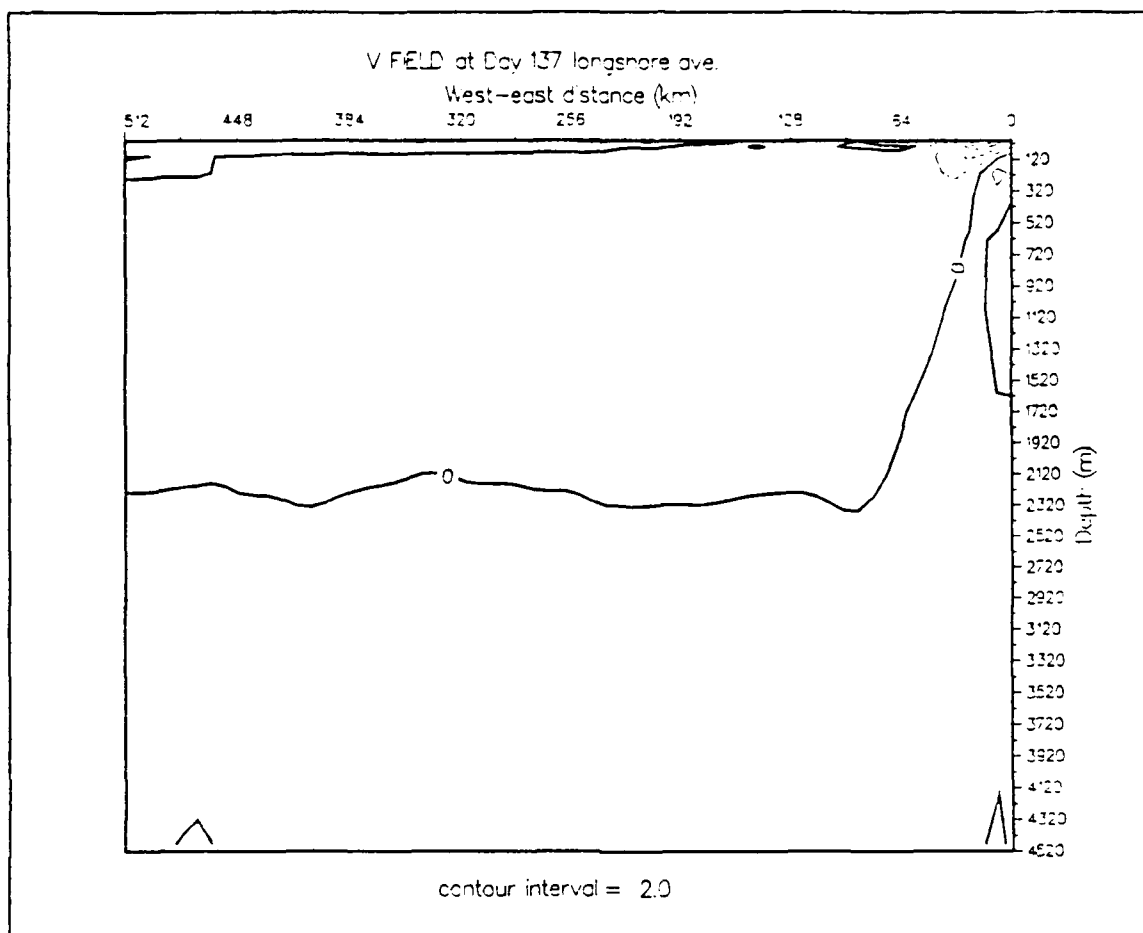
**Figure 65.** Vertical cross-shore section of alongshore-averaged meridional (v) velocity (cm/s) for experiment 3 at day 137:   Contour interval is 2.0 cm s. Dashed lines denote equatorward velocities.

cross-section of the alongshore averaged meridional (v) velocity (not shown) shows a poleward nearshore surface current within about 30 km of the coast, with speeds above 2 cm s in the upper 200 m. Offshore of 30 km, a southward surface current is evident. From day 225 to day 270 (from 14 September to 29 October), the two anticyclones propagate southwestward, probably due to a combination of advection by the mean flow and $\beta$-induced motion.

*(4)* *End of the Upwelling Season.*   The cyclonic circulations that spanned the coast become almost imperceptible by day 270 (Figure 79 (left)). The coastal circulation consists of a weak equatorward current offshore and a weak poleward surface current nearshore. The weakening of the eddy field near the coast may correspond to a

Figure 66.    Vertical cross-shore section of alongshore-averaged meridional (v) veloc-
ity (cm/s) for experiment 3 at day 141:    Contour interval is 2.0 cm s.
Dashed lines denote equatorward velocities.

real decrease of energy in the mesoscale features by the end of the upwelling season.
During November and December, the alongshore winds, with decreased mean
equatorward velocities and periods of moderate or strong poleward velocities (9 to 10
November, 12 to 13 November, 27 November to 7 December), have decreased the
equatorward surface current and probably weakened the eddies by modifying the ther-
mal structure.    By the end of the experiment on day 332 (30 December), the two
anticyclonic eddies no longer exist, three very weak cyclonic circulations are still evident,
and the surface equatorward current is now much less intense and has a smaller cross-
sectional area than during the peak of the upwelling season (Figure 79 (right)).
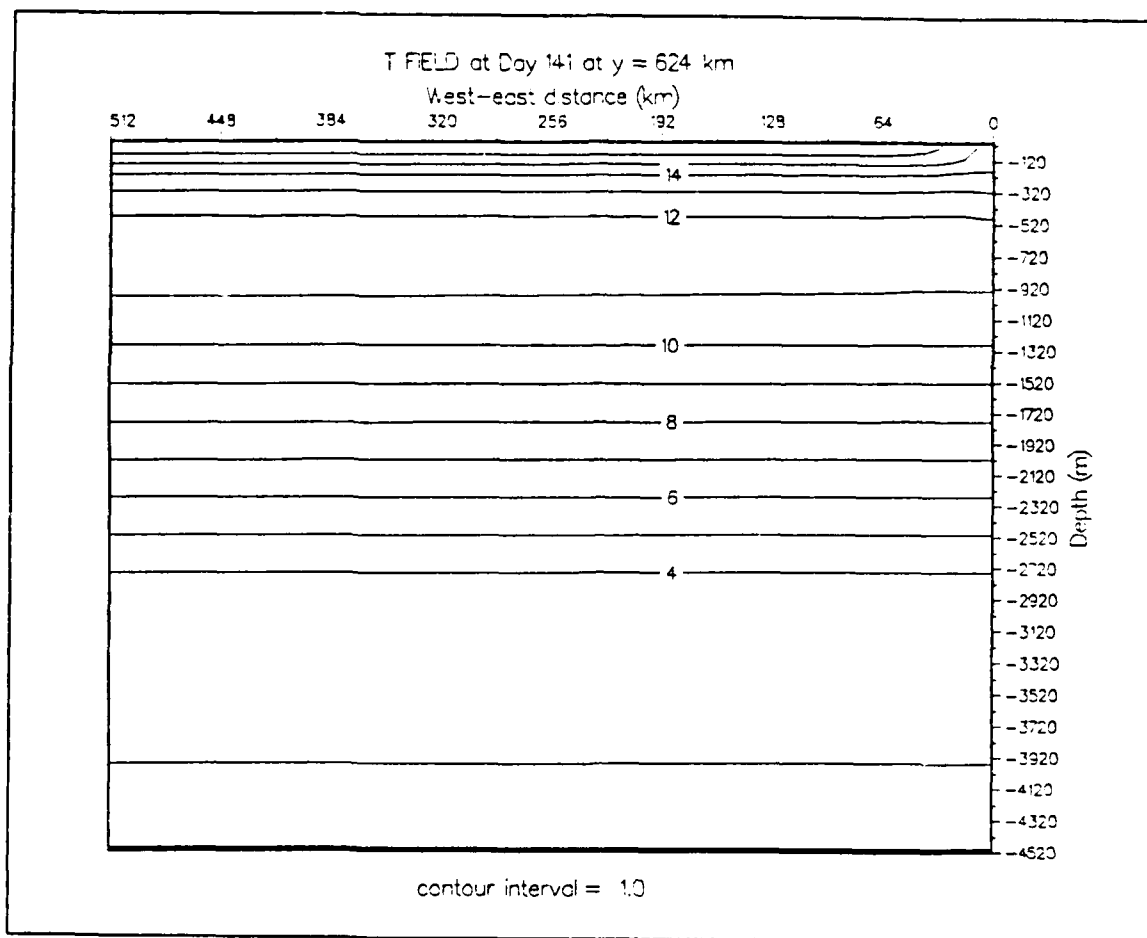
**Figure 67.** Vertical cross-shore section of temperature (°C) at y = 624 km for experiment 3 at day 141: Contour interval is 1.0°C.

V FELD at Day 96 longshore ave.
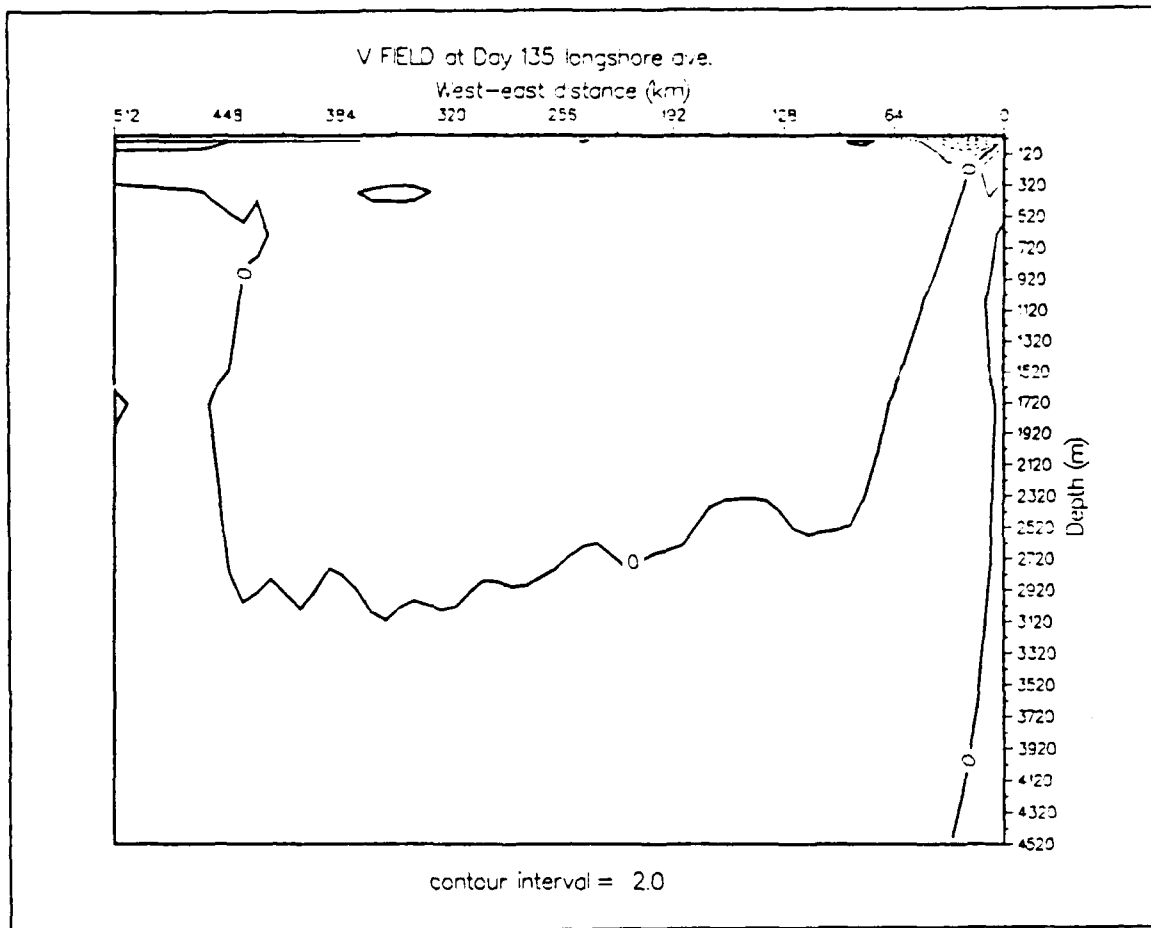West—east distance (km)

contour interval = 2.0
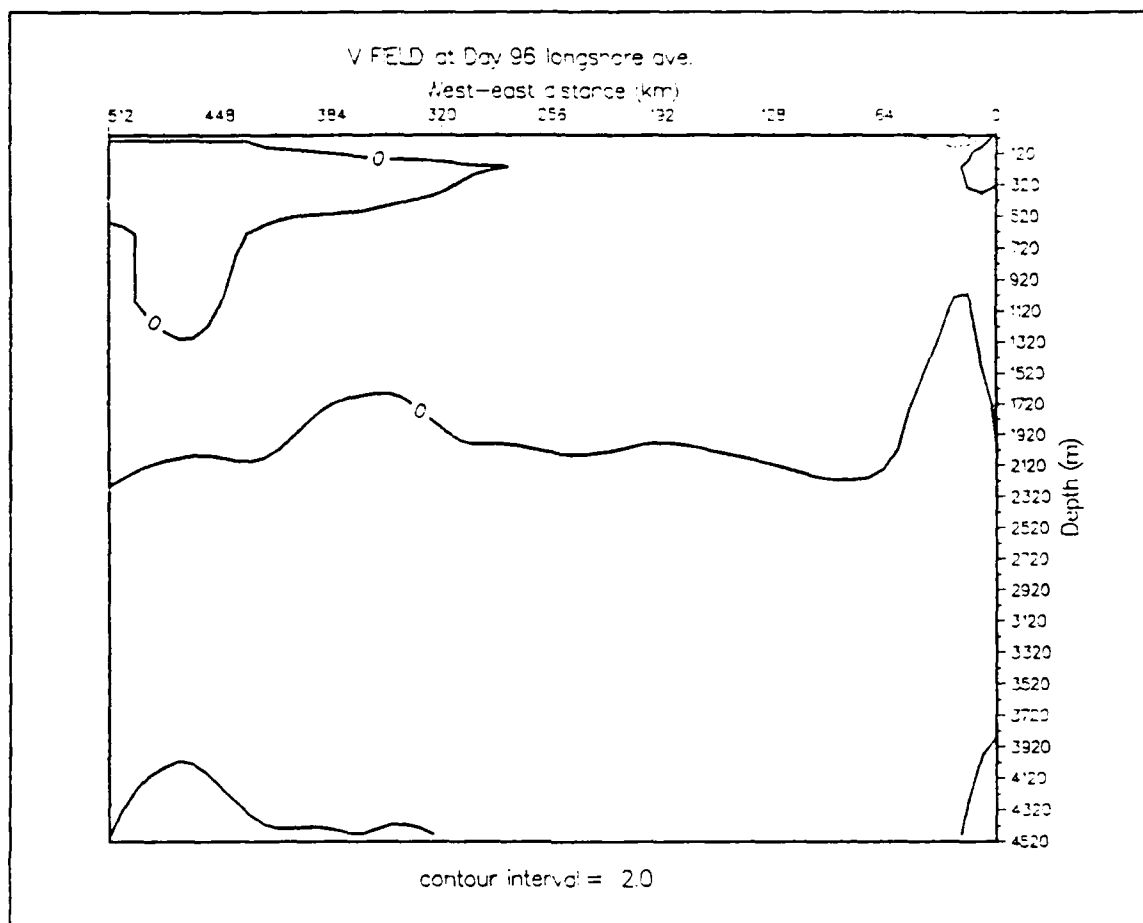
**Figure 68.** Vertical cross-shore section of alongshore-averaged meridional (v) velocity (cm/s) for experiment 3 at day 96: Contour interval is 2.0 cm/s. Dashed lines denote equatorward velocities.
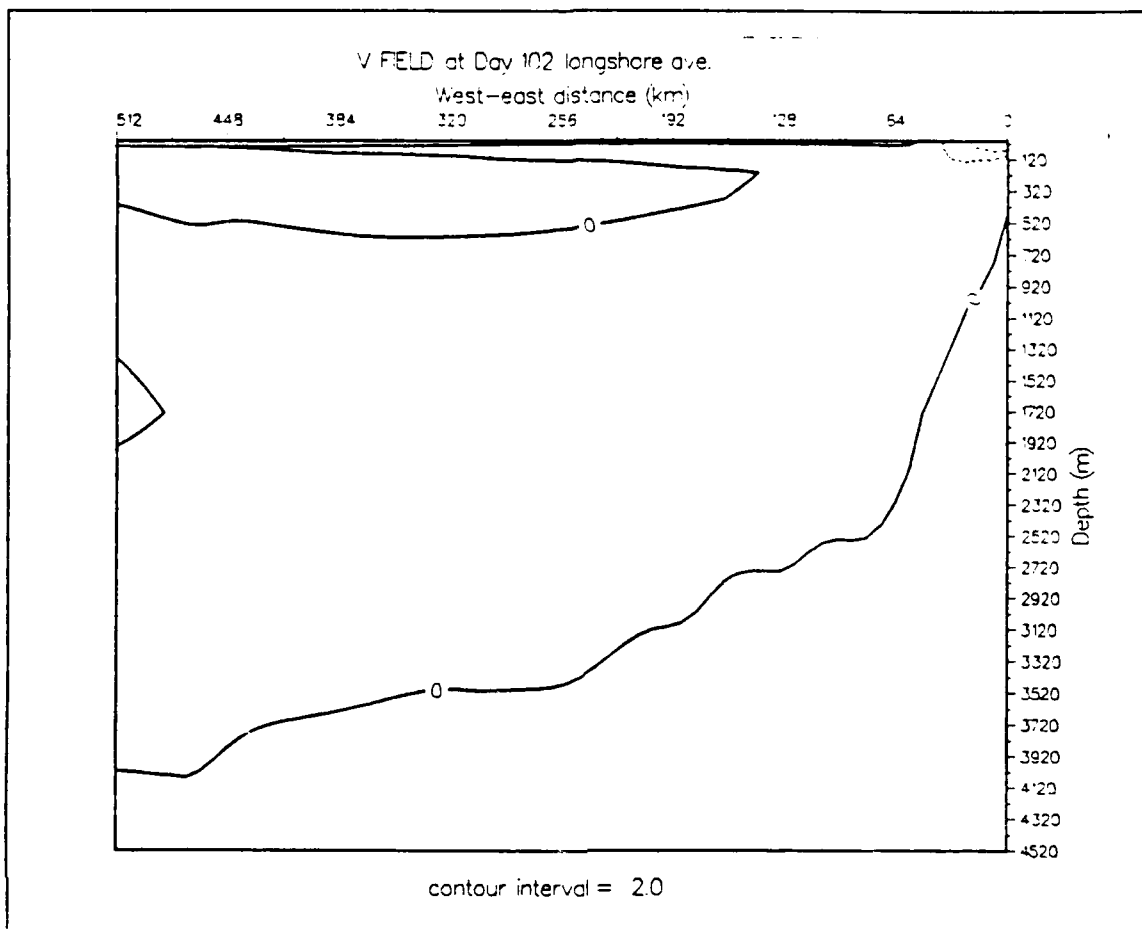
**Figure 69.** Vertical cross-shore section of alongshore-averaged meridional (v) velocity (cm/s) for experiment 3 at day 102: Contour interval is 2.0 cm. s. Dashed lines denote equatorward velocities.
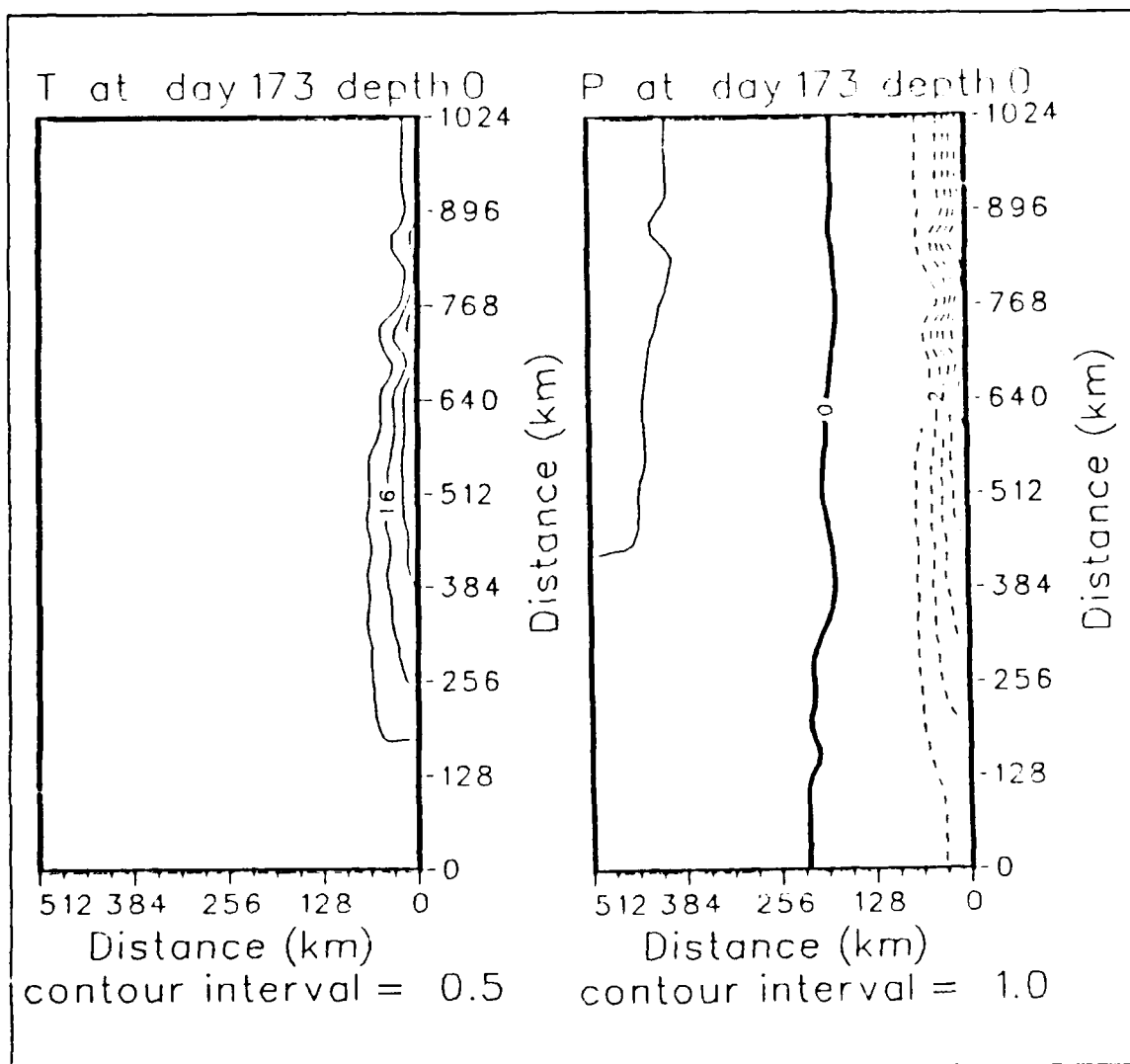
Figure 70.    Surface isopleths of (left) temperature (°C) and (right) dynamic height (cm) relative to 2400 m for experiment 3 at day 173:   Contour interval is 0.5°C for temperature and 1.0 cm for dynamic height. Dashed lines denote negative values.
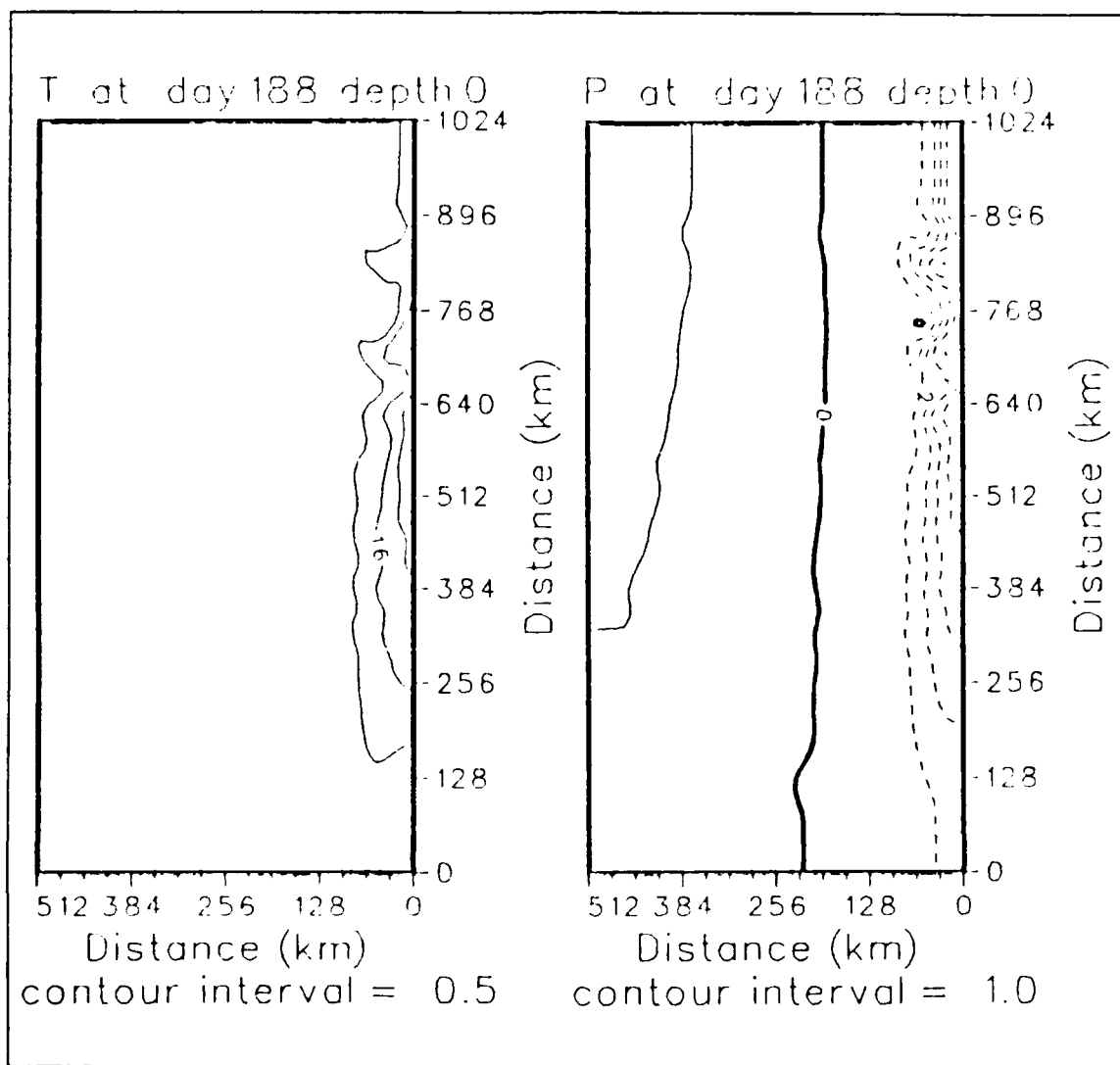
**Figure 71.** Surface isopleths of (left) temperature (°C) and (right) dynamic height (cm) relative to 2400 m for experiment 3 at day 188: Contour interval is 0.5°C for temperature and 1.0 cn. for dynamic height. Dashed lines denote negative values.
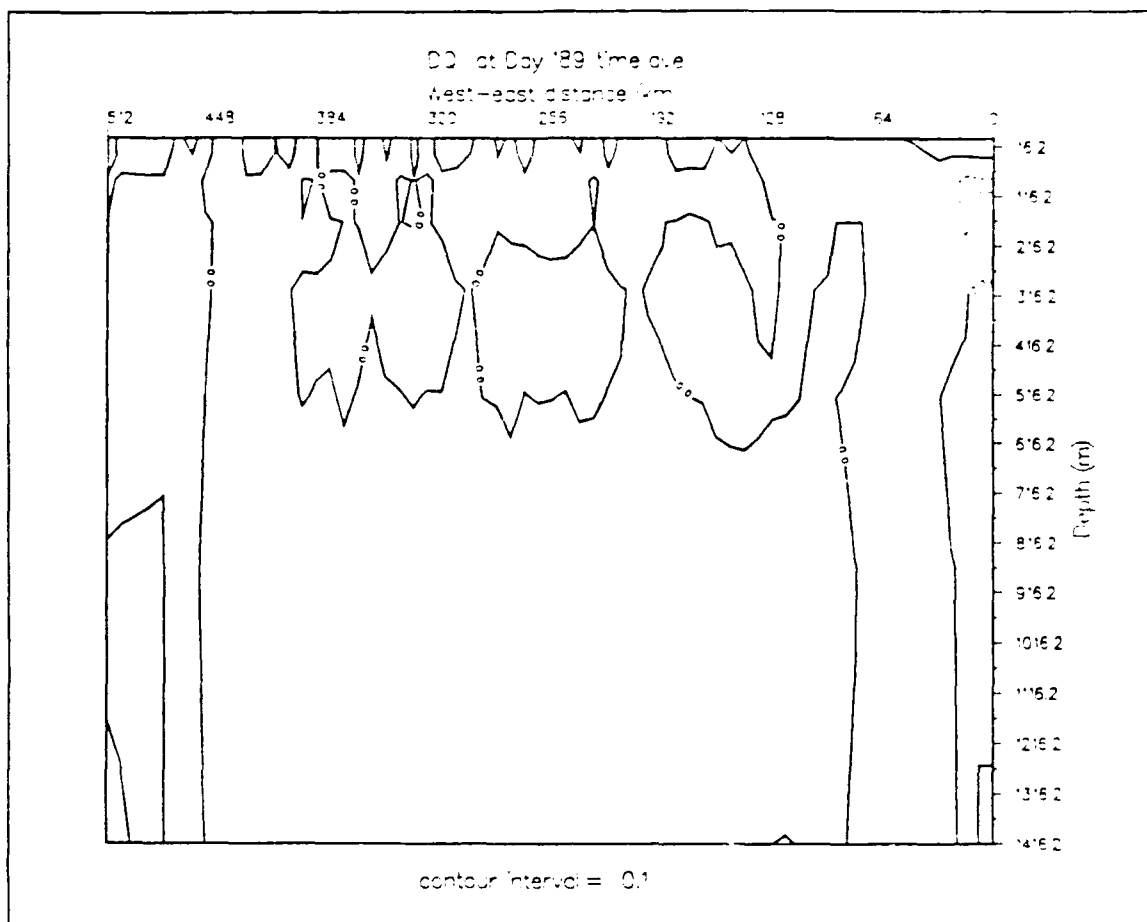
**Figure 72.** Vertical cross-section of the cross-stream derivative of potential vorticity multiplied by the zonal grid size (°C / (m s)) for the time-averaged days 180-189 of experiment 3: Values are scaled by $10^6$. Contour interval is 0.1°C / (m s). Dashed contours denote negative values. The vertical cross-section was taken at y = 752 km.
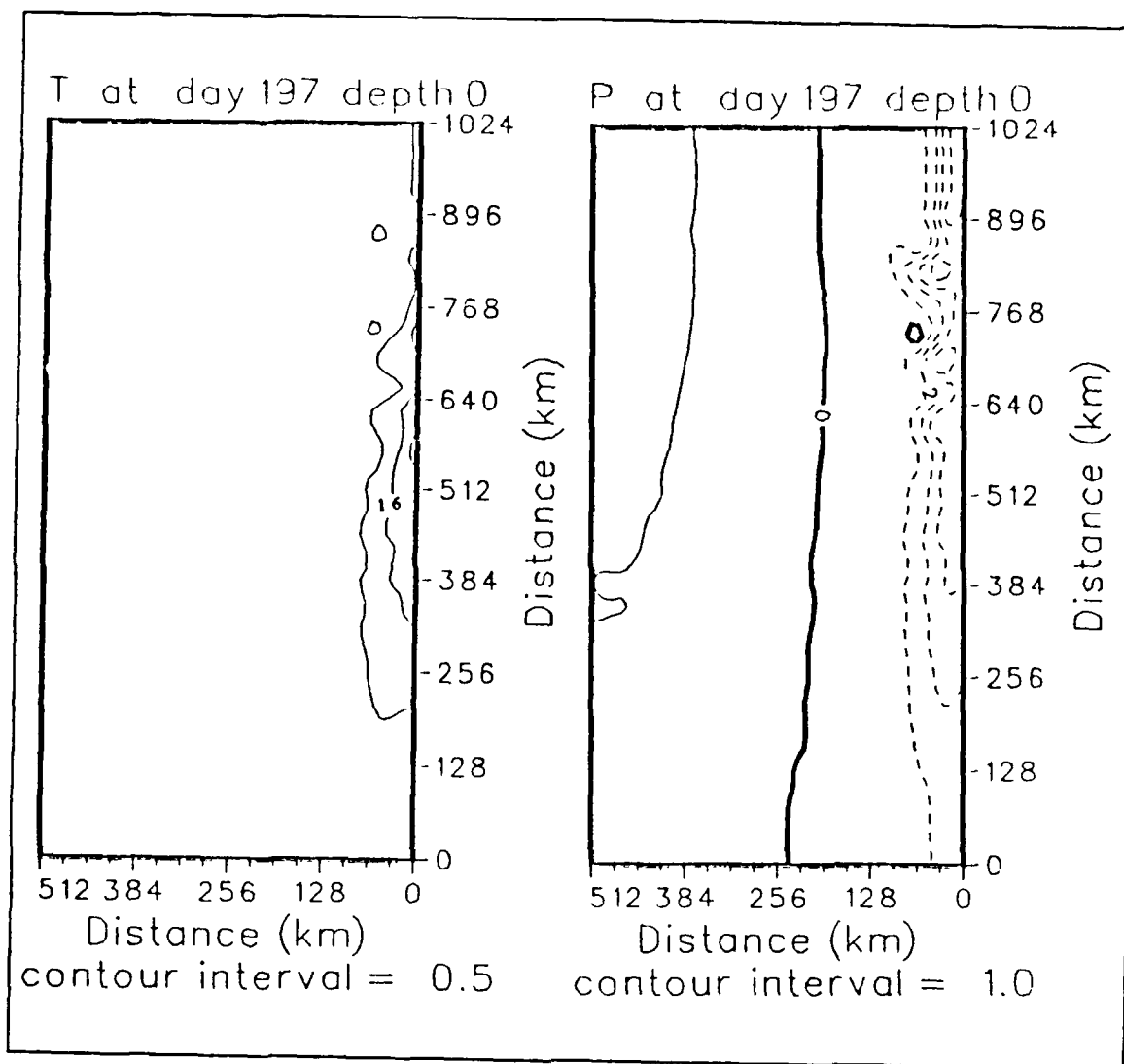
**Figure 73.** Surface isopleths of (left) temperature (°C) and (right) dynamic height (cm) relative to 2400 m for experiment 3 at day 197: Contour interval is 0.5°C for temperature and 1.0 cm for dynamic height. Dashed lines denote negative values.
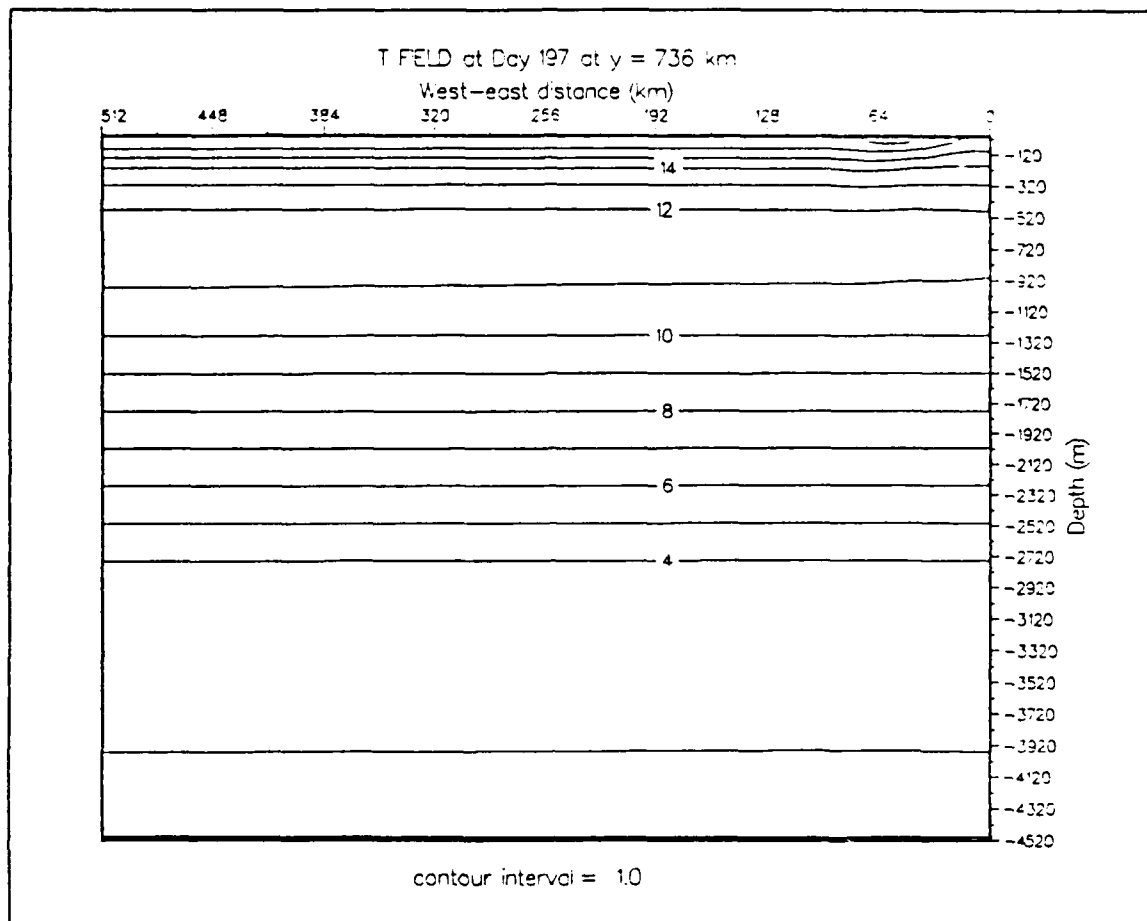
**Figure 74.** Vertical cross-shore section of temperature (°C) at y = 736 km for experiment 3 at day 197:   Contour interval is 1.0°C.
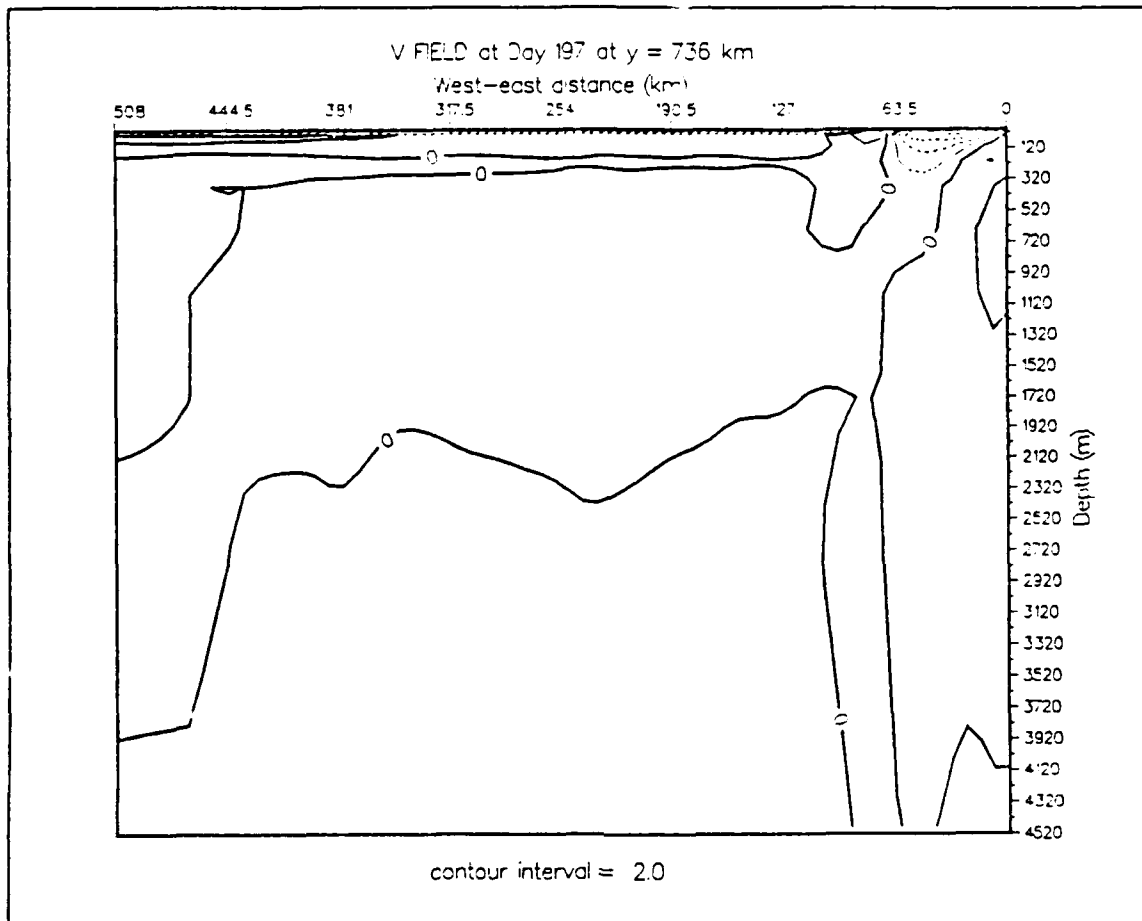
**Figure 75.** Vertical cross-shore section of meridional (v) velocity (cm/s) at y = 736 km for experiment 3 at day 197: Contour interval is 2.0 cm s. Dashed lines denote equatorward velocities.
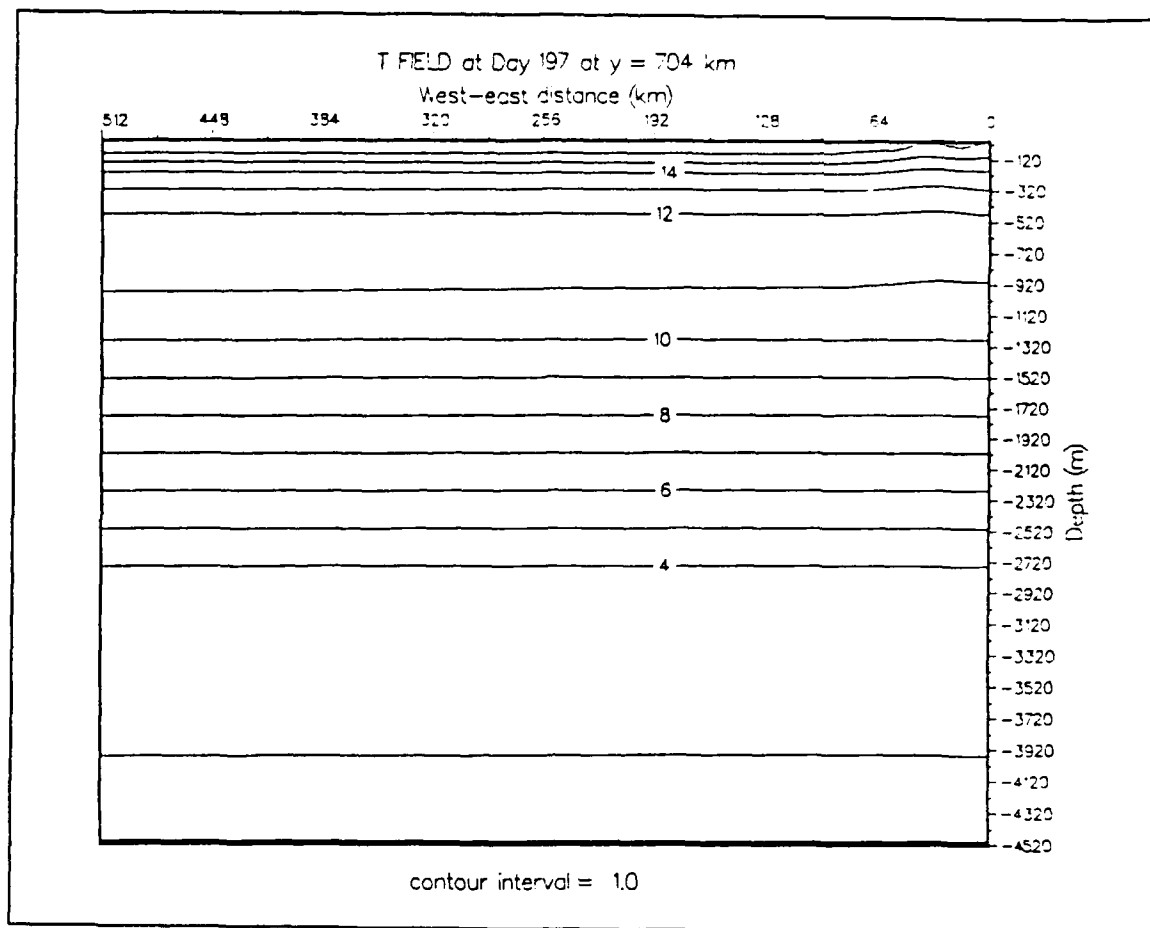
**Figure 76.** Vertical cross-shore section of temperature (°C) at y = 704 km for experiment 3 at day 197: Contour interval is 1.0°C.
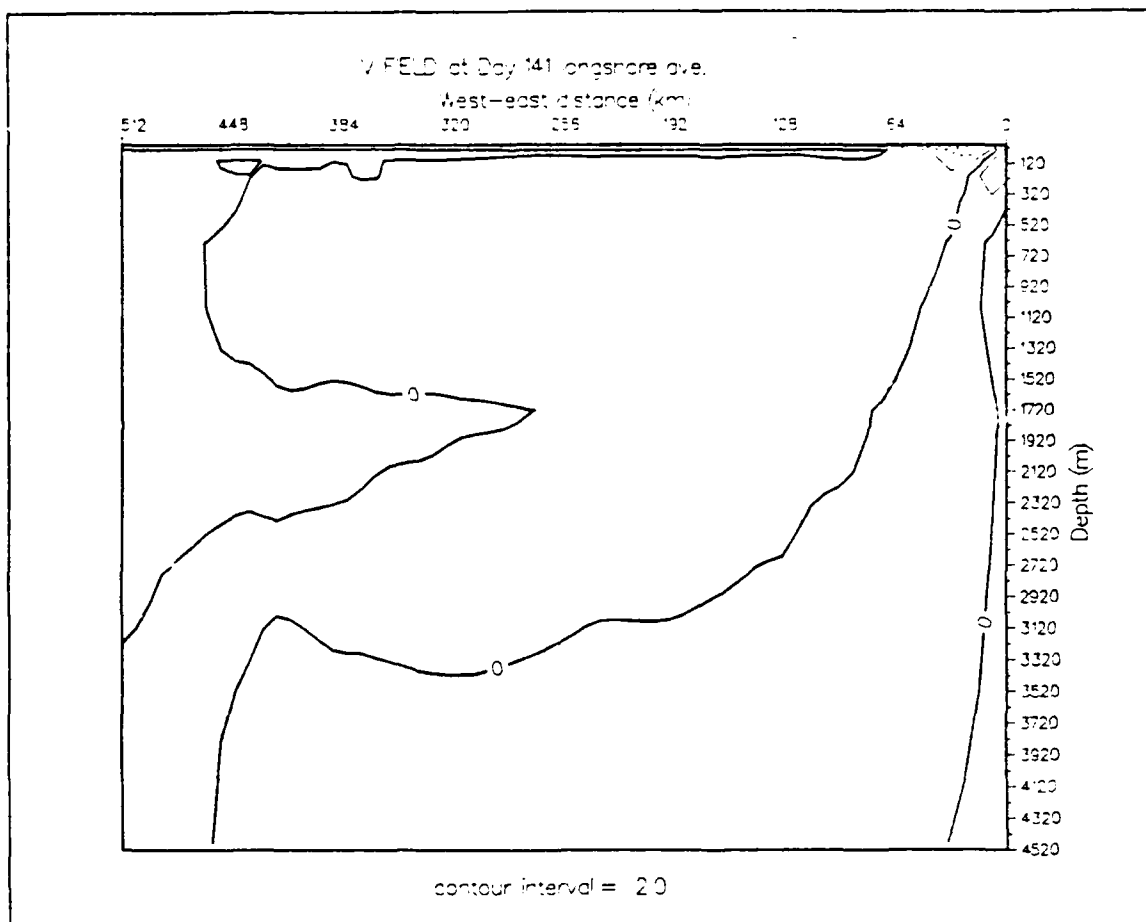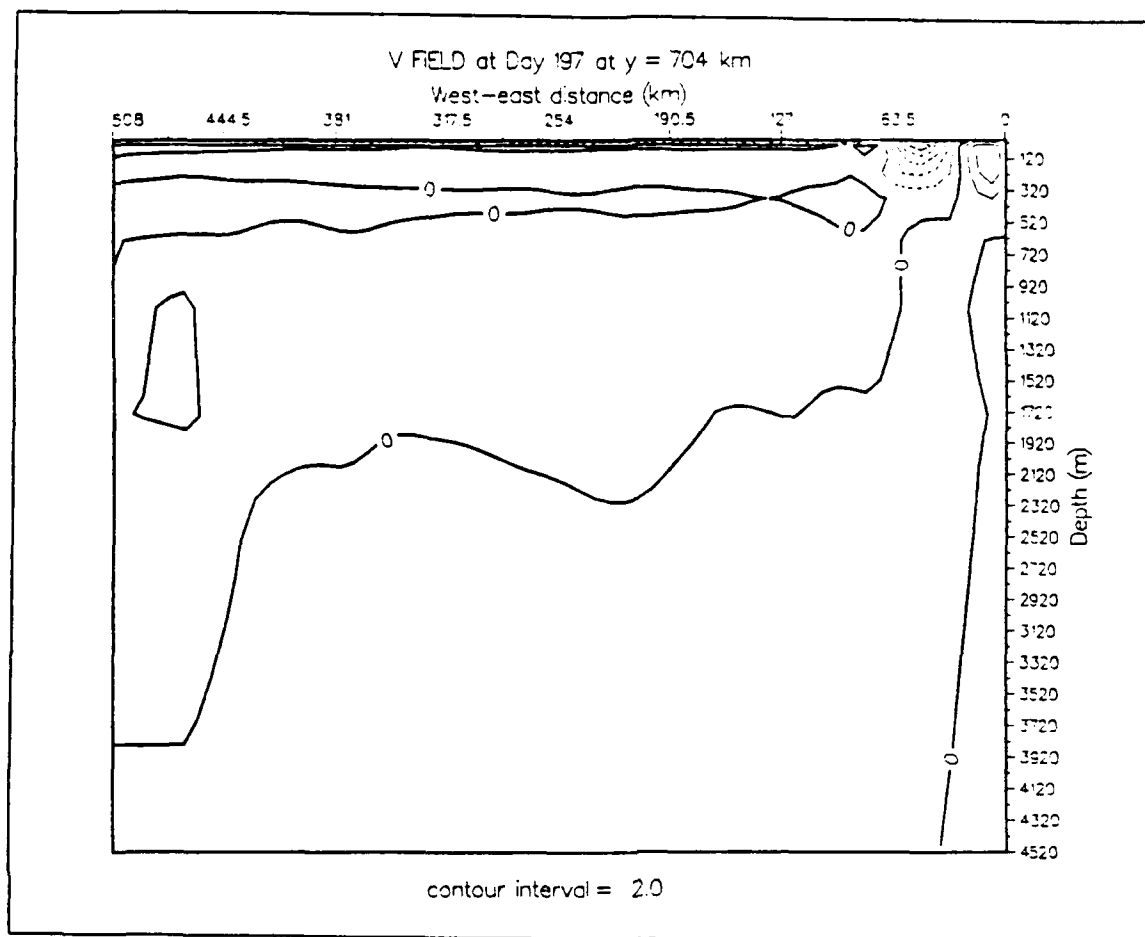
**Figure 77.** Vertical cross-shore section of meridional (v) velocity (cm/s) at y = 704 km for experiment 3 at day 197: Contour interval is 2.0 cm.s. Dashed lines denote equatorward velocities.
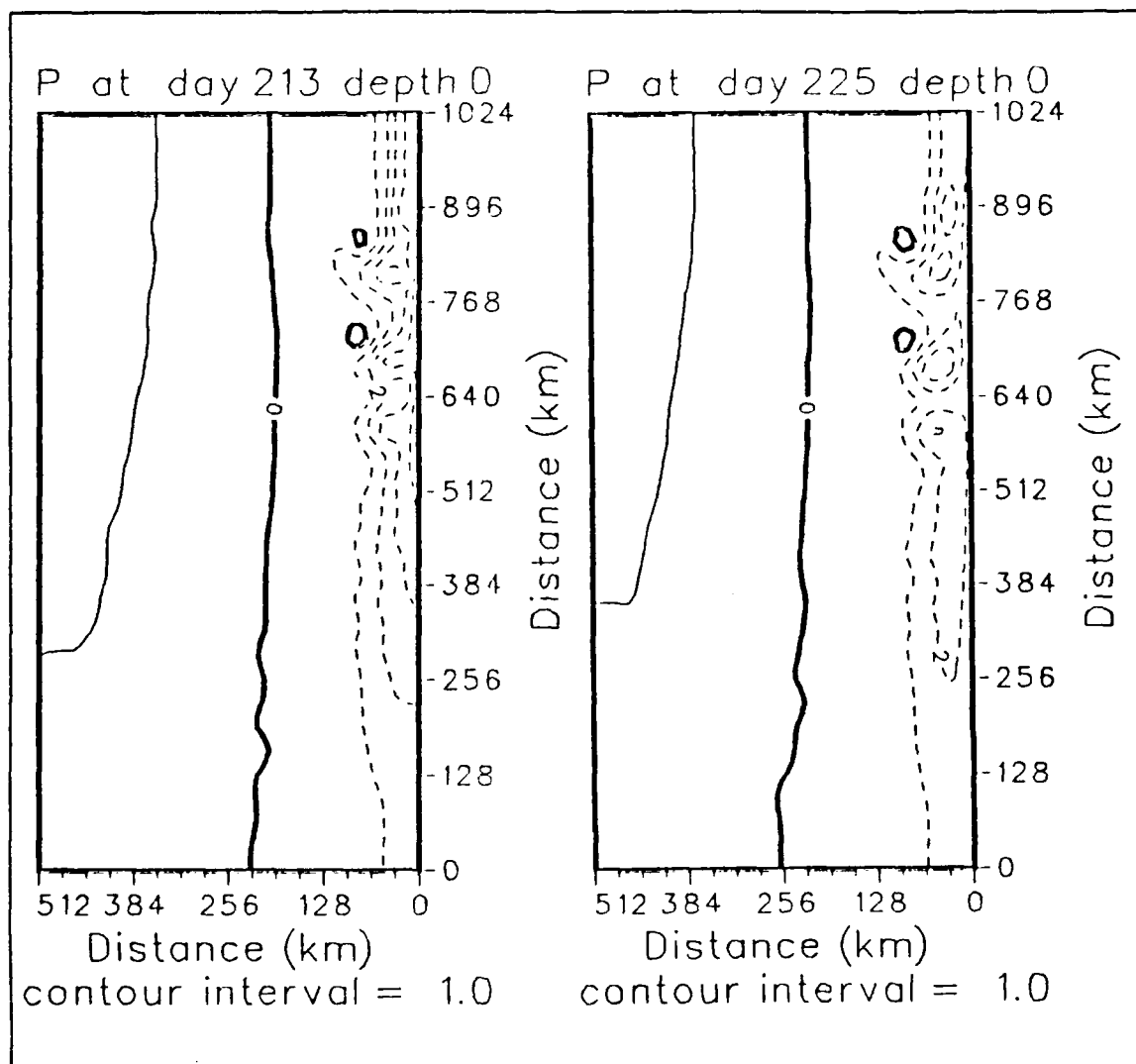
**Figure 78.** Surface isopleths of dynamic height (cm) relative to 2400 m for experiment 3 at day 213 (left) and day 225 (right): Contour interval is 1.0 cm. Dashed lines denote negative values.
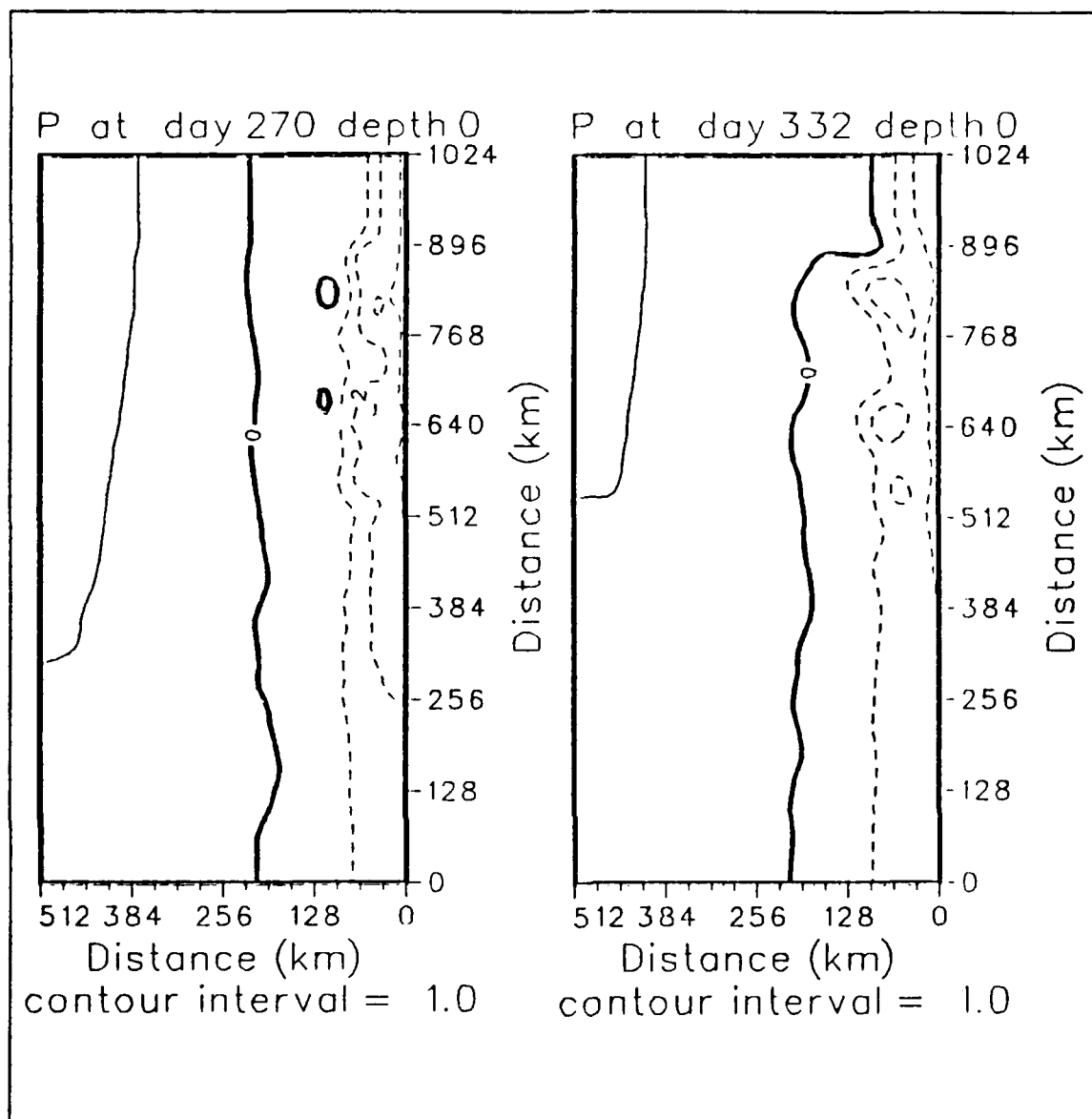
**Figure 79.** Surface isopleths of dynamic height (cm) relative to 2400 m for experiment 3 at day 270 (left) and day 332 (right): Contour interval is 1.0 cm. Dashed lines denote negative values.

# V. SUMMARY AND RECOMMENDATIONS

This study used a high-resolution, multi-level, primitive equation ocean model to investigate the role(s) of climatological and time dependent wind forcing as possible generation mechanism(s) for the coastal jets, undercurrents, fronts, and eddies in the eastern boundary current region off the west coast of the Iberian Peninsula. A band of steady equatorward winds, uniform alongshore but with zonal variability (a large negative wind stress near the coast, and narrow band of negative wind stress curl followed by regions of positive and negative wind stress curl offshore) was used as forcing in experiment 1. A band of spatially uniform, poleward winds from day 0 to day 20, followed by a reversal to spatially uniform, equatorward winds from days 21 to 105 was used as forcing in experiment 2. A band of spatially uniform, time dependent winds corresponding to the north/south component of the 6-hourly winds, computed from synoptic surface pressure analyses for the period from 1 February to 31 December 1986, was used as forcing in experiment 3. All experiments were performed on a $\beta$-plane, in an idealized, flat-bottom oceanic regime along the eastern boundary off Portugal.

On day 5 of experiment 1, in the meridional band of negative wind stress curl, there was a change in sign of the zonal gradients : of surface zonal velocity, of surface dynamic height, and of the upper ocean temperature field. The upwelled isotherms near the coast were consistent with vertical motion near the coast to compensate the Ekman layer divergence due to the equatorward winds. Further offshore, in the region of negative wind stress curl (due to the decreased equatorward winds), the westward Ekman transport was reduced, resulting in surface layer convergence and downwelling. As expected, the distribution of the surface dynamic heights relative to 2400 m (which are proportional to temperature) shows a meridionally extended ridge in the band of negative wind stress curl. The equatorward surface current nearshore and poleward surface current offshore of the surface pressure ridge are approximately in geostrophic balance with the pressure gradient forces due to the horizontal distribution of density. The flow structure on day 5 was consistent with a similar experiment conducted by McClain et al. (1986) for the north and west coast of Galicia, in which a maximum southward speed resulted shoreward of the wind shear zone and a maximum northward speed occurred offshore of the zone. In our experiment 1, the maximum equatorward velocity was larger by a factor of two, which may be explained by the use of a larger equatorward wind stress

at the coast (3.5 $dynes/cm^2$ versus 3.0 $dynes/cm^2$) and a larger negative wind stress curl offshore.

By day 20 of experiment 1, both equatorward and poleward surface currents were stronger, and a poleward undercurrent was present adjacent to the boundary at depths between ~200 and 500 m, consistent with previous results of McCreary et al. (1987) and Batteen et al. (1989). There was evidence of eddies at y ~735 km and y ~191 km superimposed on this system.

By day 40 of experiment 1, four, well developed anticyclonic eddies were present along a meridional axis located close to the band of negative wind stress curl. All eddies were likely generated due to the anticyclonic shear of the wind in this region and each had a thermal structure consistent with warm core rings. Four cold water filaments were lying in places where the circulation of each anticyclone advected the upwelled water offshore. The alongshore wave length of the eddies was estimated, based on spectral analysis, to be approximately 154 km.

By day 60 of experiment 1, the two northern and the two southern eddies had merged/coalesced into one northern and one southern eddy. From days 60 to 90, the two eddies propagated westward and expanded in size. The estimated westward propagation rates were 1.4 km/day and 2.3 km/day for the northern and southern anticyclones, respectively. The faster rate for the southern eddy is qualitatively consistent with a faster $\beta$-induced motion at lower latitudes.

By day 90 of experiment 1, the eddies had stabilized in size and, as estimated by the spectral analysis, had a peak energy at a dominant wave length of ~300 km. From day 90 to the end of experiment 1 (day 154), the two anticyclones continued to propagate westward. By day 150, two new anticyclones were generated in the same region of negative wind stress curl as before. The thermal and velocity structures were consistent via the thermal wind relation.

The equatorward nearshore surface current and poleward surface countercurrent offshore, reproduced early in the experiment, were qualitatively consistent with a similar experiment (McClain et al., 1986) and with northward transport near the shelf break, as indicated by Coastal Zone Color Scanner (CZCS) imagery off the west coast of Galicia. However, due to the lack of available observations, it is not known if the instability of the flow and the resulting mesoscale eddies in this experiment correspond to reality off the IP. While the negative wind stress curl has been observed off the west coast of Galicia from 18 to 23 April 1982, and was probably orographically induced by the rias, no observations exist to verify how far downstream of the Galicia coast this negative

wind stress curl may occur. With the lack of observations, the results of experiment 1 may best be considered a process oriented study designed to study the influence of a small-scale, large negative wind stress curl superimposed on a large scale climatological positive wind stress curl offshore in an eastern boundary current sysyem.

Experiment 2 was conceived to study a "spring transition". On day 20 (end of the period of 1.2 *dynes/cm²* poleward wind stress) the flow responded with onshore Ekman transport convergence in the Ekman layer, and downwelling near the coast. The surface dynamic heights relative to 2400 m consistently indicated increasing values towards the coast and, as expected, a poleward surface current extended along the eastern boundary with lighter/warmer waters at the coast. Observations over the shelf off Oregon during the winter (prevailing poleward winds) have shown poleward flow over the shelf without mean vertical shear (Huyer, 1983). In experiment 2 the poleward surface current (alongshore averaged maximum meridional velocity of ~ 12 cm s extending down to ~150 m) showed vertical shear, which may be explained via the thermal wind relation by the exaggerated downward displacement of the isotherms in the coastal upper ocean. There was also a weak equatorward undercurrent.

Experiment 2 showed a relatively fast (1-2 days) response of the system to a reversal to equatorward winds of 3.5 *dynes/cm²* . On day 22 (2 days after the transition to equatorward wind stress), the model responded with offshore Ekman transport in the upper layer, upwelled isotherms near the coast, and the replacement of the previous poleward surface current by an equatorward surface current. On day 30, with increasing time under the influence of the equatorward winds, the upwelled 16 and 15°C isotherms intercepted the surface and were displaced offshore and the surface equatorward coastal current, associated with the front in the upper ~70 m, had a jet-like structure which showed large vertical shear in the alongshore velocity. The poleward undercurrent, with an averaged alongshore velocity of ~5 cm s, was present nearshore between ~320 and 450 m depth. In experiment 2, the changes of the thermal and velocity structures near the coast were consistent with observations of the 25 through 31 March 1975 spring transition off Oregon (Huyer, 1983) by having upward sloping isotherms, a mean southward surface current, and strong vertical shear. No observations are available to document a "spring transition" off Portugal.

From day 30 to day 50 the surface isotherms were continuously displaced offshore, the surface equatorward jet widened as far as 64 km from the coast (day 50) and became shallower inshore. The upper portion of the poleward undercurrent became closer to the surface (depth of ~120 m at the coast) and a weak surface poleward countercurrent de-

veloped offshore of the equatorward jet in the middle model domain. The southward surface jet and poleward undercurrent at depths below 120 m were consistent with the typical summer coastal upwelling regime off Oregon, as described by Huyer (1983). Off Portugal, current meter observations (Fiúza, 1984) from 12 June to 7 July 1980 (peak of the upwelling season) on the inner and outer shelf at latitude 38° 06'N showed weak mean southward flows (-1.7 and -2.1 cm/s for the inshore and near-shelf break stations, respectively). However, these observations were taken under a regime of quasi-permanent southward, but fluctuating winds, and topographic features, such as the Setúbal embayment and Setúbal canyon in the vicinity of the current meter stations, thus making comparisons with the model results difficult, because the model assumes a straight coastline, flat bottom and was forced by a steady, relatively large wind stress.

Two anticyclonic eddies were generated between days 70 and 75 of experiment 2 at positions y ~593 km and y ~473 km in a region of high surface dynamic height that was existent in approximately the middle of the model domain, 60 km offshore. One closed cyclonic circulation also existed on day 75, that developed from the meandering jet at y ~ 540 km near the coast. From day 75 to the end of the experiment (day 105), a new anticyclone developed from meanders of the coastal jet and was present on day 90 at y ~835 km, approximately 65 km offshore. The eddies intensified and were displaced continuously southwestward probably due to advection by the mean flow. Experiment 2, like experiment 1, can be considered a process-oriented study to give insight on the coastal ocean processes associated with "spring transitions" along eastern boundaries.

The time series of the wind velocities used to force the model in experiment 3 suggests that pulses of strong or moderate poleward winds with time scales of a few days (typically ~ 4-6 days) may be important, especially during the pre-upwelling season (February) and also after the decay of upwelling (November and December). In experiment 3, between days 5 and 16 (6 to 17 February), the existing equatorward coastal surface current, created by previous equatorward winds, disappeared and was replaced by a poleward surface coastal current. Situations of short pulses of strong poleward winds (for instance from day 61 to 63) may not be enough to completely reverse a pre-existing equatorward surface current, but the current tends to decrease in intensity and is reduced in cross-sectional area, while the poleward undercurrent increases in intensity, expands in cross-sectional area, and displaces the weakened equatorward current offshore.

During the upwelling season, fluctuations of the prevailing equatorward winds with time scales of a few days (typically 4-5 days) correspond to events of intensification and

relaxation. With intensification of the winds favorable for upwelling, the upwelled isotherms near the surface respond with additional offshore displacement consistent with increased offshore Ekman transport, the surface equatorward jet increases in vertical extent, and the poleward undercurrent is considerably reduced. With the relaxation of the equatorward winds, the surface isotherms tend to recede towards the coast, but the configuration of the isotherms in the upper 200 m stays upwelled. Off the coastal of Portugal, surveys of sea surface temperature using an airborne radiation thermometer (Fiúza, 1982) and satellite infrared imagery (Fiúza, 1984) have indicated onshore progression of warmer oceanic waters in association with relaxation of the northerly winds. During the relaxation, the equatorward surface current became shallower and the poleward undercurrent got closer to the surface and increased in size. Experiment 3 also showed that by the middle and end of the upwelling season, mesoscale eddies are likely to be generated off the west coast of Portugal. On day 188 (8 August) from a meander of the surface coastal jet, a closed anticyclonic circulation developed at $y \sim 748$ km. On day 197 (17 August) two new closed cyclonic circulations show up at $y \sim 832$ km and $y \sim 704$ km. The thermal structure of the anticyclone shows downward displacement of the upper ocean isotherms in the center of the eddy. The thermal structures of the cyclonic eddies show raised upper ocean isotherms in the center of the eddies. Distributions of the velocities associated with the eddies are consistent with the thermal structures via the thermal wind relation. A cold water filament is recognized at the surface on day 197 (17 August), lying between a dipole pair of eddies composed of the anticyclone and the northern cyclone. On day 213 of experiment 3 (2 September), a second anticyclone was present at $\sim848$ km. The two cyclonic eddies positioned closer to the coast than the anticyclone split, resulting in four cyclones that spanned the coastal region by day 225 (14 September). During November and December, with the decreased influence of the winds favorable for upwelling and with some time intervals of strong moderate poleward winds (days 281 to 283, 284 to 286, and 299 to 310), the eddies, as recognized in the distribution of surface dynamic height, weakened and disappeared. On day 332 (30 December) the two anticyclones were no longer evident and only weak remains of the cyclonic circulations were superimposed on the also weakened surface coastal current system.

The results from the experiments support the hypothesis that wind forcing, and particularly time dependent winds, can be a significant generation mechanism for eddies, jets, fronts, and upwelling filaments off the west coast of the IP. It should be noted, however, that this study employed the constraints of a regular, straight coastline and a

flat bottom to isolate and examine the effects of wind forcing. Future studies should use climatological, spatially resolved winds (values on a grid with points one-degree or even less apart) for the region and also time dependent, spatially resolved winds. Features like the irregular coastline and bottom topography should also be included in the numerical studies, because they are likely to be important mechanisms in controlling the locations of mesoscale features in the study region. Inclusion of salinity, which is important in controlling the density at the depths of the Mediterranean Water influence, may also improve the accuracy of the results in the experiments. Besides the numerical studies, observational programs on the shelf and slope should be implemented including current meter arrays, Lagrangian current drifters, remote sensing, and CTD surveys with appropriate space time resolution to synoptically map mesoscale structures. Such a program would allow realistic comparisons with the numerical studies.

# LIST OF REFERENCES

Ambar, I.,and M.R. Howe 1979. Observations of the Mediterranean outflow - I. Mixing in the Mediterranean outflow. *Deep-Sea Res., 26,* 535-554.

Ambar, I., 1983. A shallow core of Mediterranean water off western Portugal. *Deep-Sea Res., 30,* 677-680.

Ambar, I., 1984. Seis meses de medições de correntes, temperaturas e salinidades na vertente continental ao largo da costa alentejana. *Relatório técnico, I 84,* Grupo de Oceanografia, *Universidade de Lisboa,* 47 pp. (*Unpublished manuscript*).

Ambar, I., 1985. Seis meses de medições de correntes, temperaturas e salinidades na vertente continental Portuguesa a 40 N. *Relatório técnico, I 85.* Grupo de Oceanografia, *Universidade de Lisboa,* 40 pp. (*Unpublished manuscript*).

Arakawa, A., and V.R. Lamb, 1977. Computational design of the basic dynamical processes of the UCLA general circulation model. *Methods in Computational Physics.* J. Chang. Ed., Academic Press, *17,* 173-265.

Bakun, A., 1987. *Applications of maritime data to the study of surface forcing of seasonal and interannual ocean variability in eastern boundary regions.* Ph.D. Dissertation, Oregon State University, Corvalis, OR, 226 pp.

Barton, E. D., 1989. The poleward undercurrent on the eastern boundary of the subtropical North Atlantic. In : *Poleward Flow along Eastern Ocean Boundaries,* edited by S. Neshyba, C.N.K. Mooers and R.L. Smith. Springer - Verlag Lecture Notes. 82-94.

Batteen, M.L., and Y.-J. Han, 1981. On the computational noise of finite-difference schemes used in ocean models. *Tellus, 33,* 387-396.

Batteen, M.L., R. L. Haney, T.A. Tielking, and P G. Renaud, 1989. A numerical study of wind forcing of eddies and jets in the California Current System. *J. Mar. Res., 47,* 493-523.

Camerlengo, A.L., and J.J. O'Brien, 1980. Open boundary conditions in rotating fluids. *J. Comput. Physics, 35,* 12-35

Chatfield, C., 1984. *The Analysis of Time Series : An Introduction.* Chapman and Hall, New York, 286 pp.

Emery, W.J., and L.A. Mysak, 1980. Dynamical interpretations of satellite-sensed thermal features off Vancouver Island. *J. Phys. Oceanogr., 10,* 961-970.

Esbenson S.K. and Kushnir Y., 1981. The heat budget of the global ocean : an atlas based on estimates from surface marine observations. *Climatic Research Institute, report 29,* 27 pp.

Fiúza, A.F.G., 1982. The Portuguese coastal upwelling system. *In Present problems of oceanography in Portugal, Junta Nacional de Investigação Científica e Tecnológica, Lisboa*, 45-71.

Fiúza, A.F.G., 1984. Hidrologia e dinâmica das águas costeiras de Portugal. *Dissertação apresentada à Universidade de Lisboa para obtenção do grau de Doutor em Física, especialização em Ciências Geofísicas*, 1-294.

Fiúza, A.F.G.,and F.M. Sousa, 1989. Preliminary results of a CTD survey in the Coastal Transition Zone off Portugal during 1-9 September 1988. *Coastal Transition Zone Newsletter, 4,* 2-9.

Haney, R.L., 1985. Midlatitude sea surface temperature anomalies: A numerical hindcast. *J. Phys. Oceanogr., 15,* 787-799.

Haney, R. L., W.S. Shiver, and K.H. Hunt, 1978. A dynamical-numerical study of the formation and evolution of large-scale ocean anomalies. *J. Phys. Oceanogr., 8,* 952-969.

Holland, W.R., 1978. The role of mesoscale eddies in the general circulation of the ocean-- Numerical experiments using a wind-driven quasi-geostrophic model. *J. Phys. Oceanogr., 8,* 363-392.

Holland, W.R., and M.L. Batteen, 1986. The parameterization of subgrid scale heat diffusion in eddy-resolved ocean circulation models. *J. Phys. Oceanogr., 16,* 200-206.

Huyer, A., 1983. Coastal upwelling in the California Current System. *Prog. Oceanogr., 12,* 259-284.

Huyer, A., 1988. Shelf circulation. *The Sea : Ocean Engineering Science, 9,* 51 pp., submitted.

Ikeda, M., and W.J. Emery, 1984. Satellite observations and modeling of meanders in the California Current System off Oregon and Northern California. *J. Phys. Oceanogr., 14,* 1434-1450.

Levitus, S., 1982. Climatological atlas of the world ocean. *U.S. Dep. Commer. NOAA Prof. Pap. 13 ,* 173 pp.

McClain, C. R., S. Chao, L. P. Atkinson, J. O. Blanton, and F. Castillejo, 1986. Wind-driven upwelling in the vicinity of Cape Finisterre, Spain. *J. Geophys. Res., 91,* 8470-8486.

McCreary, J.P., P.K. Kundu, and S. Chao, 1987. On the dynamics of the California Current System. *J. Mar. Res., 45,* 1-32.

Meincke, J., G. Siedler, and W. Zenk, 1975. Some current observations near the continental slope off Portugal. *"Meteor" Forsch.-Ergebn., A, 16,* 15-22.

Paulson, C.A., and J.J. Simpson, 1977. Irradiance measurements in the upper ocean. *J. Phys. Oceanogr., 7,* 952-956.

Reece, R.H., 1989. *An analysis of hydrographic data collected off Point Sur, California in November 1988.* M.S. thesis Naval Postgraduate School, Monterey, CA. 76 pp.

Sverdrup, H. U., M.W. Johnson, and R.H. Fleming, 1942. *The Oceans their Physics, Chemistry, and General Biology.* Prentice-Hall, Inc., Englewood Cliffs, N.J., 1087 pp.

Tchernia, P., 1980. *Descriptive Regional Oceanography.* Pergamon Marine Series, 253 pp.

Thompson, R.O.R.Y., 1984. Observations of the Leeuwin Current off Western Australia. *J. Phys. Oceanogr.*, *14*, 623-628.

Thomson, R.E., 1984. A cyclonic eddy over the continental margin off Vancouver Island: Evidence for baroclinic instability. *J. Phys. Oceanogr.*, *14*, 1326-1348.

Watts, D. R., 1983. Gulf stream variability. *Eddies in Marine Science* (A. R. Robinson, Ed.), Springer-Verlag, New York, 114-144.

Weatherly, G.L., 1972. A study of the bottom boundary layer of the Florida current. *J. Phys. Oceanogr.*, *2*, 54-72.

Wooster, W. S., A. Bakun, and D. R. McLain, 1976. The seasonal upwelling cycle along the eastern boundary of the North Atlantic. *J. Mar. Res.*, *34*, 131-140.

Wright, D.G., 1980. On the stability of a fluid with specialized density stratification. Part II. Mixed baroclinic-barotropic instability with application to the Northeast Pacific. *J. Phys. Oceanogr.*, *10*, 1307-1322.

# INITIAL DISTRIBUTION LIST

1. Defense Technical Information Center  2
   Cameron Station
   Alexandria, VA  22304-6145

2. Library, Code 0142  2
   Naval Postgraduate School
   Monterey, CA  93943-5002

3. Chairman (Code 68Co)  1
   Department of Oceanography
   Naval Postgraduate School
   Monterey, CA 93943

4. Chairman (Code 63Rd)  1
   Department of Meteorology
   Naval Postgraduate School
   Monterey, CA 93943

5. Dr. M.L. Batteen (Code 68Bv)  3
   Department of Oceanography
   Naval Postgraduate School
   Monterey, CA 93943

6. Dr. R.L. Haney (Code 63Hy)  3
   Department of Meteorology
   Naval Postgraduate School
   Monterey, CA 93943

7. Director, Naval Oceanography Division  1
   Naval Observatory
   34th and Massachusetts Avenue NW
   Washington, DC 20390

8. Commanding Officer  1
   Fleet Numerical Oceanography Center
   Monterey, CA 93943

9. Commanding Officer  1
   Naval Environmental Prediction Research Facility
   Monterey, CA 93943

10. Naval Ocean Research and Development Activity  1
    NSTL Station
    Bay St. Louis, MS 39522

11. Office of Naval Research (Code 420)  1
    800 N. Quincy Street
    Arlington, VA 22217

12. Dr. Andrew Bakun  2
    Pacific Fisheries Environmental Group
    Southwest Fisheries Science Center, NMFS
    NOAA
    P.O. Box 831
    Monterey, CA 93942

13. CDR Craig S. Nelson  1
    Department of Oceanography
    Naval Postgraduate School
    Monterey, CA 93943

14. Prof. Robert L. Smith  1
    College of Oceanography
    Oregon State University
    Corvallis, OR 97331

15. Prof. Adriana Huyer  1
    College of Oceanography
    Oregon State University
    Corvallis, OR 97331

16. Prof. Eric D. Barton  1
    Department of Physical Oceanography
    University College of North Wales
    Menai Bridge, Gwynedd LL59 5EY
    United Kingdom

17. Prof. Armando F. G. Fiúza  1
    Grupo de Oceanografia
    Departamento de Fisica, Centro de Geofisica
    Universidade de Lisboa
    Rua da Escola Politecnica, 58
    1200 Lisboa
    Portugal

18. Prof. Isabel L. S. A. Ambar  1
    Grupo de Oceanografia
    Departamento de Fisica, Centro de Geofisica
    Universidade de Lisboa
    Rua da Escola Politecnica, 58
    1200 Lisboa
    Portugal

19. Dr. Charles R. McClain     1
    Laboratory for Oceans
    NASA Goddard Space Flight Center
    Greenbelt, MD 20771

20. Dr. Larry P. Atkinson     1
    Department of Oceanography
    Old Dominion University
    Norfolk, VA 23508

21. Dr. Jack O. Blanton     1
    Skidaway Institute of Oceanography
    Savannah, GA 31406

22. Direcção do Serviço de Instrução e Treino     1
    Marinha Portuguesa
    Rua do Arsenal
    1100 Lisboa
    Portugal

23. Director Geral do Instituto Hidrográfico     1
    Instituto Hidrográfico
    Rua das Trinas, 49
    1200 Lisboa
    Portugal

24. LCDR Carlos N. Lopes da Costa     5
    Instituto Hidrográfico
    Rua das Trinas, 49
    1200 Lisboa
    Portugal

25. Dr. D. Evans     1
    Office of Naval Research (Code 1122PO)
    800 N. Quincy St.
    Arlington, VA 22217

26. Dr. T. Kinder     1
    Office of Naval Research (Code 1122CS)
    800 N. Quincy St.
    Arlington, VA 22217

27. Director of Research Administration (Code 012)     1
    Naval Postgraduate School
    Monterey, CA 93943

28. Dr. Mário Ruivo                                                         1
    Membro do Conselho Consultivo da JNICT
    Coordenação da Area de Ciências e Tecnologia do Mar
    Av. D. Carlos I, 126
    1200 Lisboa
    Portugal

29. Dr. Hipólito Monteiro                                                   1
    Serviços Geológicos de Portugal
    Rua da Academia das Ciências, 126
    1200 Lisboa
    Portugal

30. Dr Pedro Ré                                                            1
    Secção Biologia Maritima da Faculdade de Ciências
    Universidade de Lisboa, Bloco C2
    Campo Grande
    1700 Lisboa
    Portugal

31. CDR Moshe Marom                                                        1
    Department of Oceanography
    Naval Postgraduate School
    Monterey, CA 93943

32. LT Manuel A. F. Pinto Abreu                                            1
    Department of Oceanography
    Naval Postgraduate School
    Monterey, CA 93943

33. Dr. Paul E. Smith                                                      1
    Southwest Fisheries Science Center
    National Marine Fisheries Service
    NOAA
    P.O. Box 271
    La Jolla, CA 92038

34. Mr. Ronald J. Lynn                                                     1
    Southwest Fisheries Science Center
    National Marine Fisheries Service
    NOAA
    P.O. Box 271
    La Jolla, CA 92038